Structures of Dark Matter Halos

ASTR:6782
Hai Fu

Observational Evidence of Dark Matter Halos

Method 1: Rotation Curves of Disk Galaxies

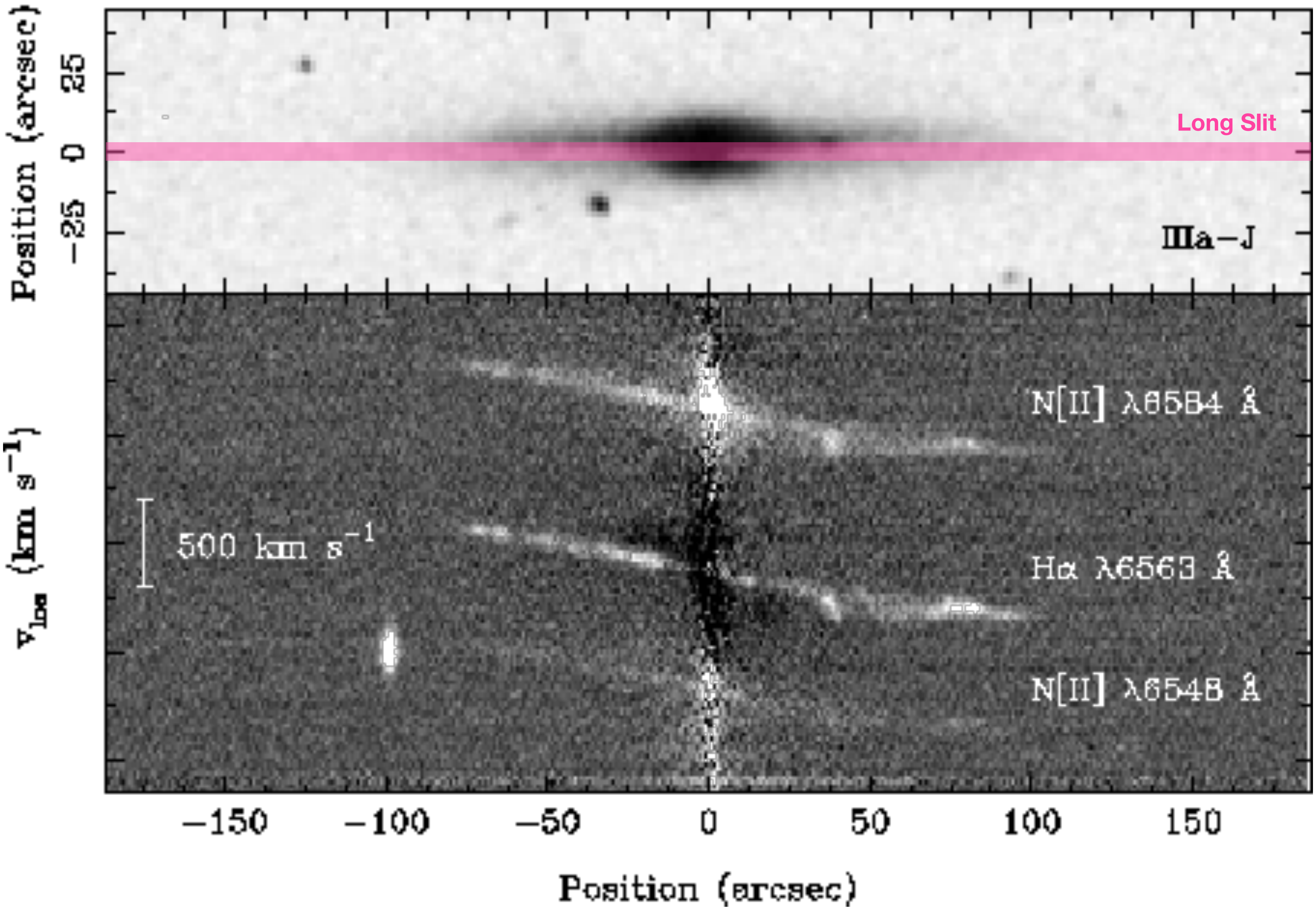

Method 2: Orbit Superposition of Elliptical Galaxies

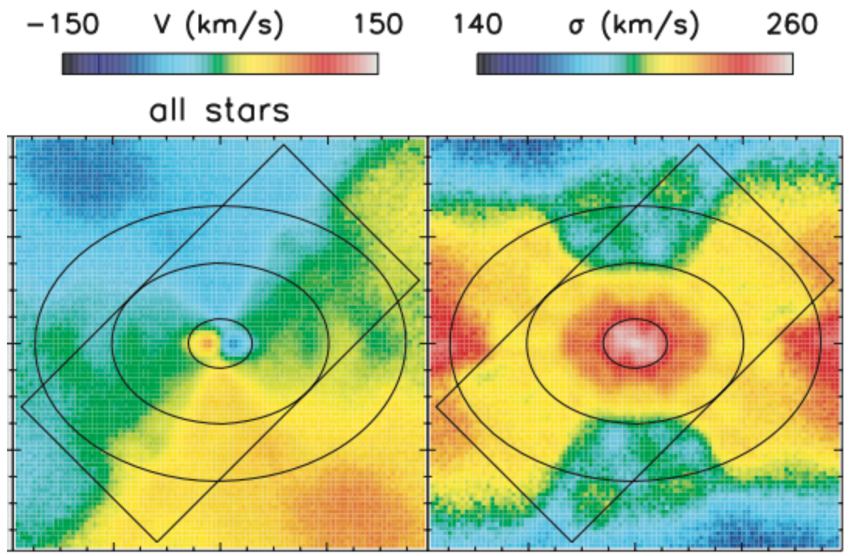

NGC4365

van den Bosch+ 2008

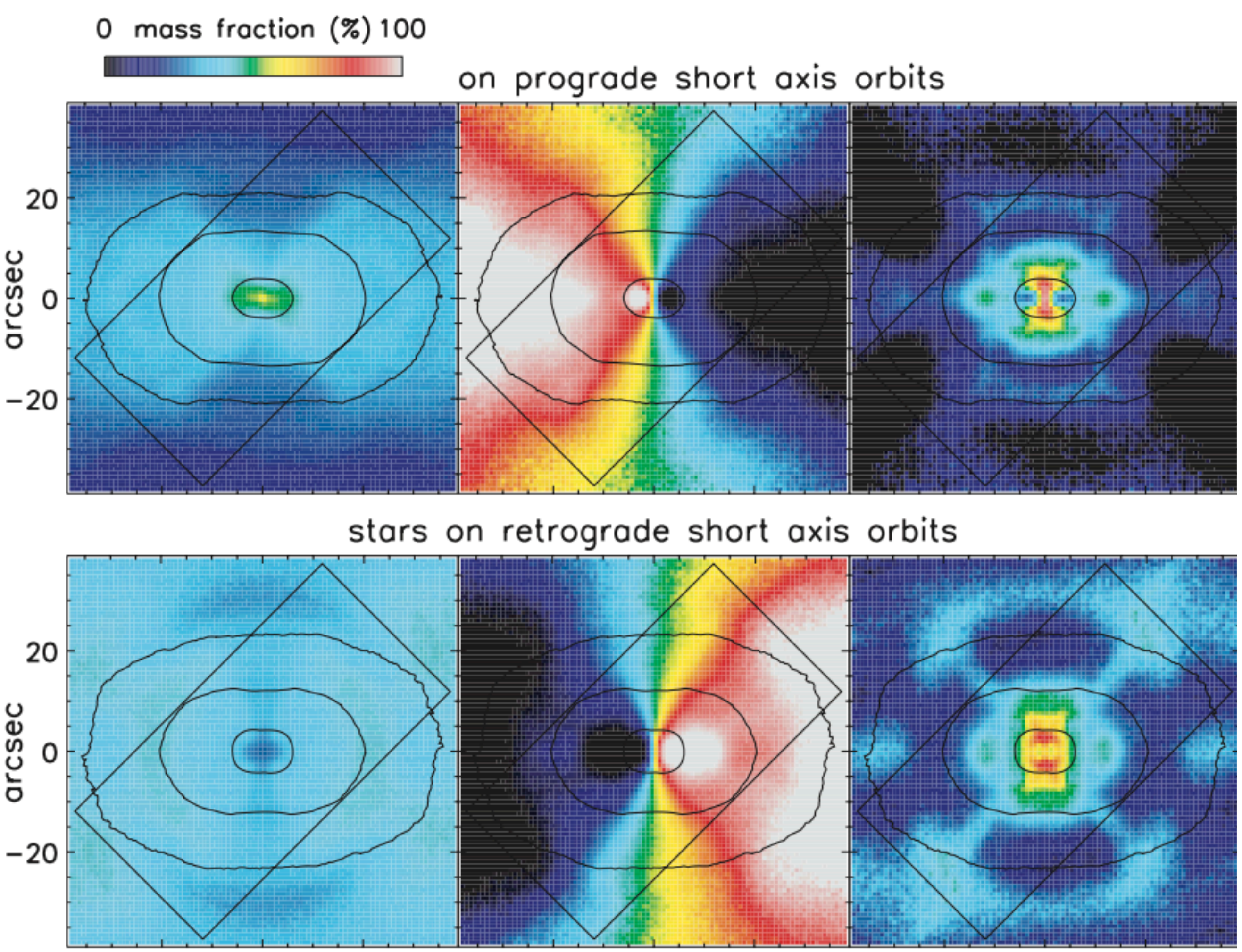

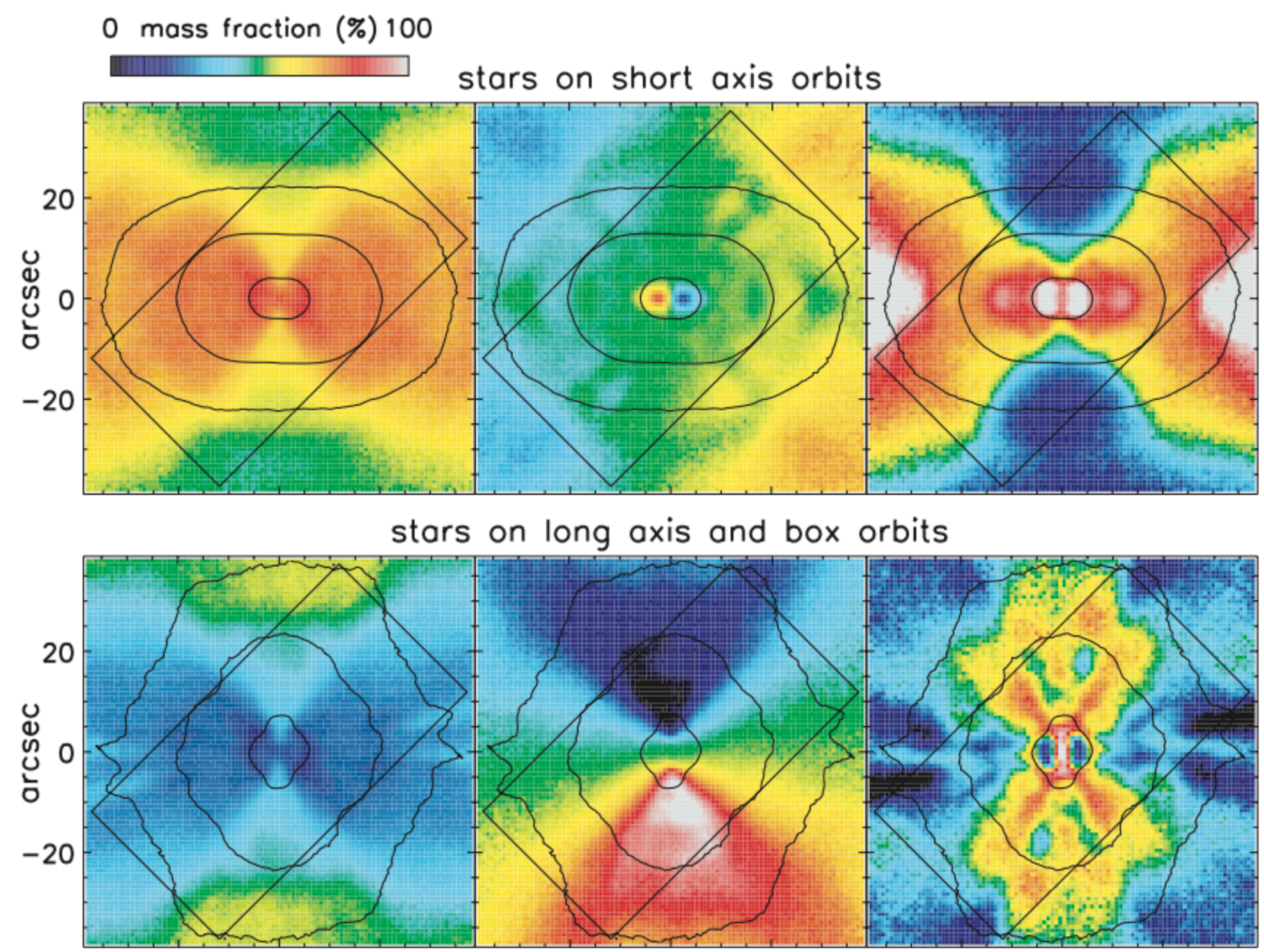

Method 3: Virial Theorem & Hydrostatic Equilibrium

Zwicky 1933: **velocity dispersion** of galaxies in the Coma Cluster

Virial Theorem: $2\bar{K} + \bar{U} = 0 \rightarrow \sigma^2 = GM/R \rightarrow M = \sigma^2 R/G$

The virial mass is **400x** greater than visible stellar mass

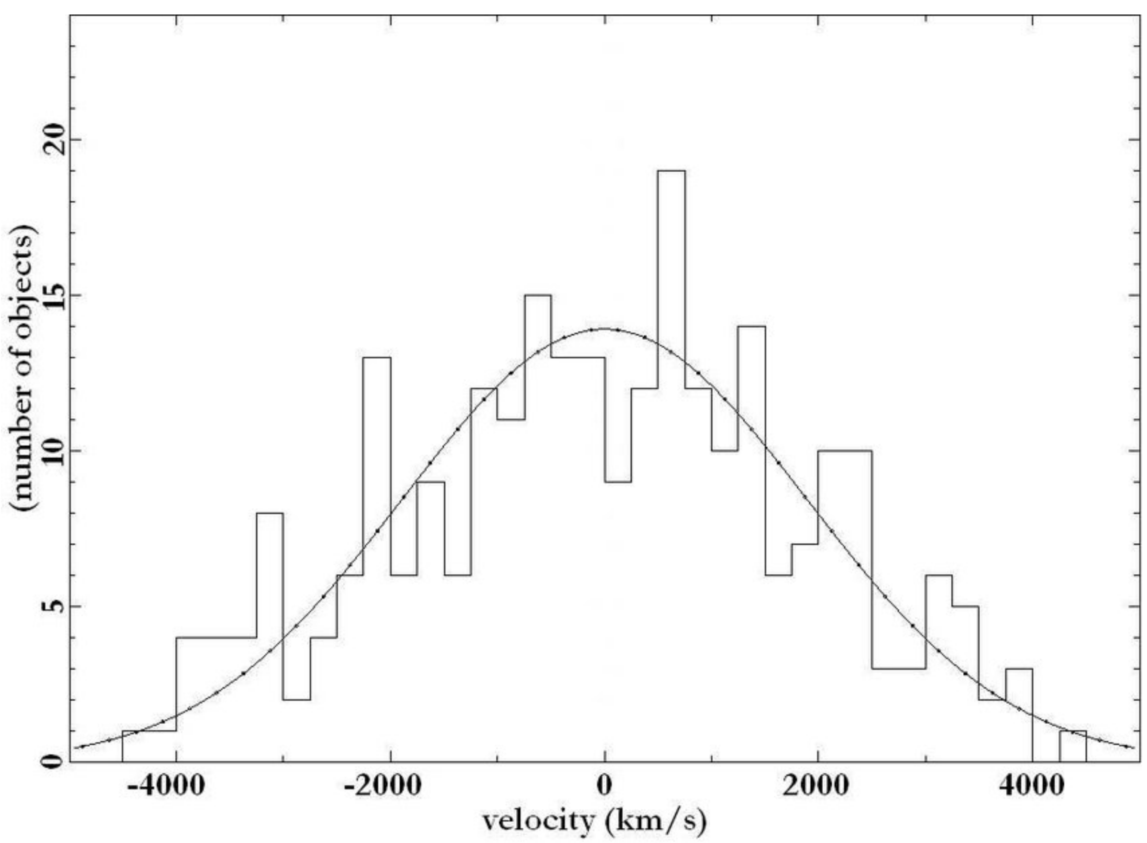

Gaussian Probability Density Function

$$p(x) = \frac{1}{\sigma\sqrt{2\pi}}\, e^{-\frac{1}{2}\left(\frac{x-\mu}{\sigma}\right)^2}$$

where σ is the standard deviation and μ the mean

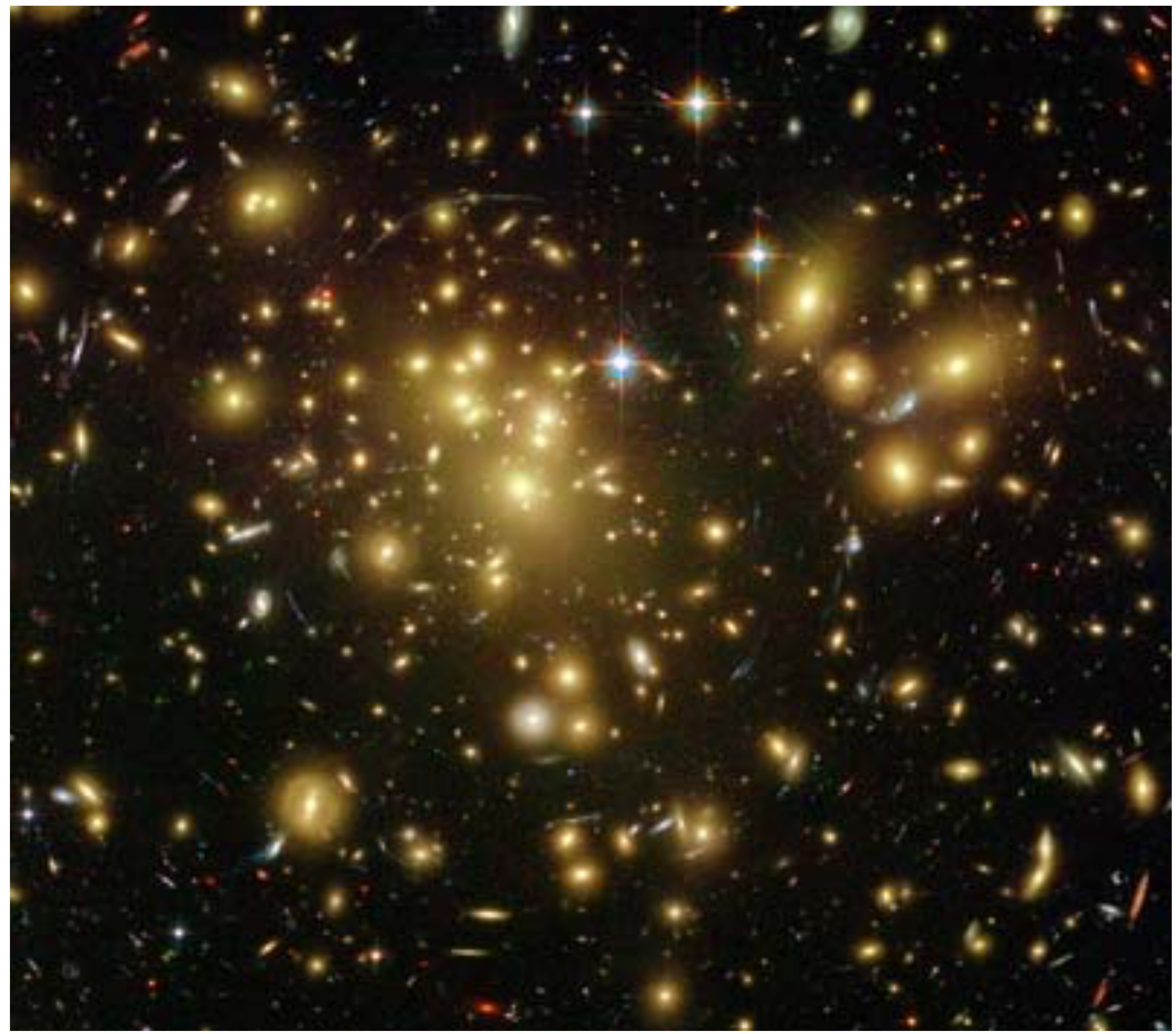

Method 4: Strong Gravitational Lensing

Lensing allows us to measure the *total* mass in the foreground lens galaxy

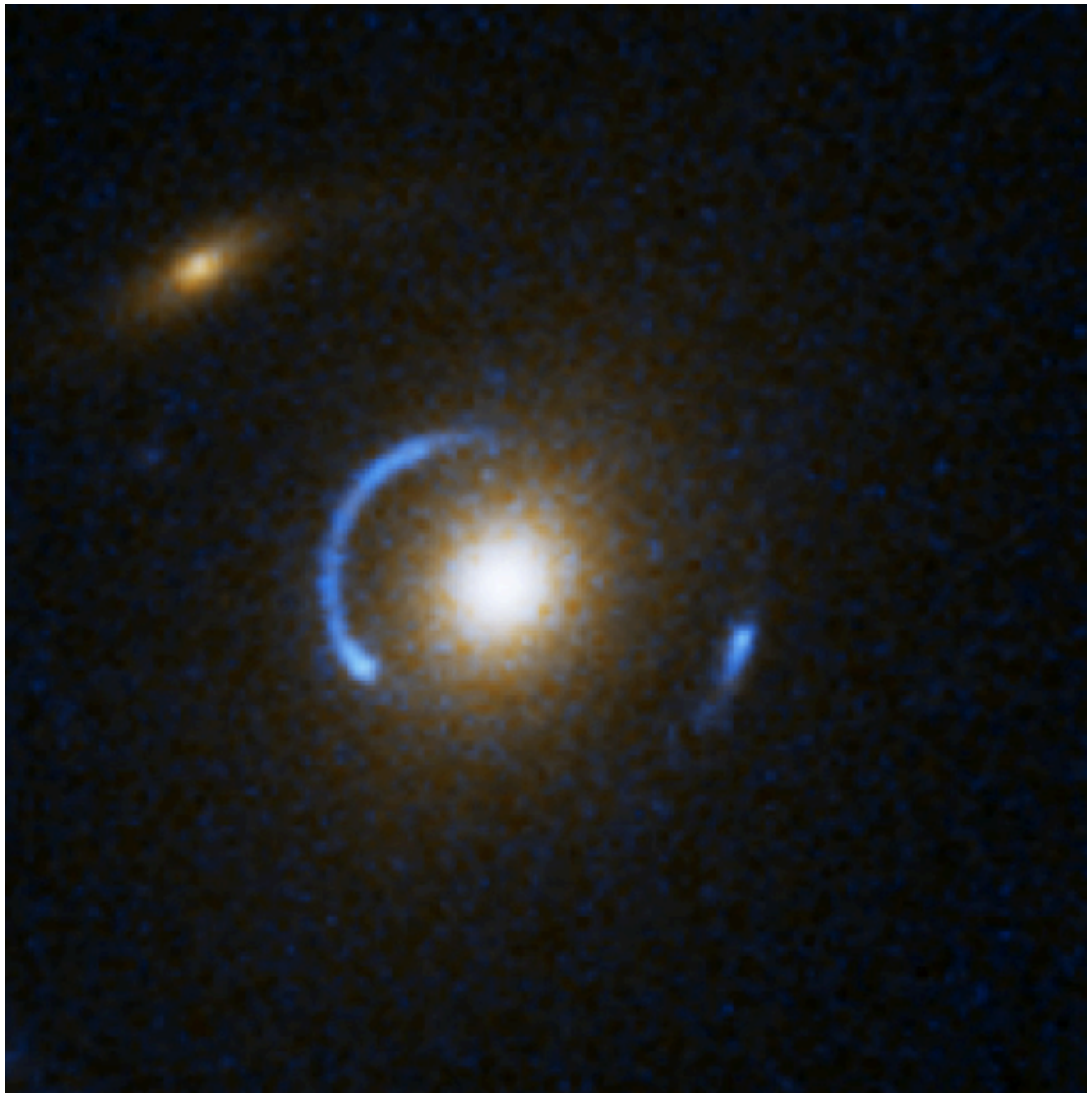

Method 5: Weak Gravitational Lensing

Lensing allows us to measure the *total* mass in the foreground lens galaxy or cluster

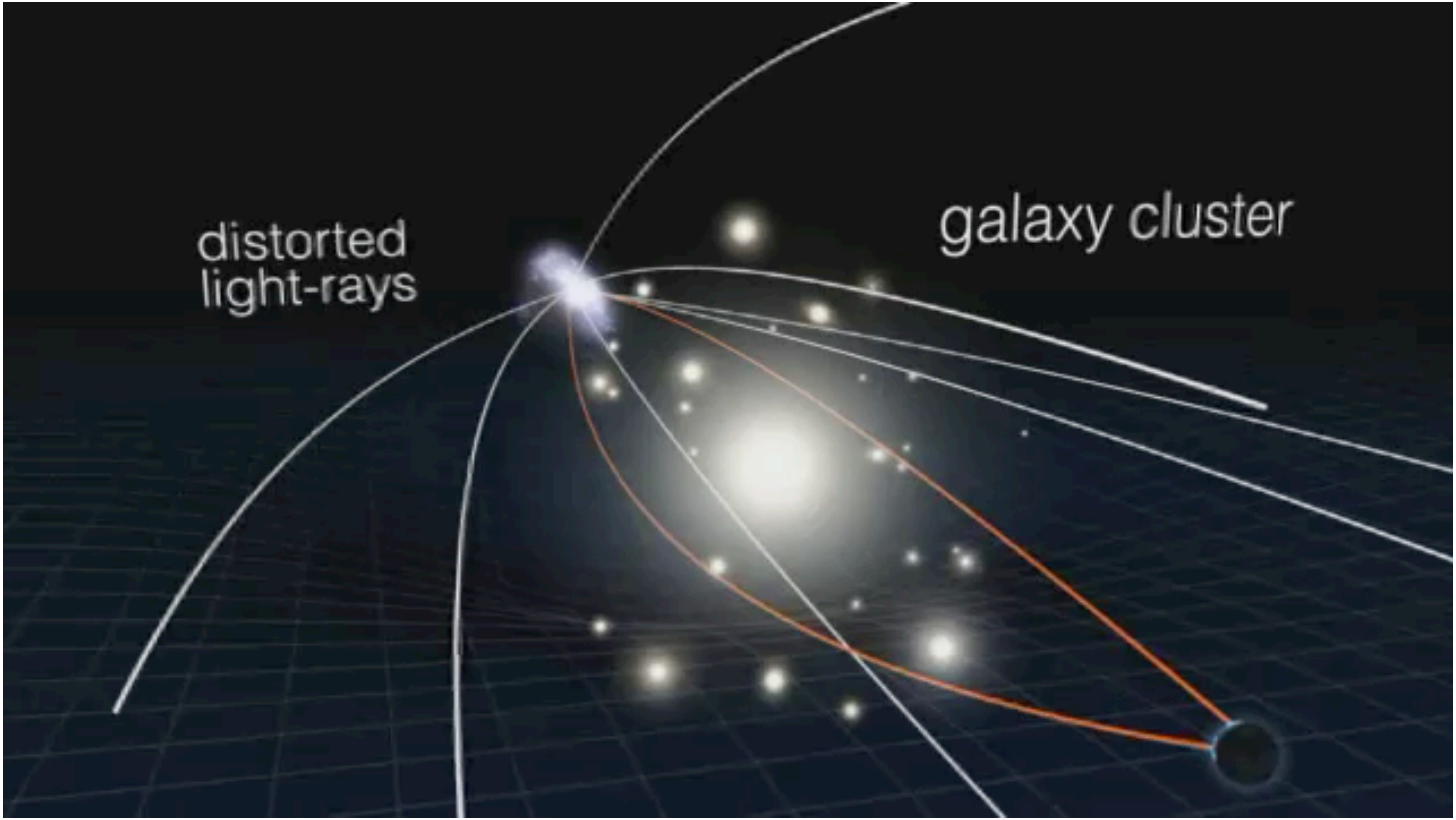

From the SC Model to N-body Simulations

Top-Hat Model: Density Evolution

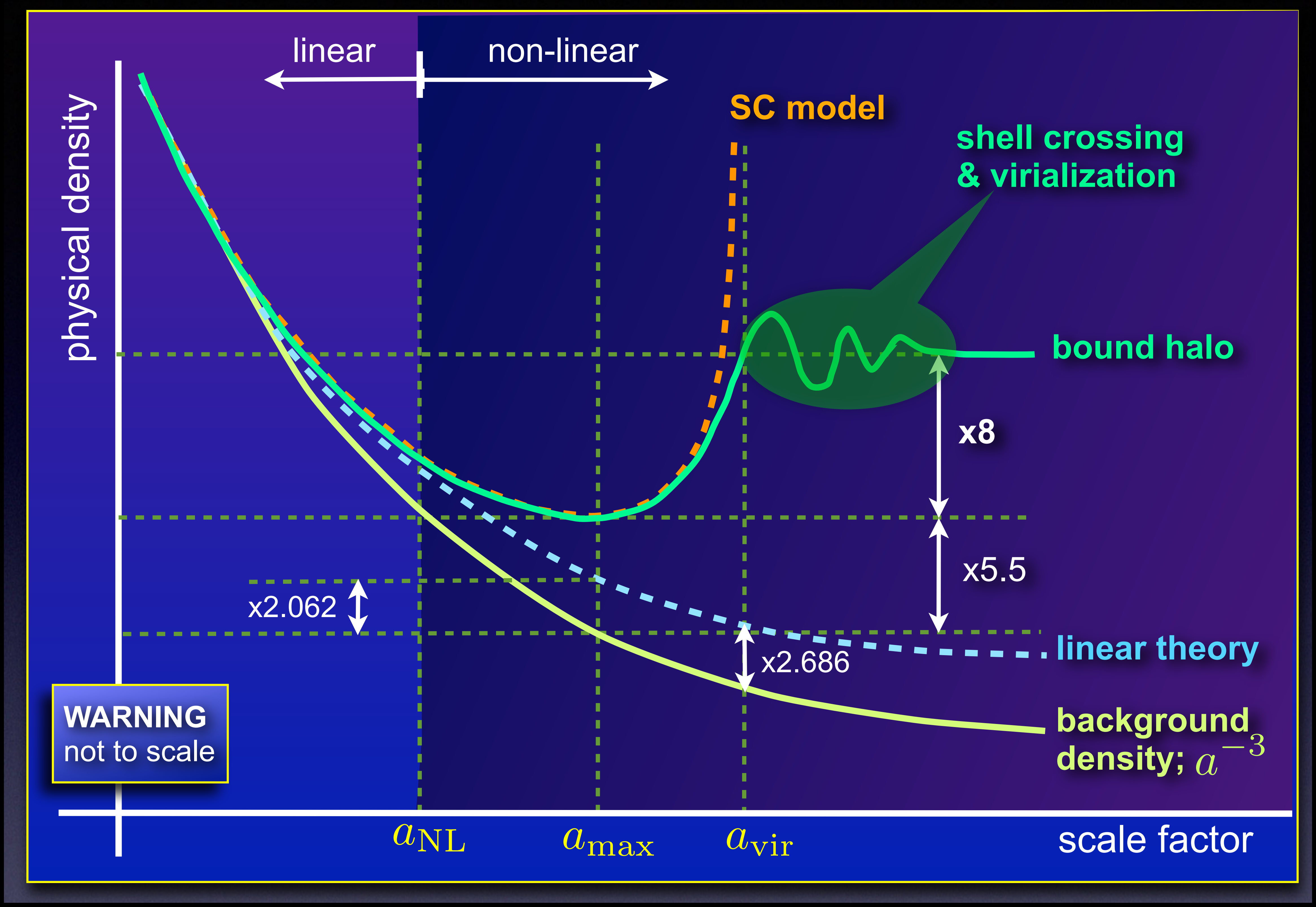

van den Bosch

From Top-Hat model to more realistic halos

- At the time of collapse, the entire structure maintains a constant density that is $18\pi^2$ times the critical density $\rho_c = 3H^2/8\pi G$
- The radius of the top-hat is well-defined by the density discontinuity at $r_v = a_v r_0$, while in reality, the density profile $\rho(r)$ should be smoothly declining until it reaches ρ_c.
- Although unrealistic, the top-hat model motivated the definition of the virial radius and virial mass of the collapsed object:

$$\bar{\rho}(r < r_\Delta) = \Delta_c \rho_c, \text{ and, } M_\Delta = \frac{4\pi}{3} r_\Delta^3 \Delta_c \rho_c \text{ where } \Delta_c = 200 \approx 18\pi^2$$

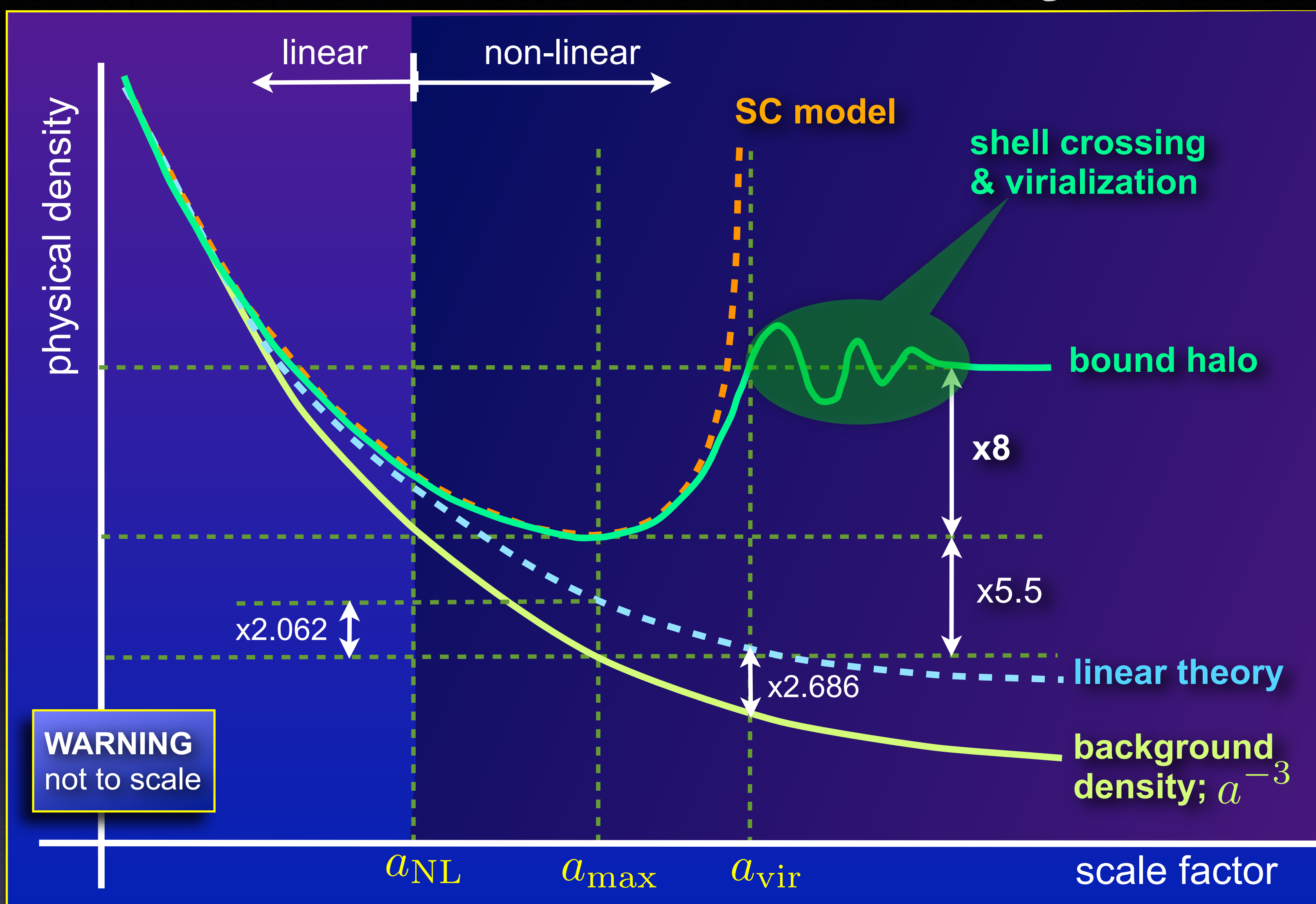

Artificial Evolution:

Because ρ_c continues to decline as the universe expands, the fixed Δ_c results in a *non-evolving* halo to *increase* in virial mass (due to definition).

dark matter simulation of a comoving volume that is 40 Mpc across

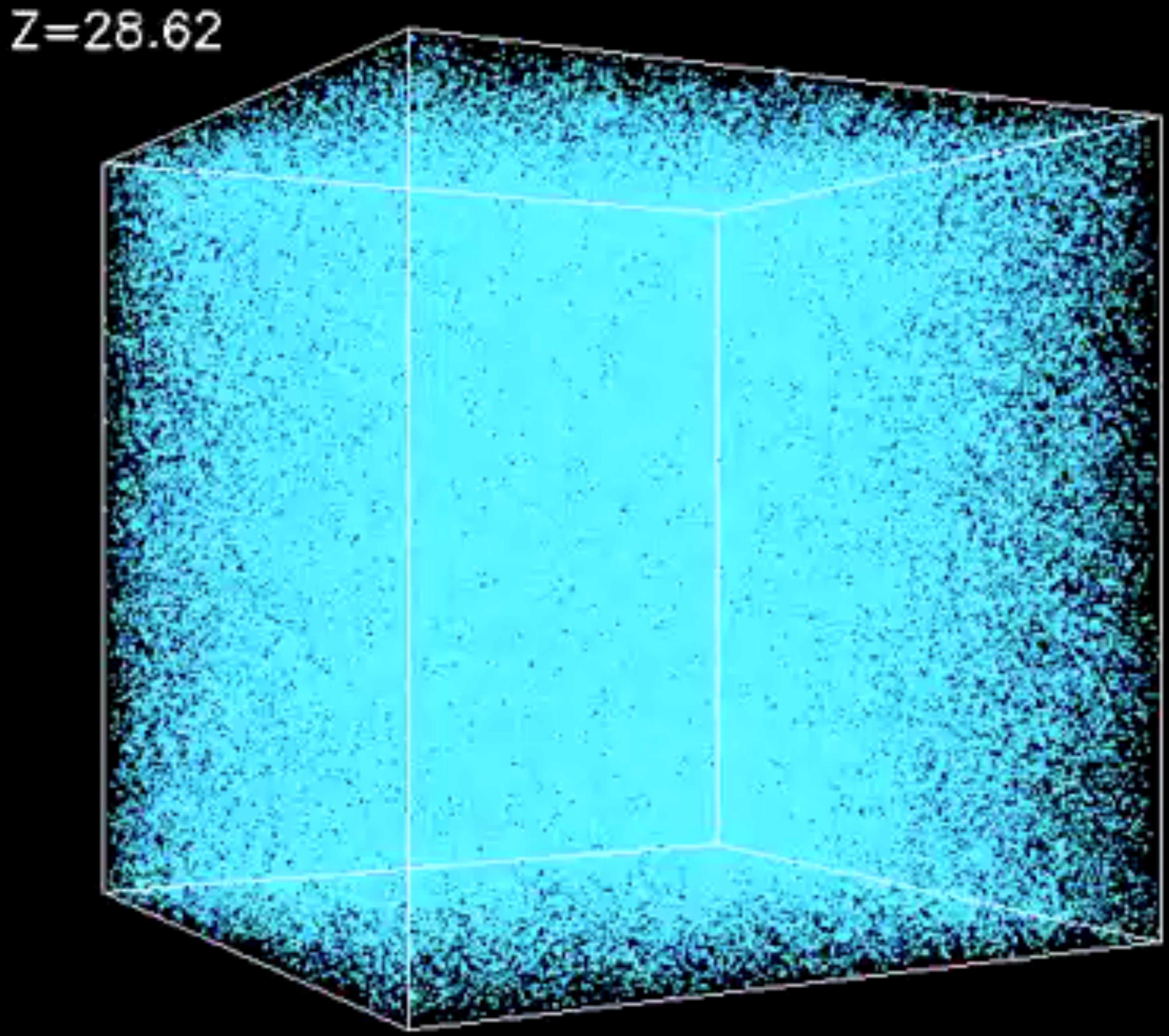

Merging/Growth History of DM Halos

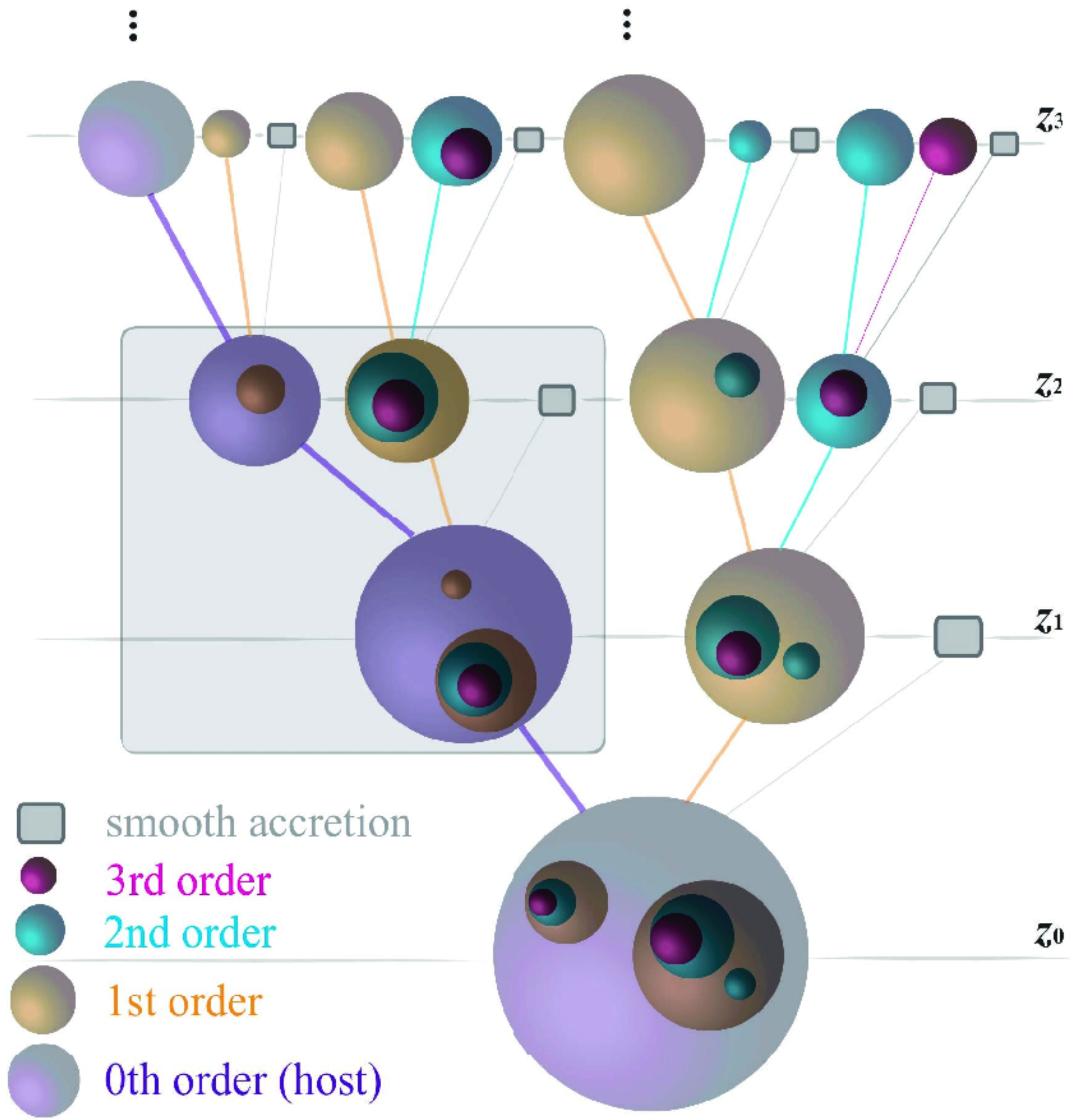

Finding Dark Matter Halos in Simulated Data

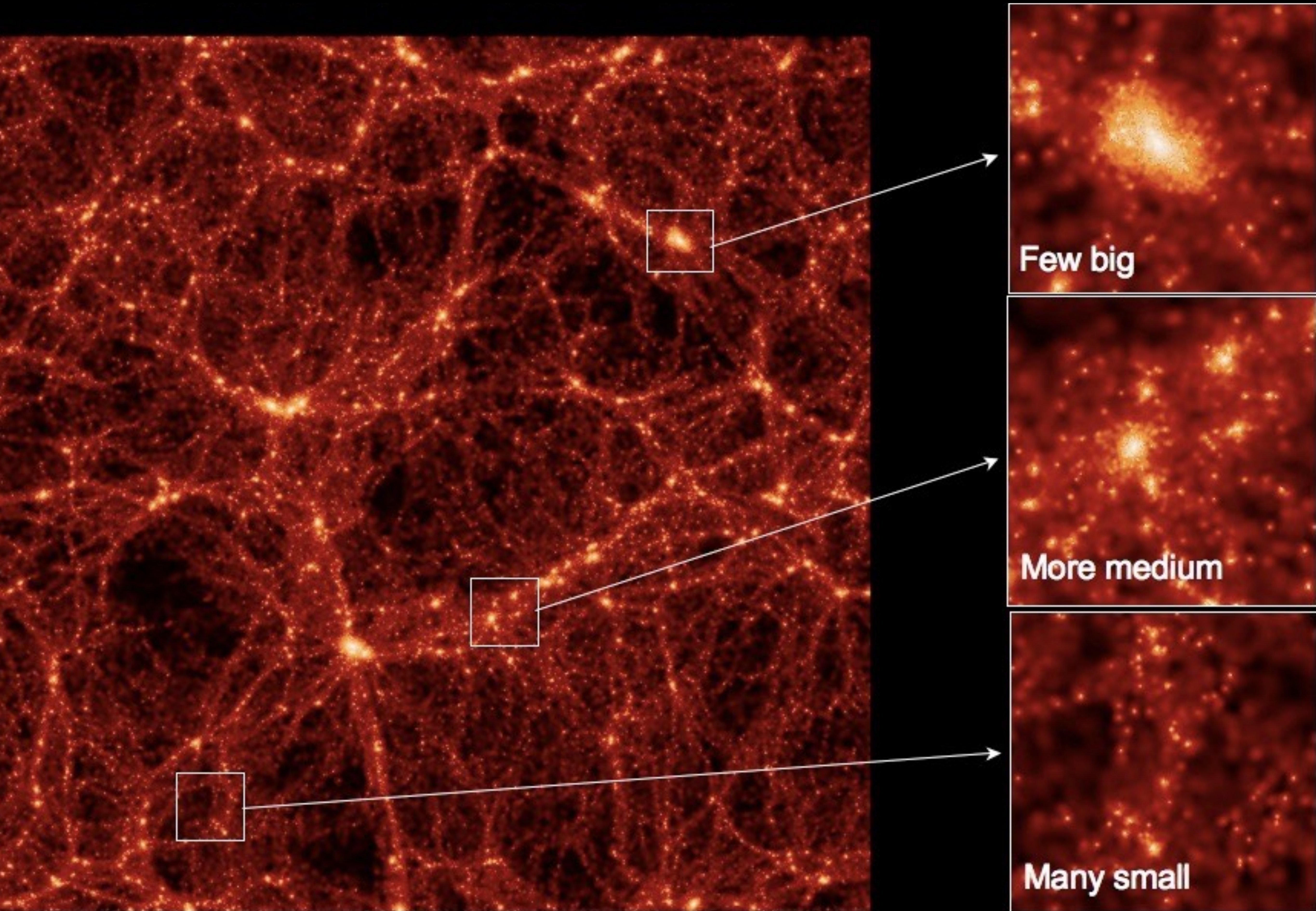

Virialization of a DM Halo from an N-body Simulation

BT Figs 4.28-30

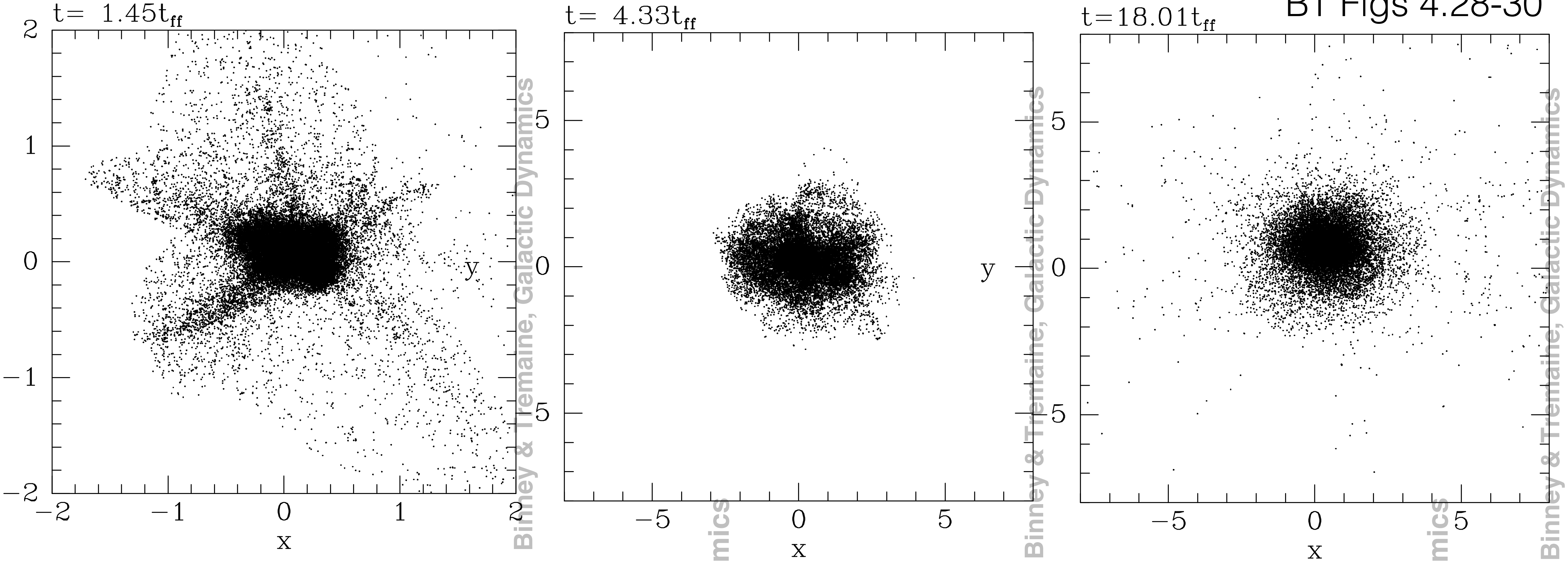

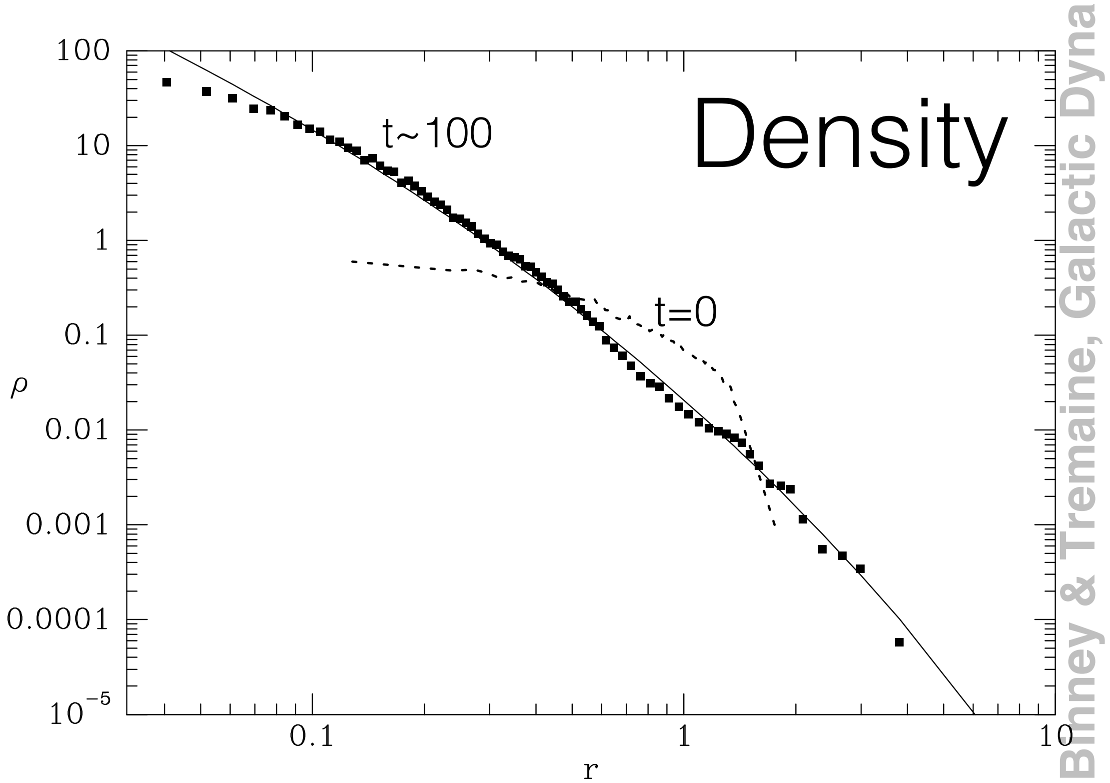

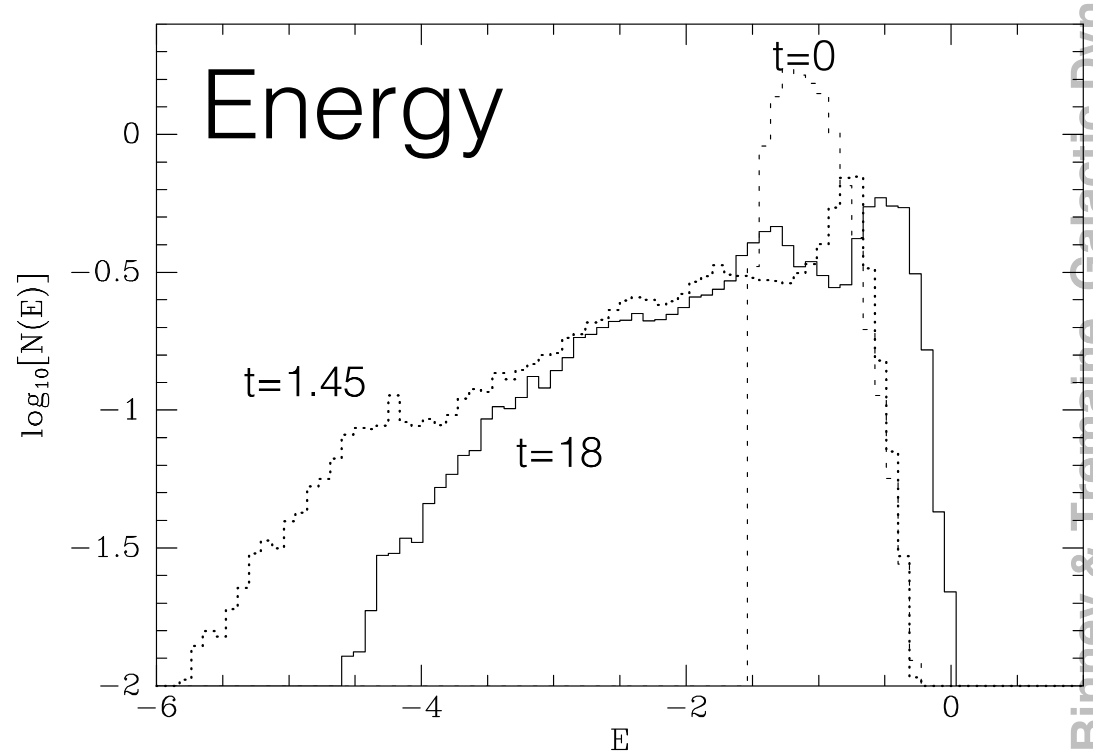

Navarro-Frenk-White (1996) Profile

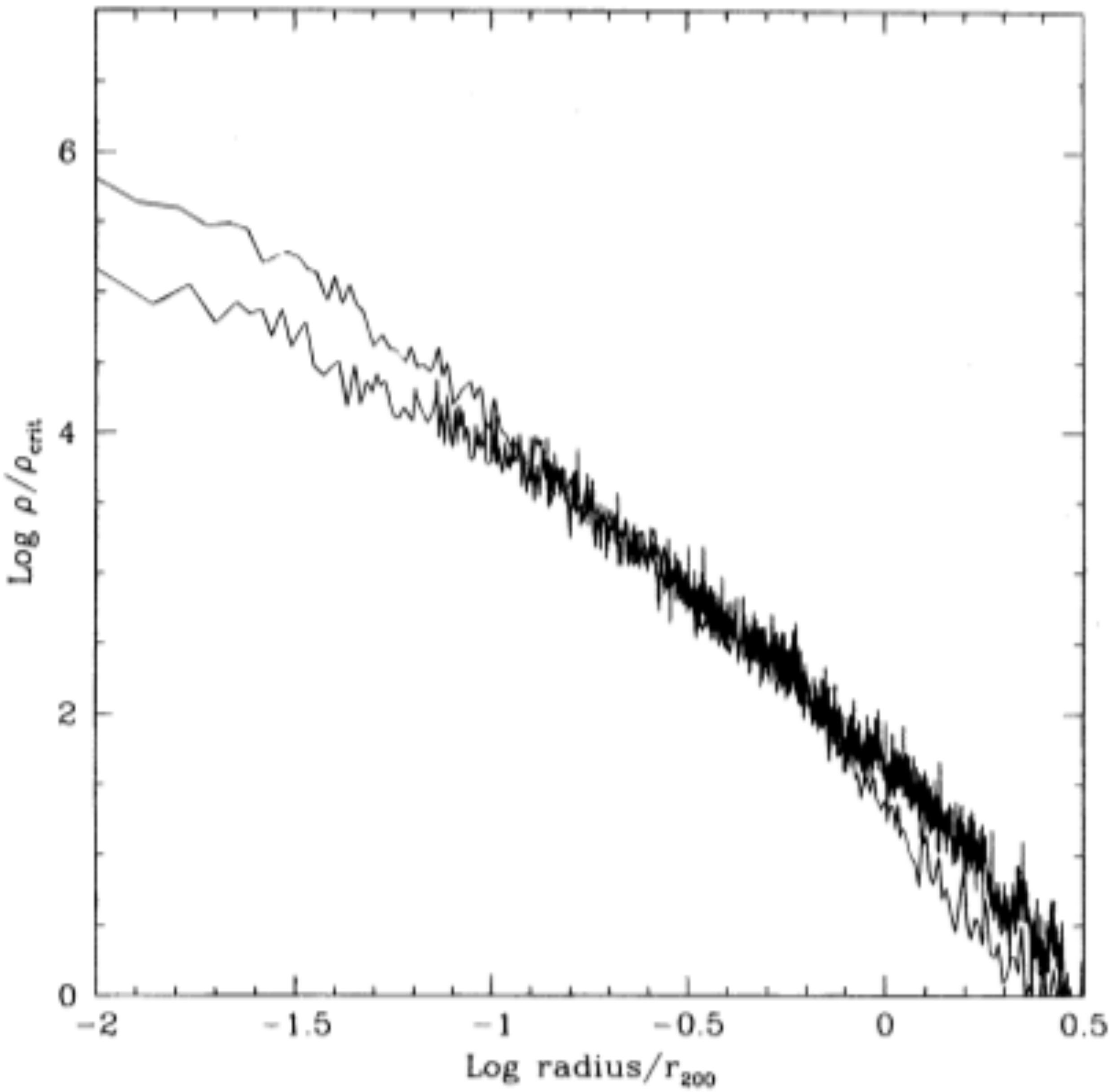

FIG. 4.—Scaled density profiles of the most and least massive halos shown in Fig. 3. The large halo is less centrally concentrated than the less massive system.

Spherical Symmetry is assumed

$$\rho(r) = \frac{\delta_c \rho_c}{(r/r_s)(1 + r/r_s)^2}$$

$$\frac{\rho(r)}{\rho_{\rm crit}} = \frac{\delta_c}{(r/r_s)(1 + r/r_s)^2}\,, \tag{3}$$

where $r_s = r_{200}/c$ is a characteristic radius and $\rho_{\rm crit} = 3H^2/8\pi G$ is the critical density (H is the current value of Hubble's constant); δ_c and c are two dimensionless parameters. Note that r_{200} determines the mass of the halo, $M_{200} = 200\rho_{\rm crit}(4\pi/3)r_{200}^3$, and that δ_c and c are linked by the requirement that the mean density within r_{200} should be $200 \times \rho_{\rm crit}$. That is,

$$\delta_c = \frac{200}{3} \frac{c^3}{[\ln(1 + c) - c/(1 + c)]}\,. \tag{4}$$

The Rapid Development of N-body Simulations

Simulation of a Cube 30 Million Light Year Across

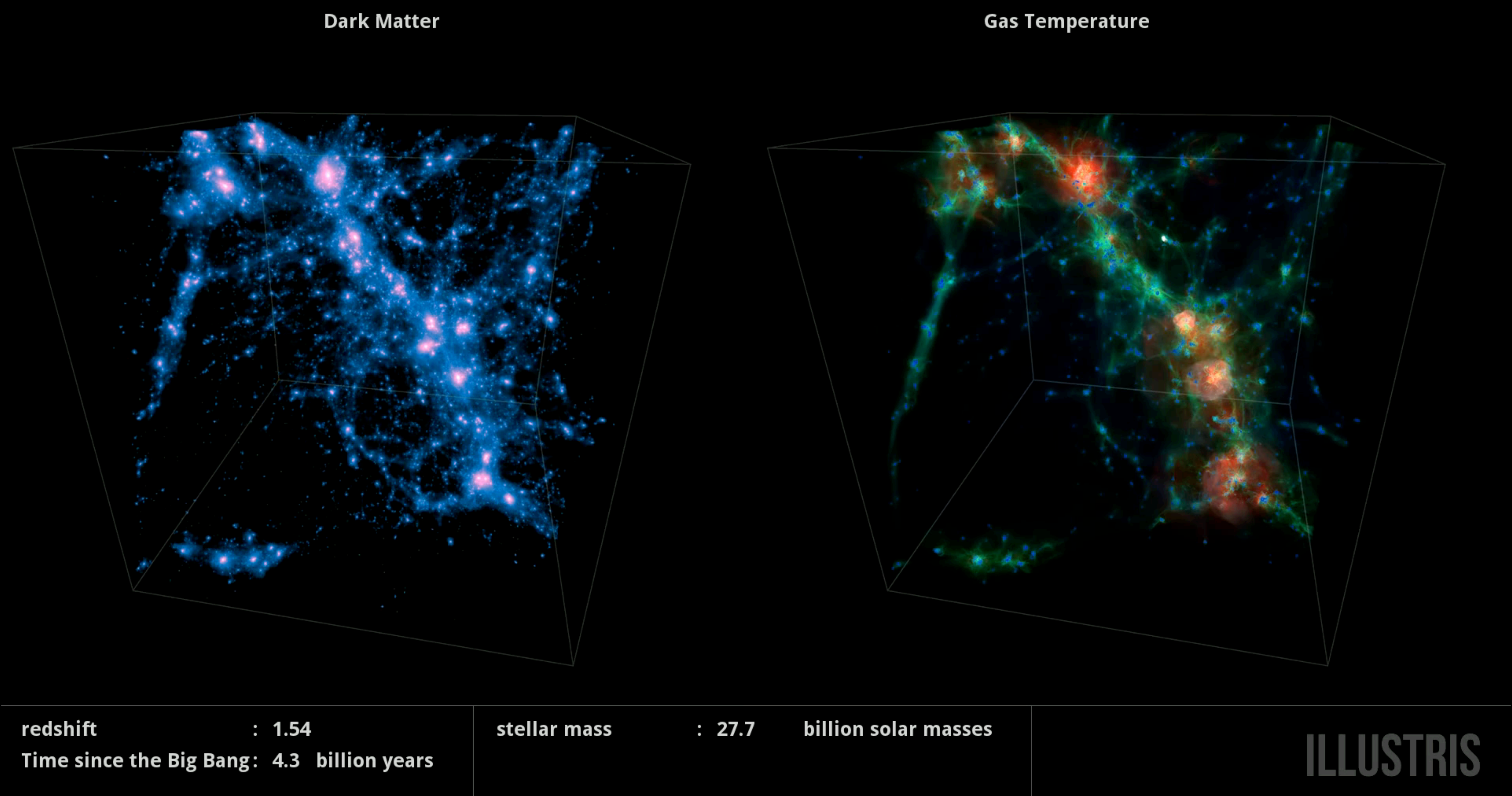

Evolution of N in N-body Simulations

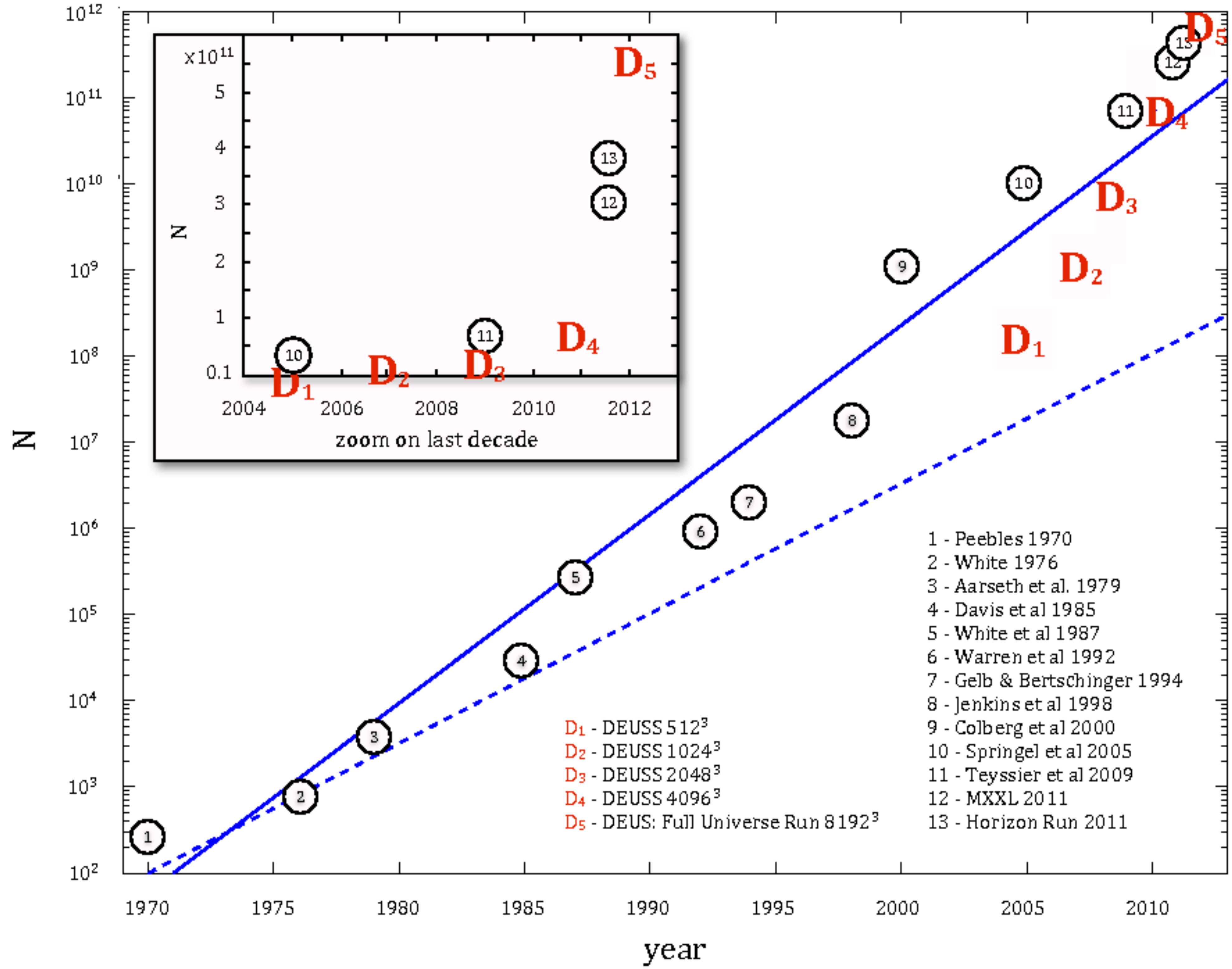

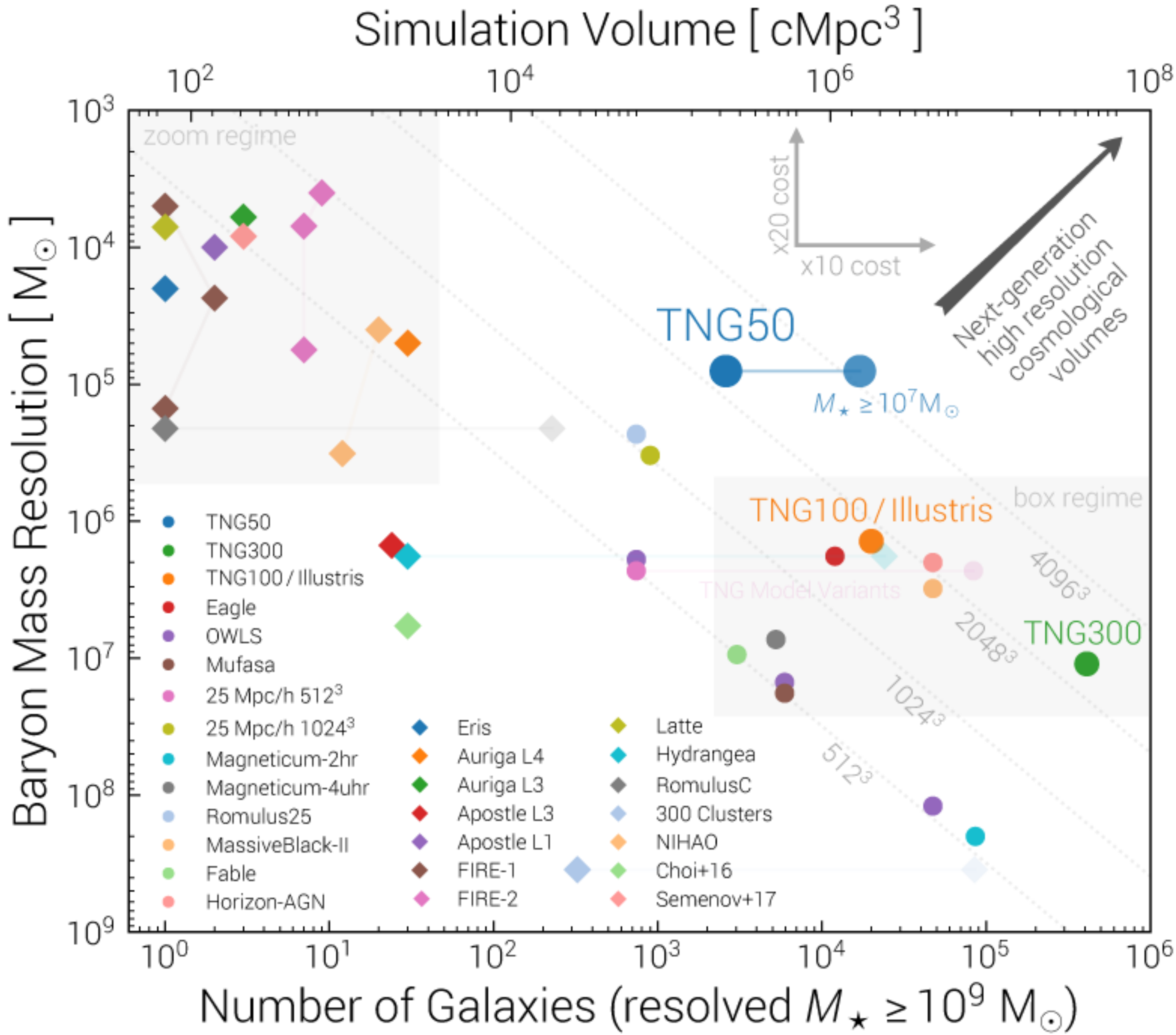

Simulation Volume [cMpc^3]
10^2 10^4 10^6 10^8
Baryon Mass Resolution [$M_\odot$]
10^3 10^4 10^5 10^6 10^7 10^8 10^9
Number of Galaxies (resolved $M_\star \geq 10^9$ $M_\odot$)
10^0 10^1 10^2 10^3 10^4 10^5 10^6
zoom regime
box regime
x20 cost
x10 cost
Next-generation high resolution cosmological volumes
TNG50
$M_\star \geq 10^7 M_\odot$
TNG100 / Illustris
TNG Model Variants
TNG300
4096^3
2048^3
1024^3
512^3
TNG50
TNG300
TNG100 / Illustris
Eagle
OWLS
Mufasa
25 Mpc/h 512^3
25 Mpc/h 1024^3
Magneticum-2hr
Magneticum-4uhr
Romulus25
MassiveBlack-II
Fable
Horizon-AGN
Eris
Auriga L4
Auriga L3
Apostle L3
Apostle L1
FIRE-1
FIRE-2
Latte
Hydrangea
RomulusC
300 Clusters
NIHAO
Choi+16
Semenov+17

		TNG50	TNG100	TNG300
Volume	$[\mathrm{Mpc}^3]$	51.7^3	110.7^3	302.6^3
L_{box}	$[\mathrm{Mpc}/h]$	35	75	205
N_{GAS}	-	2160^3	1820^3	2500^3
N_{DM}	-	2160^3	1820^3	2500^3
N_{TR}	-	2160^3	2×1820^3	2500^3
m_{baryon}	$[\mathrm{M}_\odot]$	8.5×10^4	1.4×10^6	1.1×10^7
m_{DM}	$[\mathrm{M}_\odot]$	4.5×10^5	7.5×10^6	5.9×10^7
$\epsilon_{\mathrm{gas,min}}$	$[\mathrm{pc}]$	74	185	370
$\epsilon_{\mathrm{DM},\star}$	$[\mathrm{pc}]$	288	740	1480

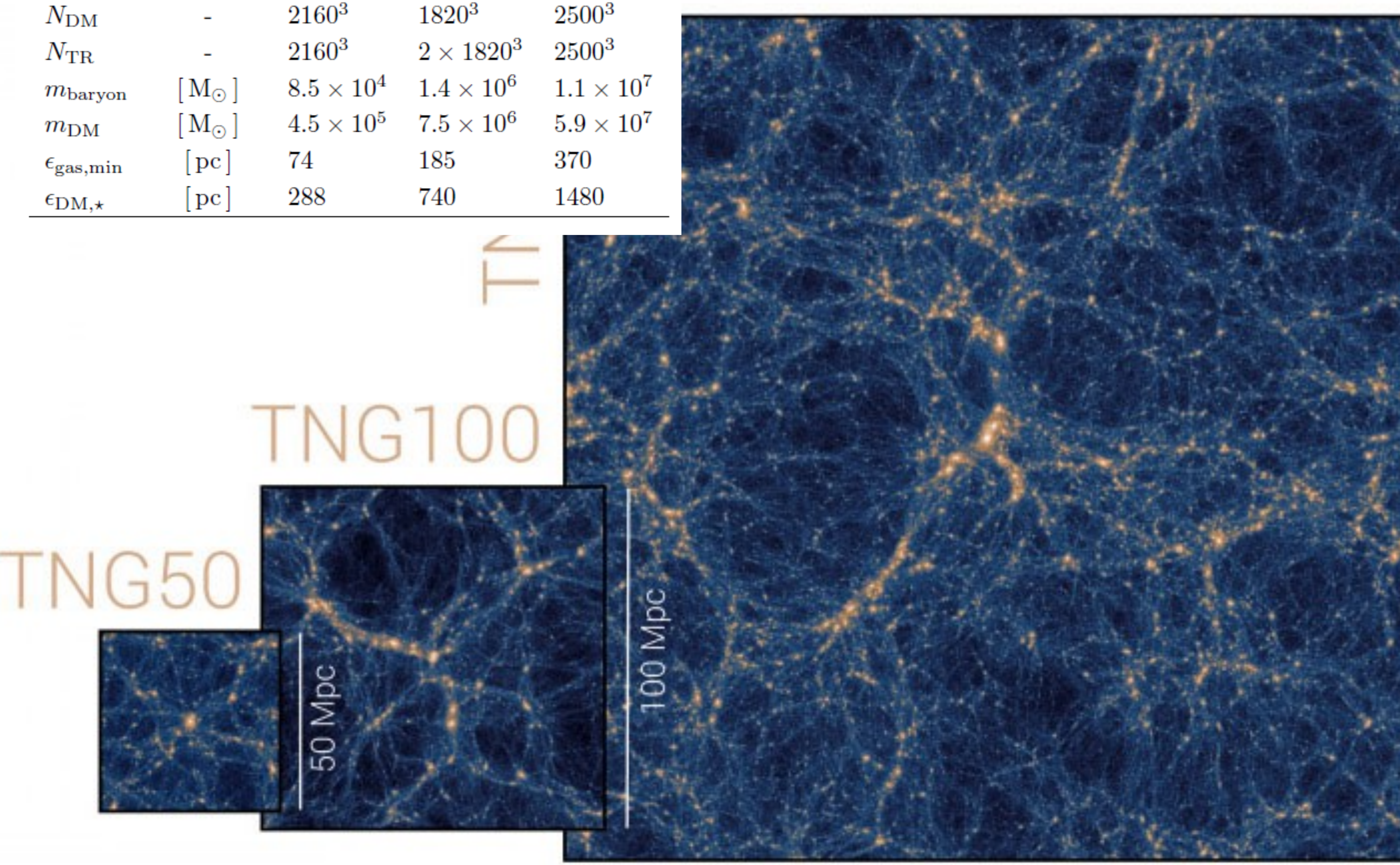

The main *Illustris* simulation was run on the Curie supercomputer at CEA (France) and the SuperMUC supercomputer at the Leibniz Computing Centre (Germany).[1][11] A total of 19 million CPU hours was required, using 8,192 CPU cores.[1] The peak memory usage was approximately 25 TB of RAM.[1] A total of 136 snapshots were saved over the course of the simulation, totaling over 230 TB cumulative data volume.

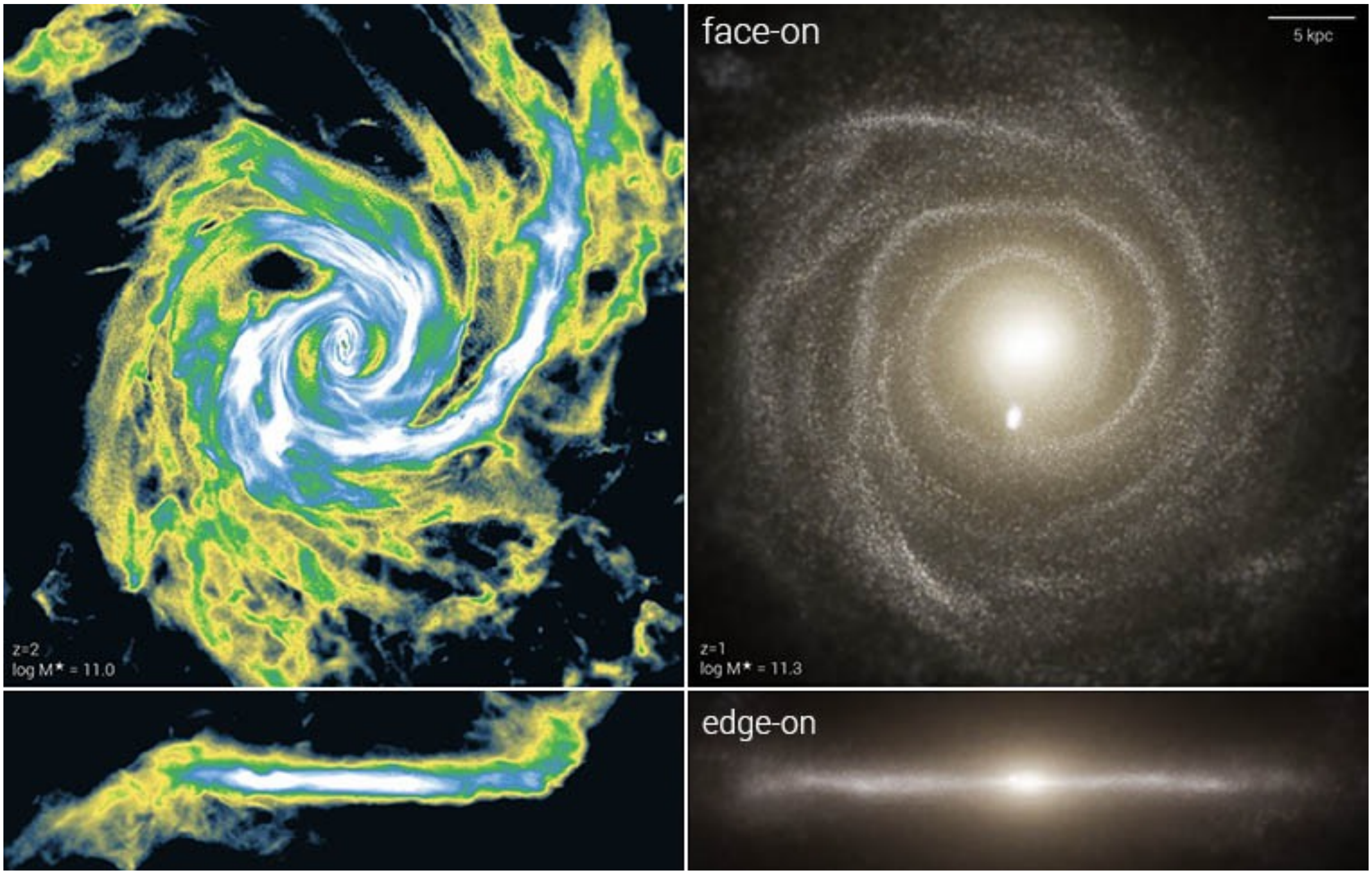

a Milky-Way-like spiral galaxy at z = 2 from TNG50

Carbon Footprint Estimate (DeepSeek)

Rough Estimate:

- **Assumptions**:
  - The simulation used 10,000 CPU cores for 1 year (8,760 hours).
  - Each CPU core consumes ~100 watts (0.1 kW) on average.
  - The data center uses a mix of energy sources with an average carbon intensity of 0.5 kg CO_2 per kWh (this varies widely by location).
- **Calculation**:
  - Total energy consumption = 10,000 cores × 0.1 kW/core × 8,760 hours = 8,760,000 kWh.
  - Carbon footprint = 8,760,000 kWh × 0.5 kg CO_2/kWh = 4,380,000 kg CO_2 (4,380 metric tons of CO_2).

Context:

- 4,380 metric tons of CO_2 is roughly equivalent to the annual emissions of about 950 average passenger vehicles or the energy use of about 500 homes for a year.

Dark Matter Particles:
Cold vs. Hot
MACRO vs. WIMP

Cold Dark Matter (>MeV, moving slowly) vs.
Hot/Warm Dark Matter (10s eV, moving relativistically)
e- mass: 0.511 MeV, p+ mass: 938 MeV

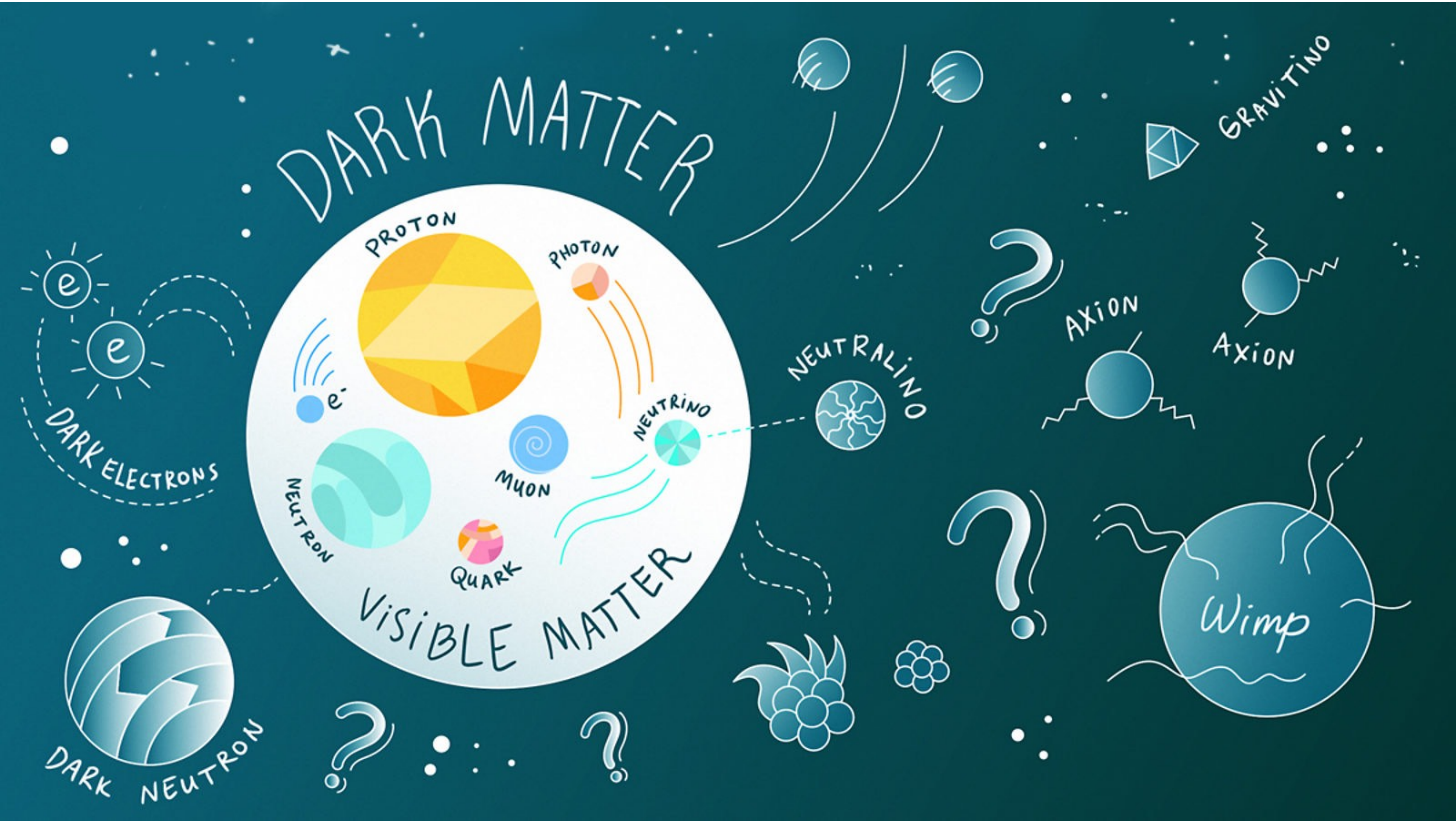

Hot, warm, cold DM simulations

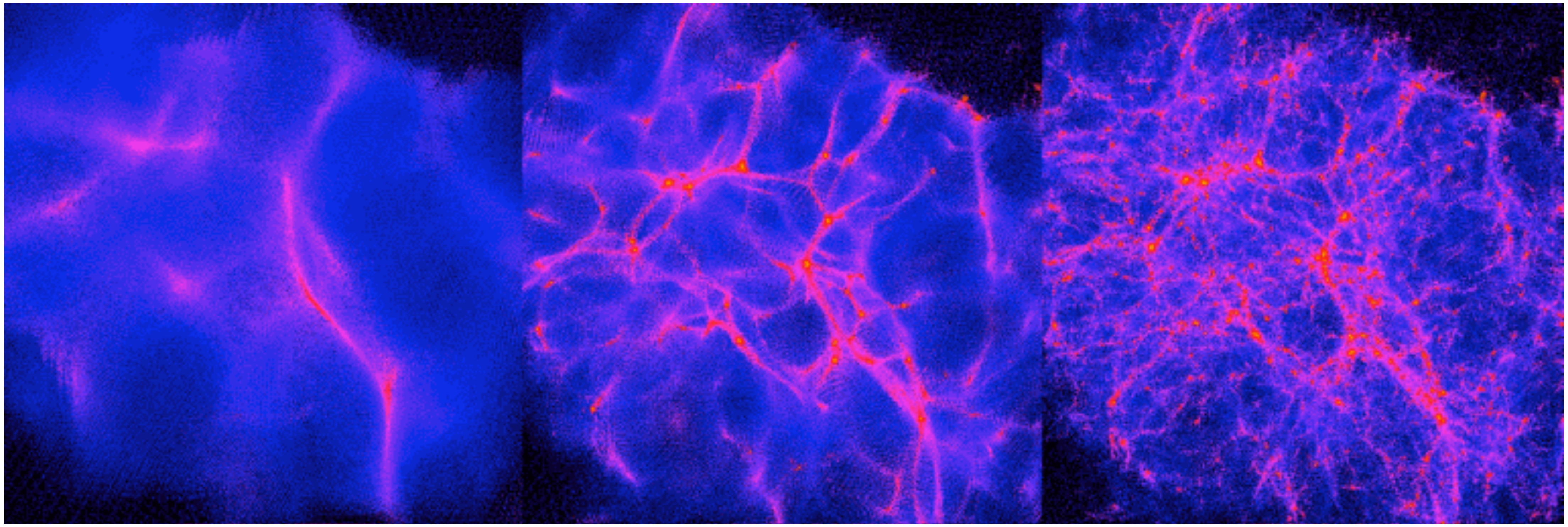

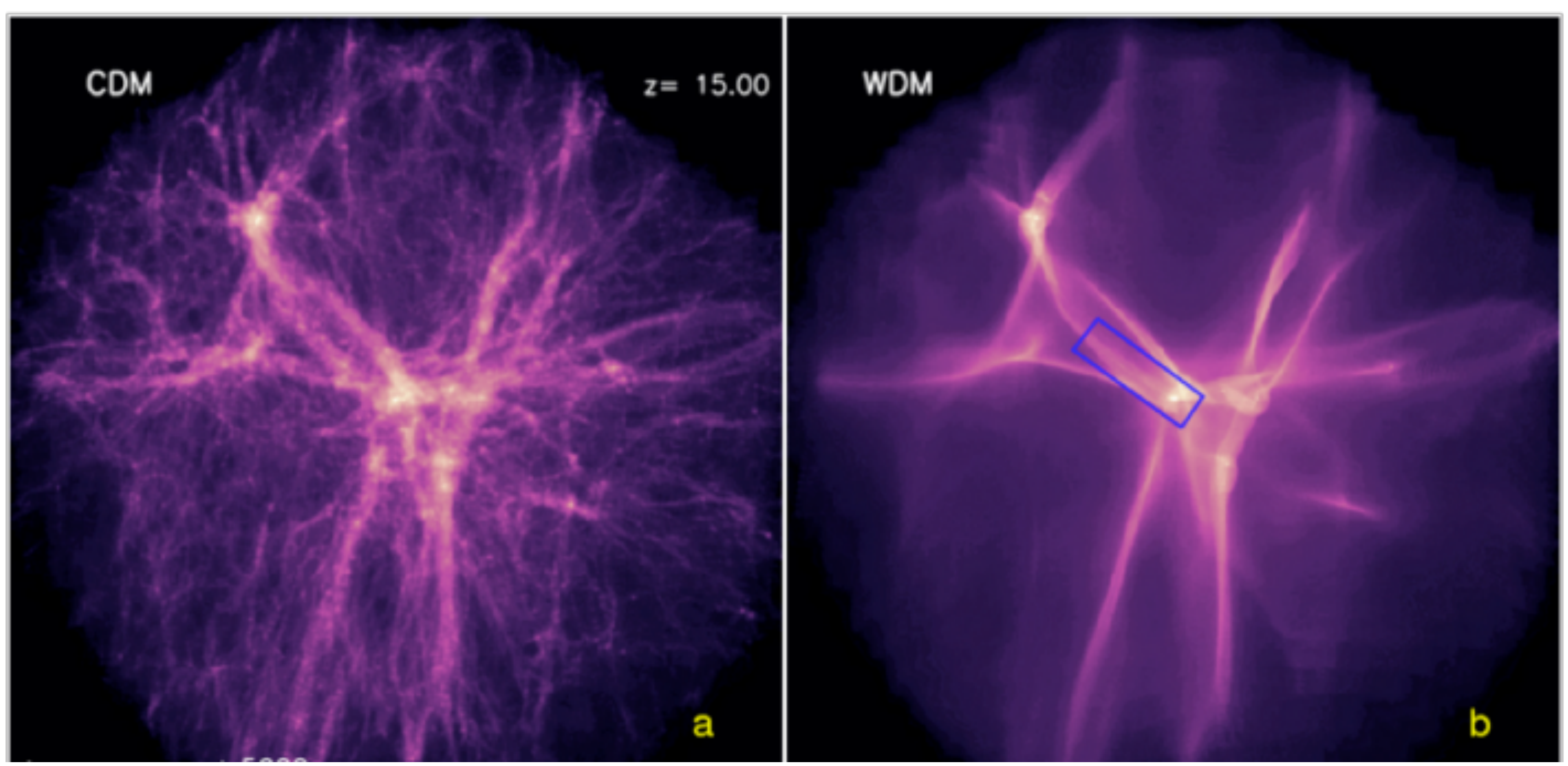

Cold Dark Matter (>MeV) vs. Hot Dark Matter (10s eV, relativistic)

HDM erase density fluctuations on small scales

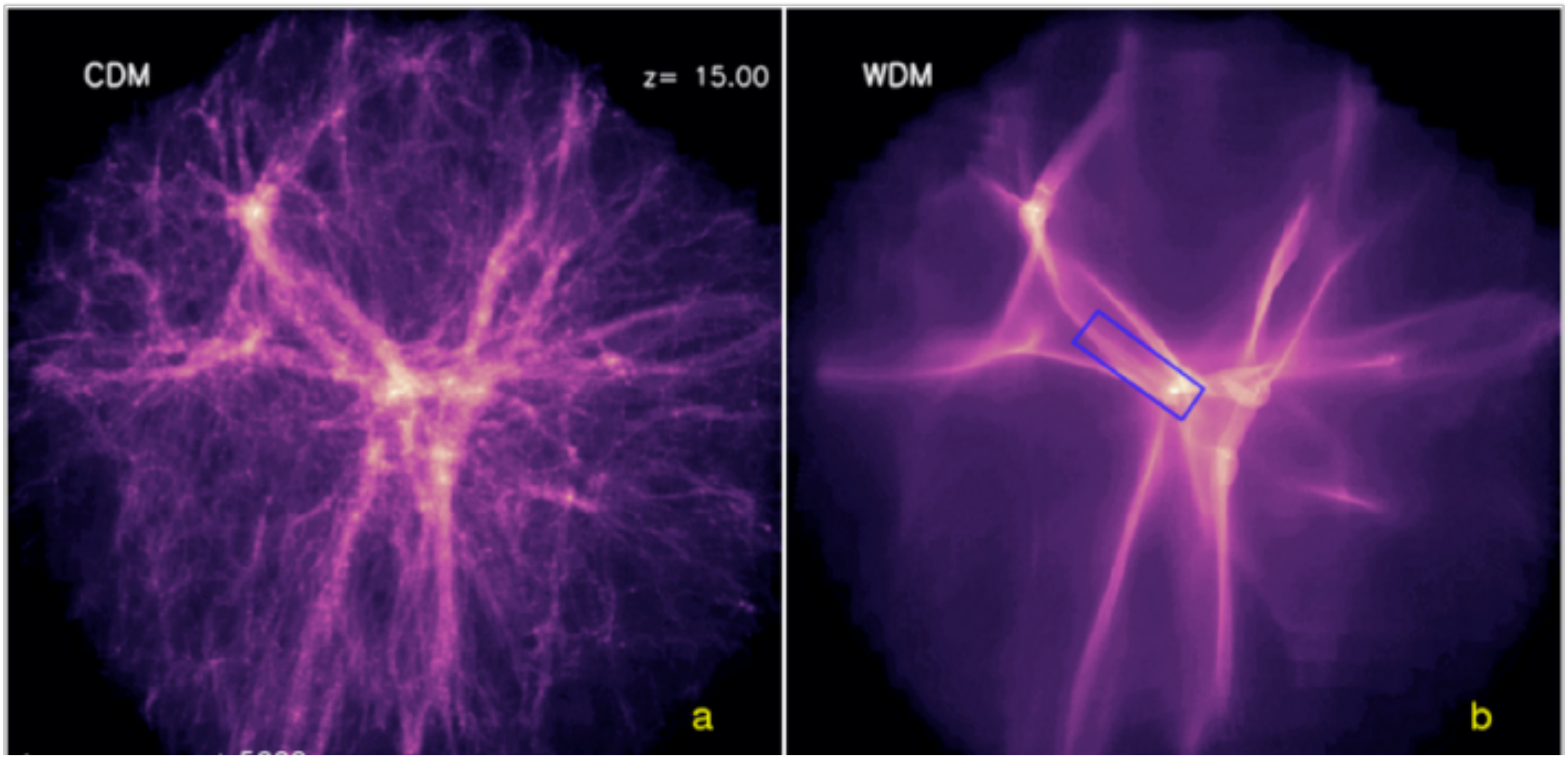

Cosmological Dark Matter Simulations

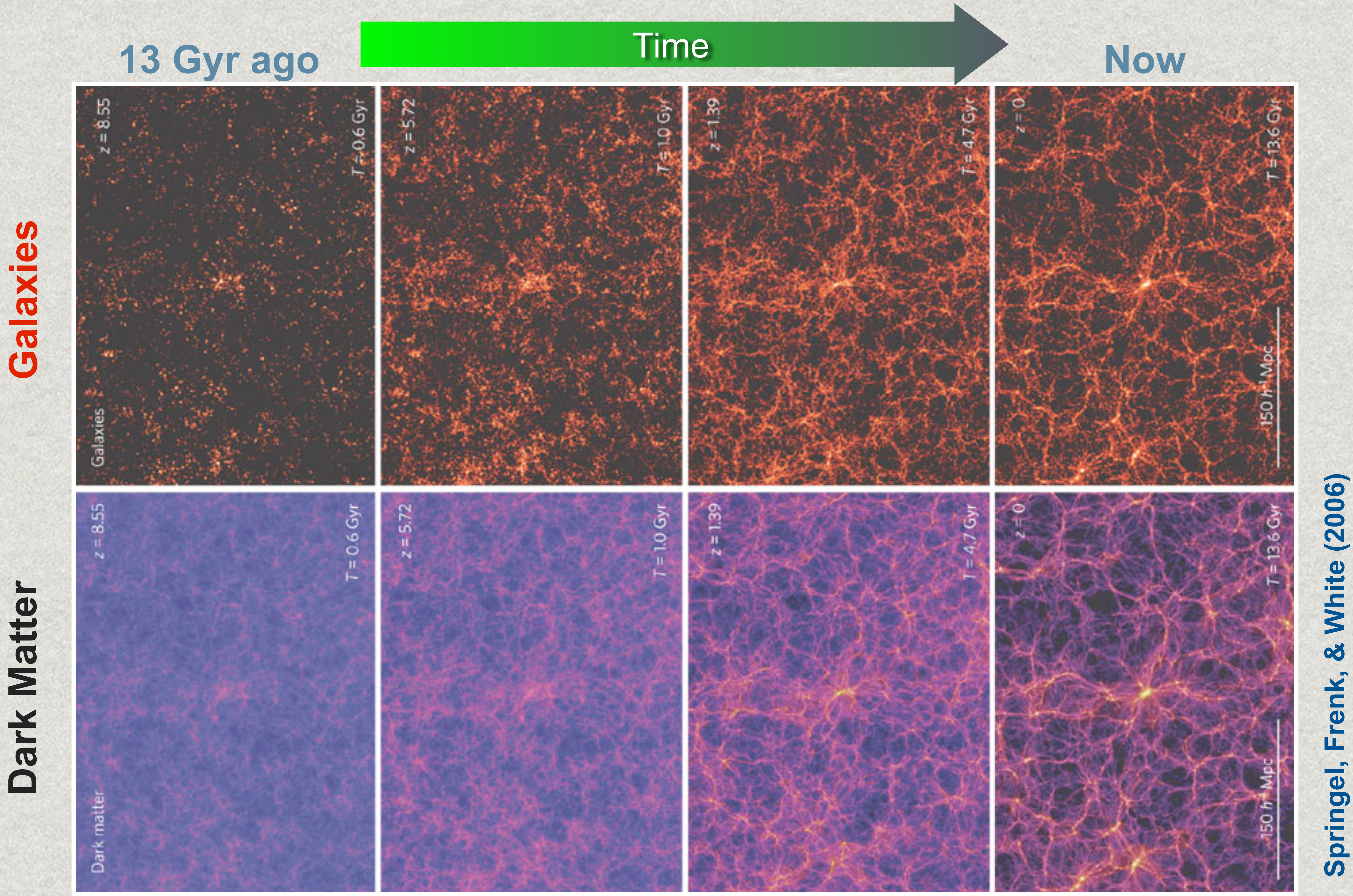

Distribution of Galaxies from Cold DM Simulations

Observed Universe

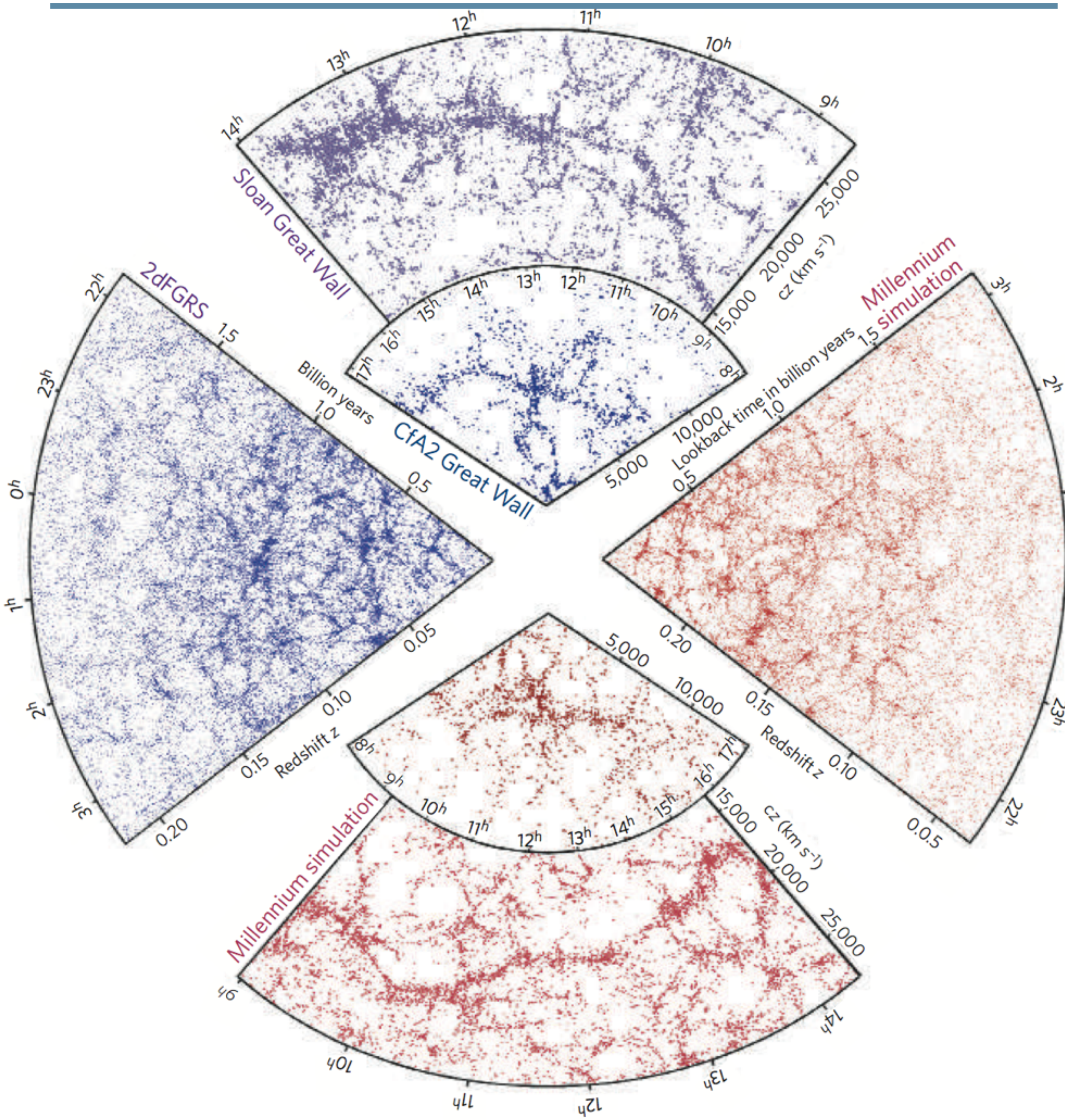

Simulated Universe

Springel, Frenk, & White (2006)

Cold Dark Matter: Particles or Compact Objects?

- No direct detection of dark matter has been made, but there are two broad categories of candidates:
  - **MACHOs** — massive compact halo objects with masses larger than 10^{-8} M_{sun}, such as planets, stars, white dwarfs, neutron stars, or stellar-mass black holes
  - **WIMPs** — weakly interacting massive particles; some fundamental particles like neutrinos but much more massive. Details of WIMP particles are unknown.

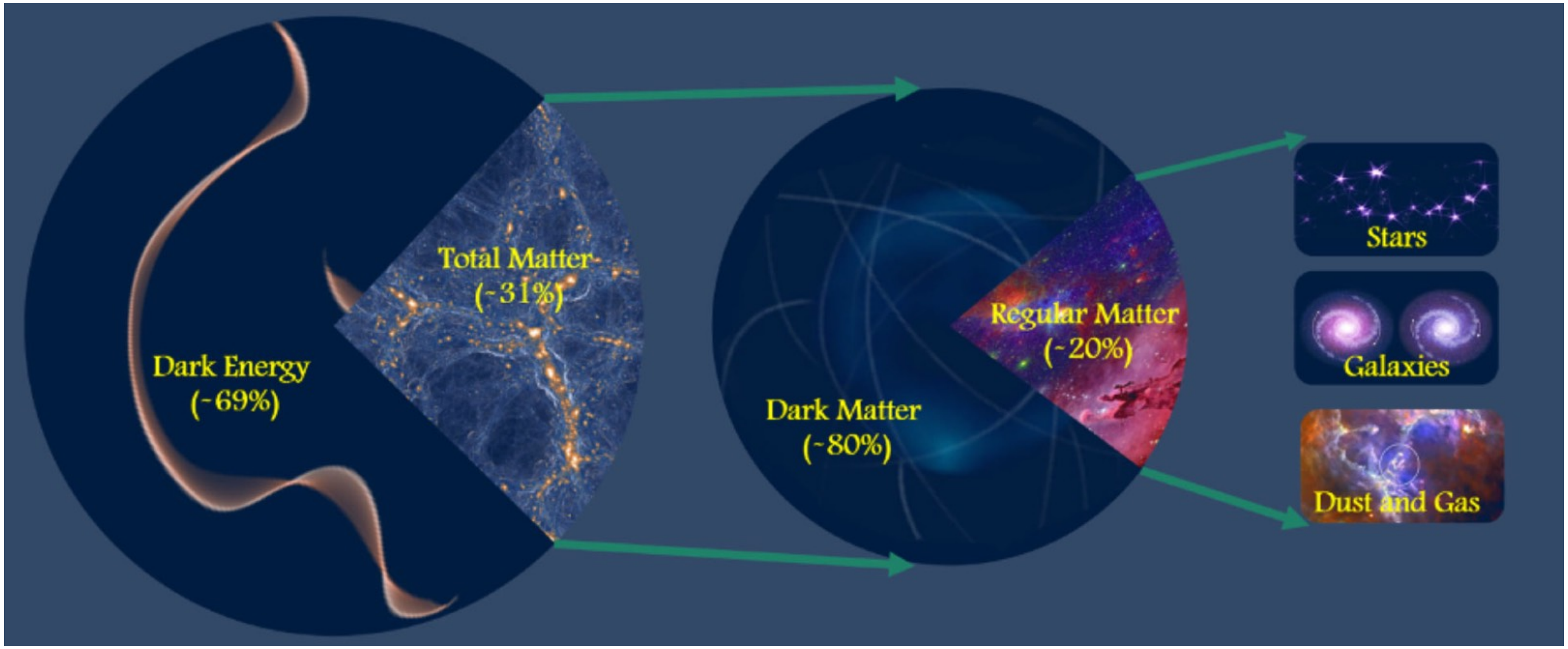

Detecting MACHOs with gravitational micro-lensing

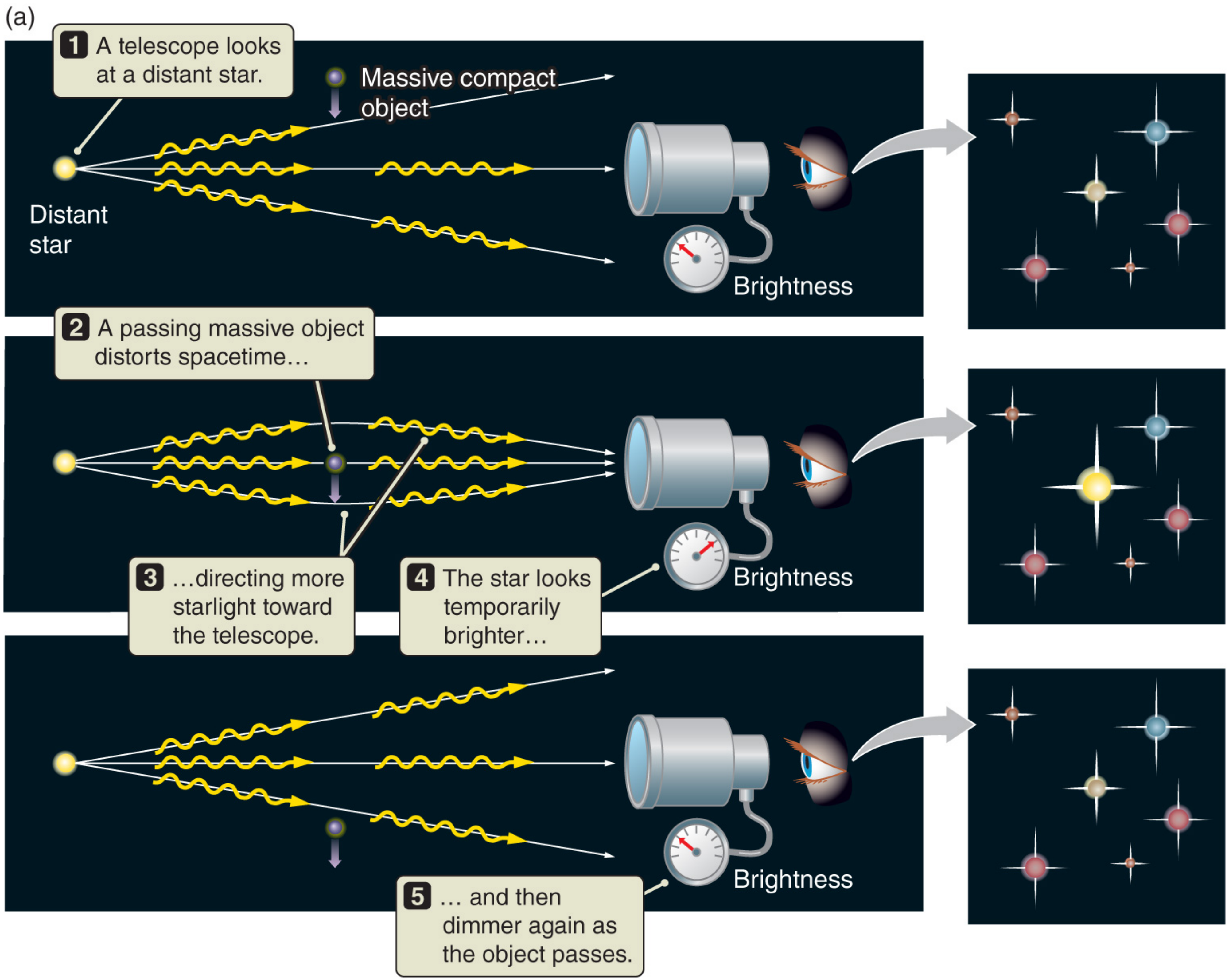

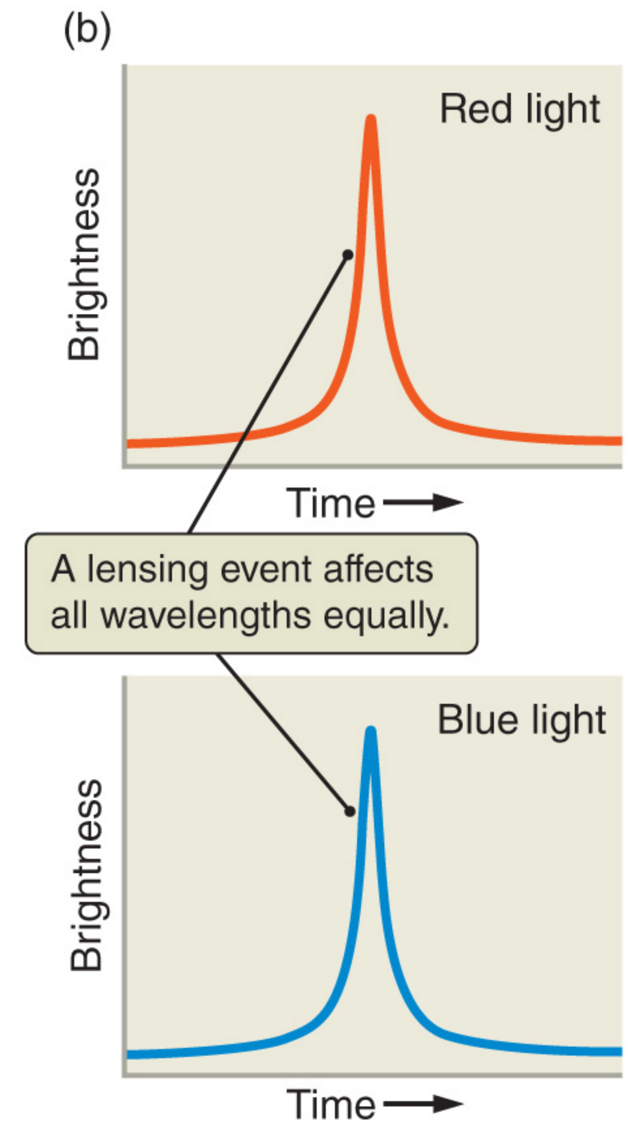

Timescale of a **microlensing** event increases w/ the mass of the MACHO

$$\langle \hat{t} \rangle \sim 130\sqrt{m/M_\odot}\ \text{days}.$$

Microlensing surveys place strict upper limits on the MACHO fraction

- Two years of data on 9 million stars in LMC found 0 microlensing event.
- Even **planet-mass MACHOs** contribute **less than 10%** of halo mass
- These results make **WIMPs** the currently favored DM candidate.

EROS AND MACHO COMBINED LIMITS ON PLANETARY-MASS DARK MATTER IN THE GALACTIC HALO

C. Alcock,[1,2] R. A. Allsman,[3] D. Alves,[1,4] R. Ansari,[5] É. Aubourg,[6] T. S. Axelrod,[7] P. Bareyre,[6,8] J.-Ph. Beaulieu,[9,10] A. C. Becker,[2,11] D. P. Bennett,[1,2,12] S. Brehin,[6] F. Cavalier,[5] S. Char,[13] K. H. Cook,[1,2] R. Ferlet,[9] J. Fernandez,[13] K. C. Freeman,[7] K. Griest,[2,14] Ph. Grison,[9] M. Gros,[6] C. Gry,[15] J. Guibert,[16] M. Lachièze-Rey,[6] B. Laurent,[6] M. J. Lehner,[17] É. Lesquoy,[6] C. Magneville,[6] S. L. Marshall,[1,2] É. Maurice,[18] A. Milsztajn,[6] D. Minniti,[1] M. Moniez,[5] O. Moreau,[16] L. Moscoso,[6] N. Palanque-Delabrouille,[6] B. A. Peterson,[7] M. R. Pratt,[19] L. Prévôt,[18] F. Queinnec,[6] P. J. Quinn,[20] C. Renault,[6,21] J. Rich,[6] M. Spiro,[6] C. W. Stubbs,[2,7,11] W. Sutherland,[22] A. Tomaney,[2,11] T. Vandehei,[2,14] A. Vidal-Madjar,[9] L. Vigroux,[6] and S. Zylberajch[6]

Received 1998 March 9; accepted 1998 March 19; published 1998 May 4

ABSTRACT

The EROS and MACHO collaborations have each published upper limits on the amount of planetary-mass dark matter in the Galactic halo obtained from gravitational microlensing searches. In this Letter, the two limits are combined to give a much stronger constraint on the abundance of low-mass MACHOs. Specifically, objects with masses $10^{-7}\ M_\odot \lesssim m \lesssim 10^{-3}\ M_\odot$ make up less than 25% of the halo dark matter for most models considered, and less than 10% of a standard spherical halo is made of MACHOs in the $3.5 \times 10^{-7}\ M_\odot < m < 4.5 \times 10^{-5}\ M_\odot$ mass range.

Subject headings: dark matter — gravitational lensing — stars: low-mass, brown dwarfs

Potential Theory

Potential-Density Pairs

Keplerian Orbits in the Solar System

Circular velocity: $v(r) = \sqrt{GM(r)/r} \Rightarrow v(r) \propto 1/\sqrt{r}$

because **the Sun** contains 99.9% of the mass!

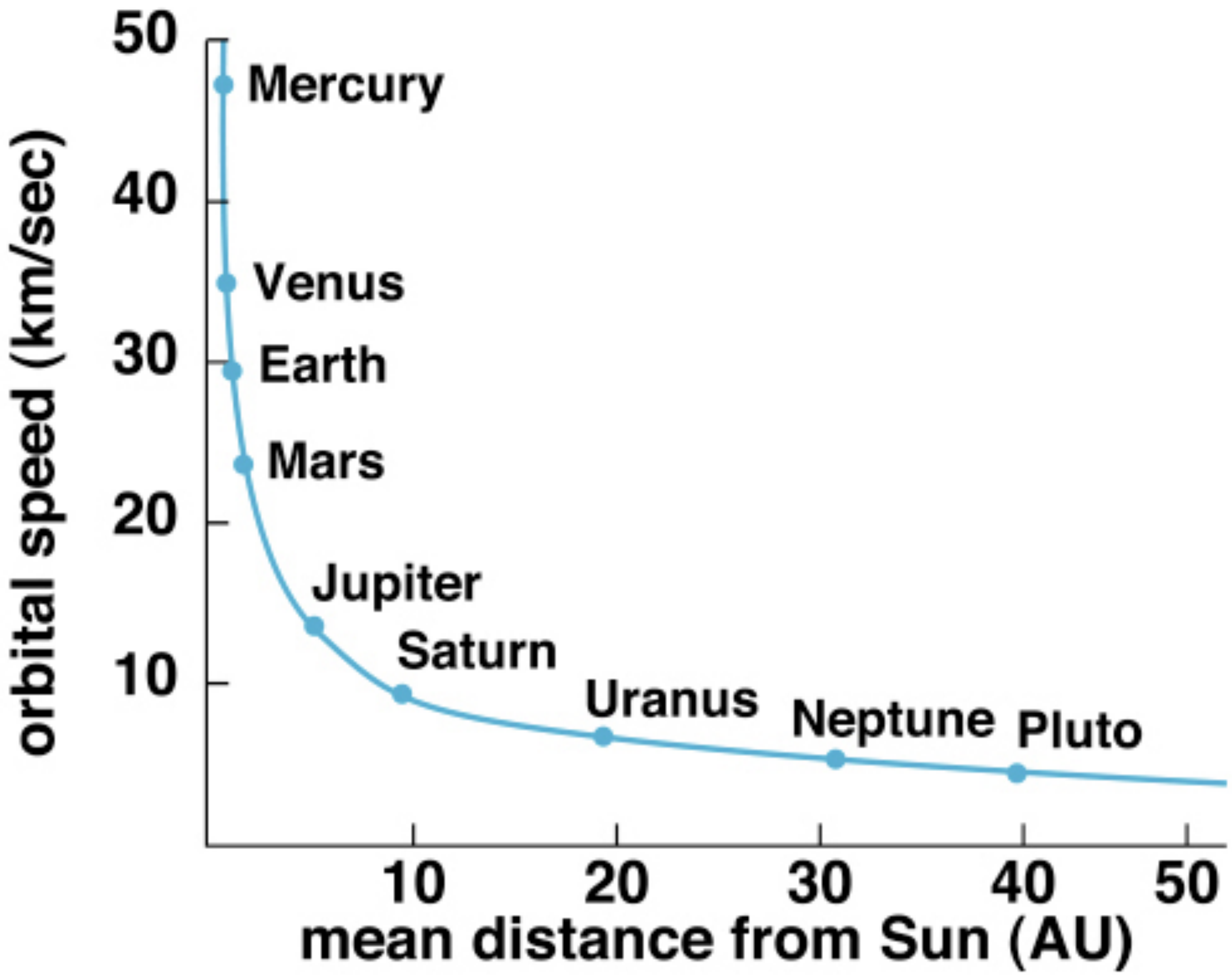

Chaotic Orbits of Galaxies in Clusters

Zwicky 1933: **velocity dispersion** of galaxies in the Coma Cluster

Virial Theorem: $2\bar{K} + \bar{U} = 0 \rightarrow \sigma^2 = GM/R \rightarrow M = \sigma^2 R/G$

The virial mass is **400x** greater than visible stellar mass

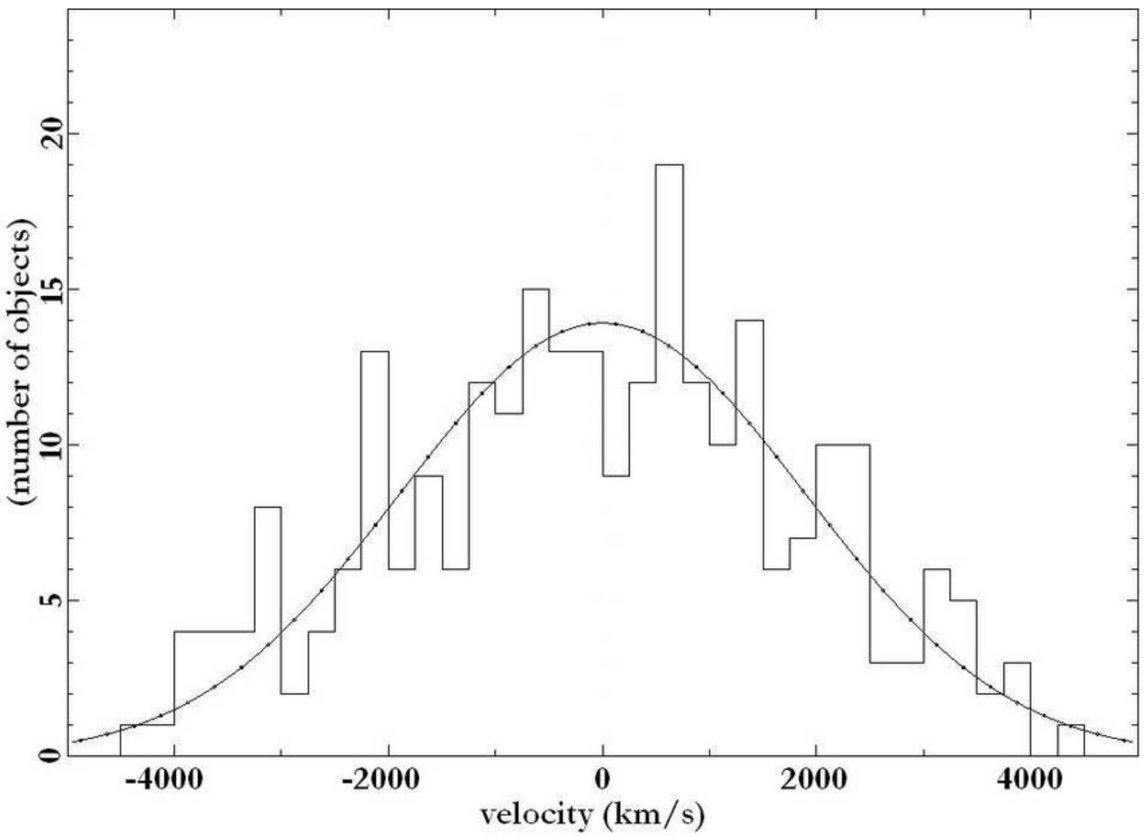

Gaussian Probability Density Function

$$p(x) = \frac{1}{\sigma\sqrt{2\pi}} e^{-\frac{1}{2}\left(\frac{x-\mu}{\sigma}\right)^2}$$

where σ is the standard deviation and μ the mean

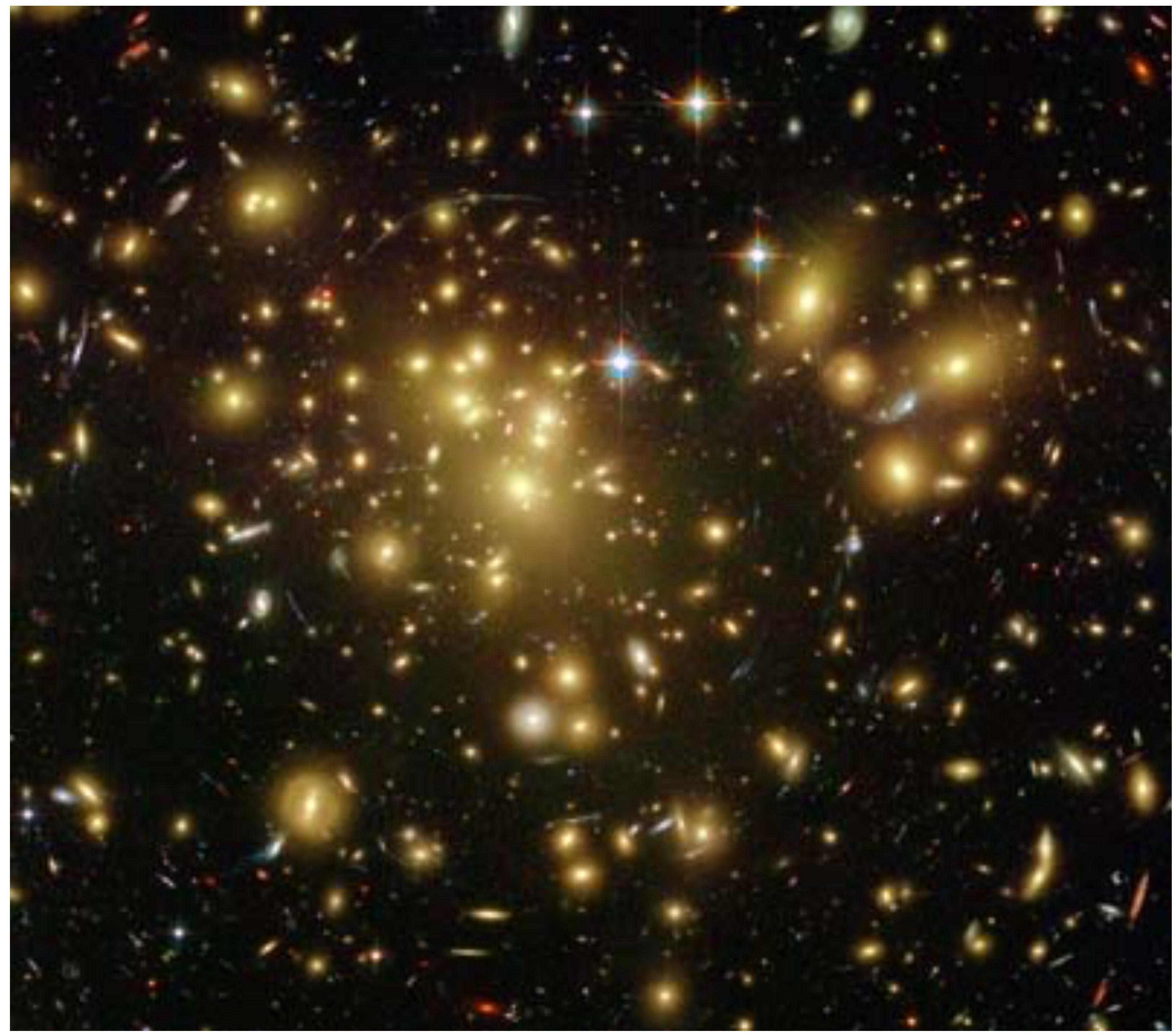

But the Virial Theorem is Not Enough …

All self-gravitating systems in equilibrium must obey the **Virial theorem**, but they display very different morphologies

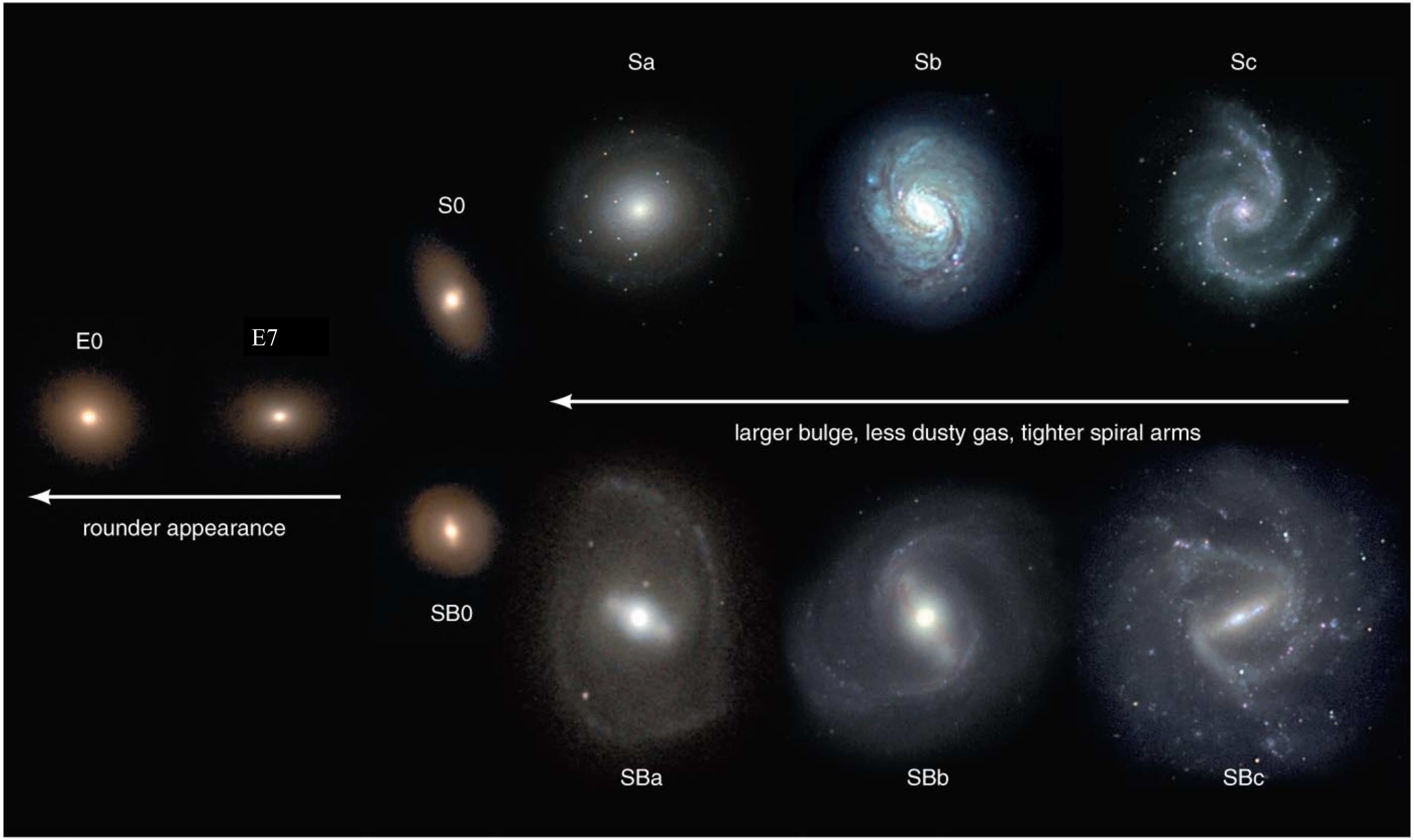

Self-gravitating systems in dynamical equilibrium (general case)

- The mass distribution $\rho(r, \theta, \phi)$ determines gravitational potential $\phi(r, \theta, \phi)$
- The gravitational potential determines the orbits because $\mathbf{g} = -\nabla\phi$
- The orbits determine how much **time** objects spend at each location $\tau(r, \theta, \phi)$, thus determines the **mass distribution** $\rho(r, \theta, \phi)$. We now have a **closed loop**.
- A **special** type of orbits are **circular orbits**, and observers can approximate mean rotation velocity as circular velocities: $v_c(r) = \sqrt{GM(r)/r}$

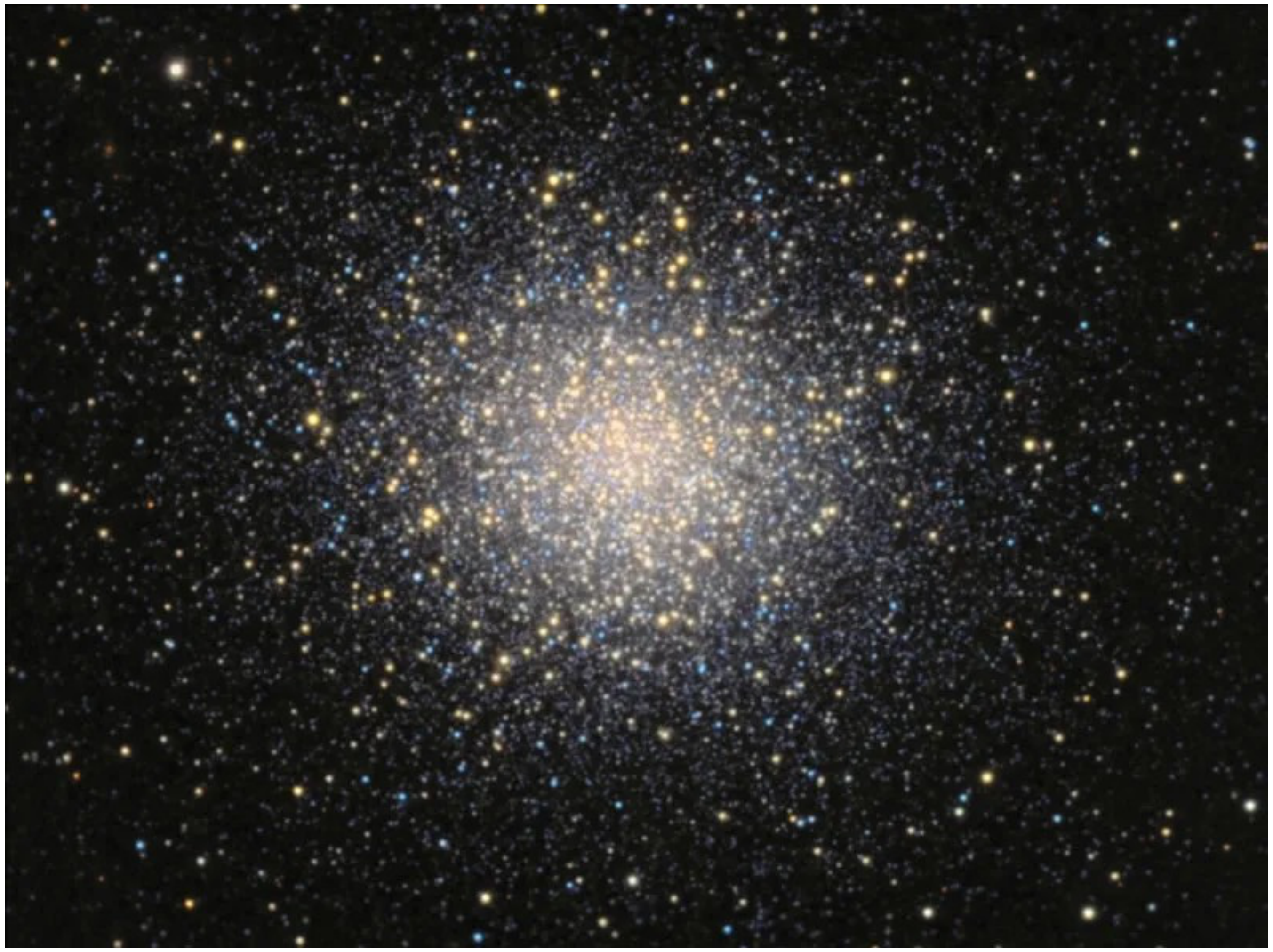

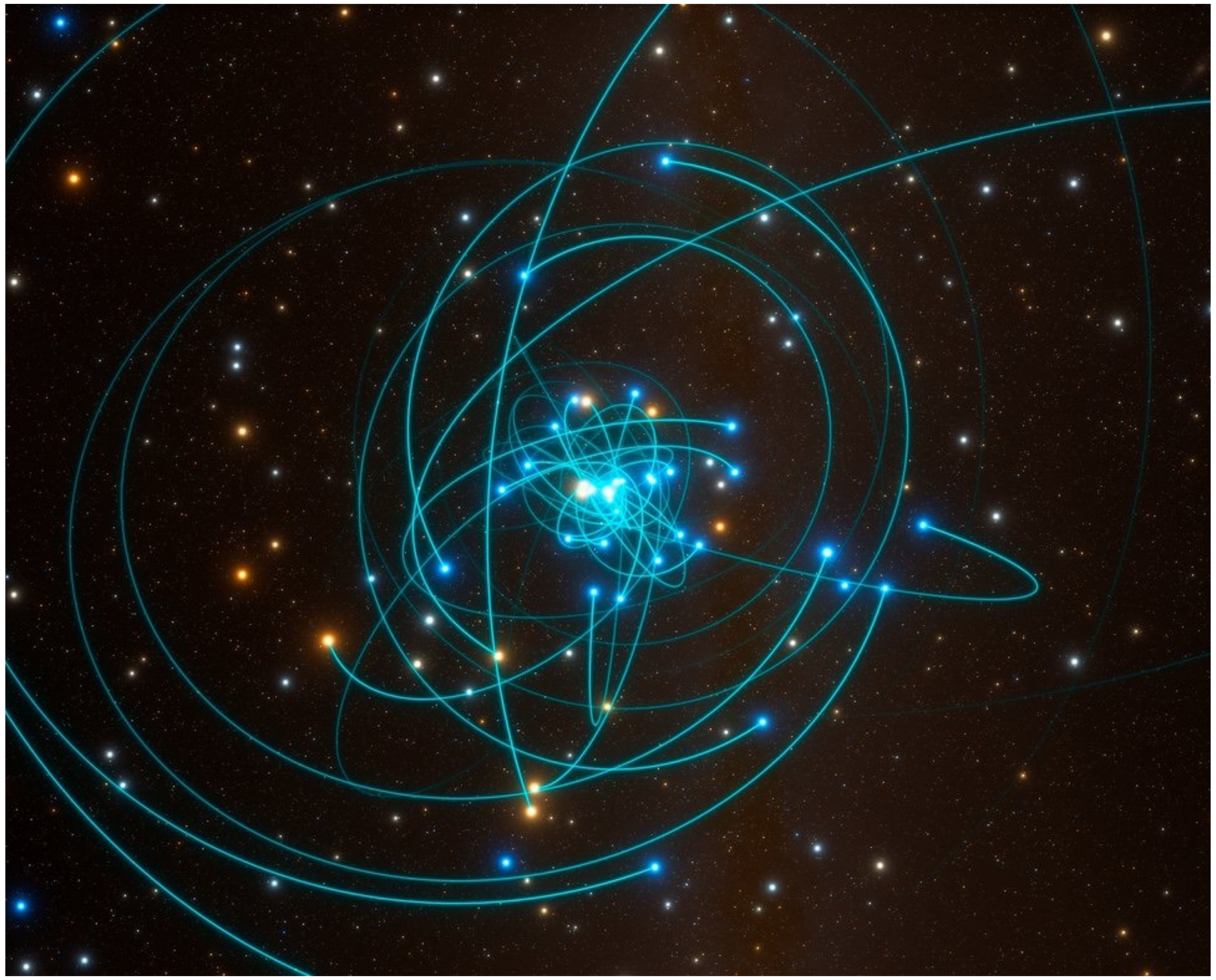

Key Equations Controlling Self-Gravitating Systems

Virial Theorem:

$$\sigma^2 = GM/r, \;\; 2\bar{K} + \bar{U} = 0$$

Equation of motion:

$$\vec{g} = -\nabla\phi$$

Gauss' Law:

$$\oint_S \mathbf{g} \cdot d\mathbf{A} = -4\pi GM$$

Poisson Equation:

$$\nabla^2\phi = 4\pi G\rho$$

Flux Due to a Point Mass

Consider a point mass M located at the center of a spherical surface of radius r. The gravitational field $\mathbf{g}$ at any point on the surface is:

$$\mathbf{g} = -G\frac{M}{r^2}\hat{\mathbf{r}}$$

The flux through the spherical surface is:

$$\oint_S \mathbf{g} \cdot d\mathbf{A}$$

Since $\mathbf{g}$ is radial and constant in magnitude over the sphere, and $d\mathbf{A}$ is also radial, we have:

$$\mathbf{g} \cdot d\mathbf{A} = g\,dA$$

Thus:

$$\oint_S g\,dA = g\oint_S dA = \left(-G\frac{M}{r^2}\right) \cdot 4\pi r^2 = -4\pi GM$$

Multiple Masses and Mass Density

For a system of multiple masses, the total flux through a closed surface is the sum of the fluxes due to each mass enclosed by the surface:

$$\oint_S \mathbf{g} \cdot d\mathbf{A} = -4\pi G \sum M_{\text{enc}}$$

If the mass distribution is continuous, the total enclosed mass M_{enc} can be expressed as an integral over the mass density $\rho(\mathbf{r})$:

$$M_{\text{enc}} = \int_V \rho \, dV$$

where V is the volume enclosed by the surface S.

Thus, Gauss's law for gravity in integral form is:

$$\oint_S \mathbf{g} \cdot d\mathbf{A} = -4\pi G \int_V \rho \, dV$$

Derivation of Poisson Equation

Using the divergence theorem:

$$\oint_S \mathbf{g} \cdot d\mathbf{A} = \int_V (\nabla \cdot \mathbf{g})\, dV$$

Substituting into Gauss's law:

$$\int_V (\nabla \cdot \mathbf{g})\, dV = -4\pi G \int_V \rho\, dV$$

Since this holds for any volume V, the integrands must be equal:

$$\nabla \cdot \mathbf{g} = -4\pi G\rho$$

$$\nabla \cdot (-\nabla\phi) = -4\pi G\rho$$

Gradient & Divergence in Spherical Coordinates

Gradient

The gradient of a scalar function $f(r, \theta, \phi)$ is:

$$\nabla f = \frac{\partial f}{\partial r}\hat{\mathbf{r}} + \frac{1}{r}\frac{\partial f}{\partial \theta}\hat{\theta} + \frac{1}{r\sin\theta}\frac{\partial f}{\partial \phi}\hat{\phi}$$

Here:

- $\hat{\mathbf{r}}$, $\hat{\theta}$, and $\hat{\phi}$ are the unit vectors in the r, θ, and ϕ directions, respectively.

Divergence

The divergence of a vector field $\mathbf{F} = F_r\hat{\mathbf{r}} + F_\theta\hat{\theta} + F_\phi\hat{\phi}$ is:

$$\nabla \cdot \mathbf{F} = \frac{1}{r^2}\frac{\partial (r^2 F_r)}{\partial r} + \frac{1}{r\sin\theta}\frac{\partial(\sin\theta\, F_\theta)}{\partial \theta} + \frac{1}{r\sin\theta}\frac{\partial F_\phi}{\partial \phi}$$

Here:

- F_r, F_θ, and F_ϕ are the components of $\mathbf{F}$ in the r, θ, and ϕ directions, respectively.

Laplacian: The Divergence of the Gradient of a Scaler Field

Laplacian

The Laplacian of a scalar function $f(r, \theta, \phi)$ is:

$$\nabla^2 f = \frac{1}{r^2}\frac{\partial}{\partial r}\left(r^2 \frac{\partial f}{\partial r}\right) + \frac{1}{r^2 \sin\theta}\frac{\partial}{\partial \theta}\left(\sin\theta \frac{\partial f}{\partial \theta}\right) + \frac{1}{r^2 \sin^2\theta}\frac{\partial^2 f}{\partial \phi^2}$$

The gradient of a scalar function $f(r, \theta, \phi)$ is:

$$\nabla f = \frac{\partial f}{\partial r}\hat{\mathbf{r}} + \frac{1}{r}\frac{\partial f}{\partial \theta}\hat{\theta} + \frac{1}{r \sin\theta}\frac{\partial f}{\partial \phi}\hat{\phi}$$

The divergence of a vector field $\mathbf{F} = F_r\hat{\mathbf{r}} + F_\theta\hat{\theta} + F_\phi\hat{\phi}$ is:

$$\nabla \cdot \mathbf{F} = \frac{1}{r^2}\frac{\partial (r^2 F_r)}{\partial r} + \frac{1}{r \sin\theta}\frac{\partial (\sin\theta\, F_\theta)}{\partial \theta} + \frac{1}{r \sin\theta}\frac{\partial F_\phi}{\partial \phi}$$

Spherical Symmetry Systems

General Equations for Spherical Symmetric Systems

Enclosed Mass within r:

$$M(r) = \int_0^r \rho(r')4\pi r'^2 dr'$$

Potential at radius r:

$$\phi(r) = -\frac{G}{r}\int_0^r dM(r') - G\int_r^\infty \frac{dM(r')}{r'}$$

$$= -4\pi G\left[\frac{1}{r}\int_0^r \rho(r)r^2 dr + \int_r^\infty \rho(r) r dr\right]$$

Circular Velocity at radius r:

$$v_c(r) = \sqrt{r\frac{d\phi}{dr}} = \sqrt{\frac{GM(r)}{r}}$$

Singular Isothermal Sphere (SIS)

Density distribution:

$$\rho(r) = \frac{\sigma^2}{2\pi G r^2} \propto r^{-2}$$

Enclosed Mass:

$$M(r) = \int_0^r \rho(r) 4\pi r^2 dr = \frac{2\sigma^2 r}{G} \propto r$$

Potential:

$$\phi(r) = 2\sigma^2 \ln(r)$$

Circular Velocity:

$$v_c(r) = \sqrt{\frac{GM(r)}{r}} = \sqrt{2}\sigma$$

NFW Profile

Density distribution:

$$\rho(r) = \frac{4\rho_s}{(r/r_s)(1 + r/r_s)^2}$$

Enclosed Mass:

$$M(r) = \int_0^r \rho(r) 4\pi r^2 dr = 16\pi\rho_s r_s^3 \left(\ln(1 + \frac{r}{r_s}) - \frac{r/r_s}{1 + r/r_s} \right)$$

Potential:

$$\phi(r) = -16\pi G\rho_s r_s^2 \frac{\ln(1 + r/r_s)}{r/r_s}$$

Circular Velocity:

$$v_c(r) = \sqrt{\frac{GM(r)}{r}}$$

NFW Profile vs. SIS Profile, using consistent definitions

Density distribution:

$$\rho(r) = \frac{4\rho_s}{(r/r_s)(1 + r/r_s)^2}$$

Density distribution:

$$\rho(r) = \frac{\rho_s}{(r/r_s)^2}$$

Enclosed Mass:

$$M(r) = 16\pi\rho_s r_s^3 \left(\ln(1 + \frac{r}{r_s}) - \frac{r/r_s}{1 + r/r_s} \right)$$

Enclosed Mass:

$$M(r) = 4\pi\rho_s r_s^2 r$$

Potential - const.:

$$\phi(r) = -16\pi G\rho_s r_s^2 \frac{\ln(1 + r/r_s)}{r/r_s}$$

Potential - const.:

$$\phi(r) = 4\pi G\rho_s r_s^2 \ln(r/r_s)$$

Spherical Symmetry Systems

Name	$\rho(r)$	$\Phi(r)$
Plummer	$\frac{3M}{4\pi a^3}\left(1+\frac{r^2}{a^2}\right)^{-5/2}$	$\frac{-GM}{\sqrt{r^2+a^2}}$
Hernquist	$\frac{M}{2\pi}\frac{a}{r(r+a)^3}$	$\frac{-GM}{r+a}$
Jaffe	$\frac{M}{4\pi}\frac{a}{r^2(r+a)^2}$	$\frac{GM}{a}\ln\left(\frac{a}{r+a}\right)$
Gamma	$\frac{(3-\gamma)M}{4\pi a^3}\frac{a^4}{r^\gamma(r+a)^{4-\gamma}}$	$\frac{GM}{a}\begin{cases}\frac{1}{\gamma-2}\left[1-\left(\frac{r}{r+a}\right)^{2-\gamma}\right], & \gamma\neq 2\\ \ln\left(\frac{r}{r+a}\right), & \gamma=2\end{cases}$

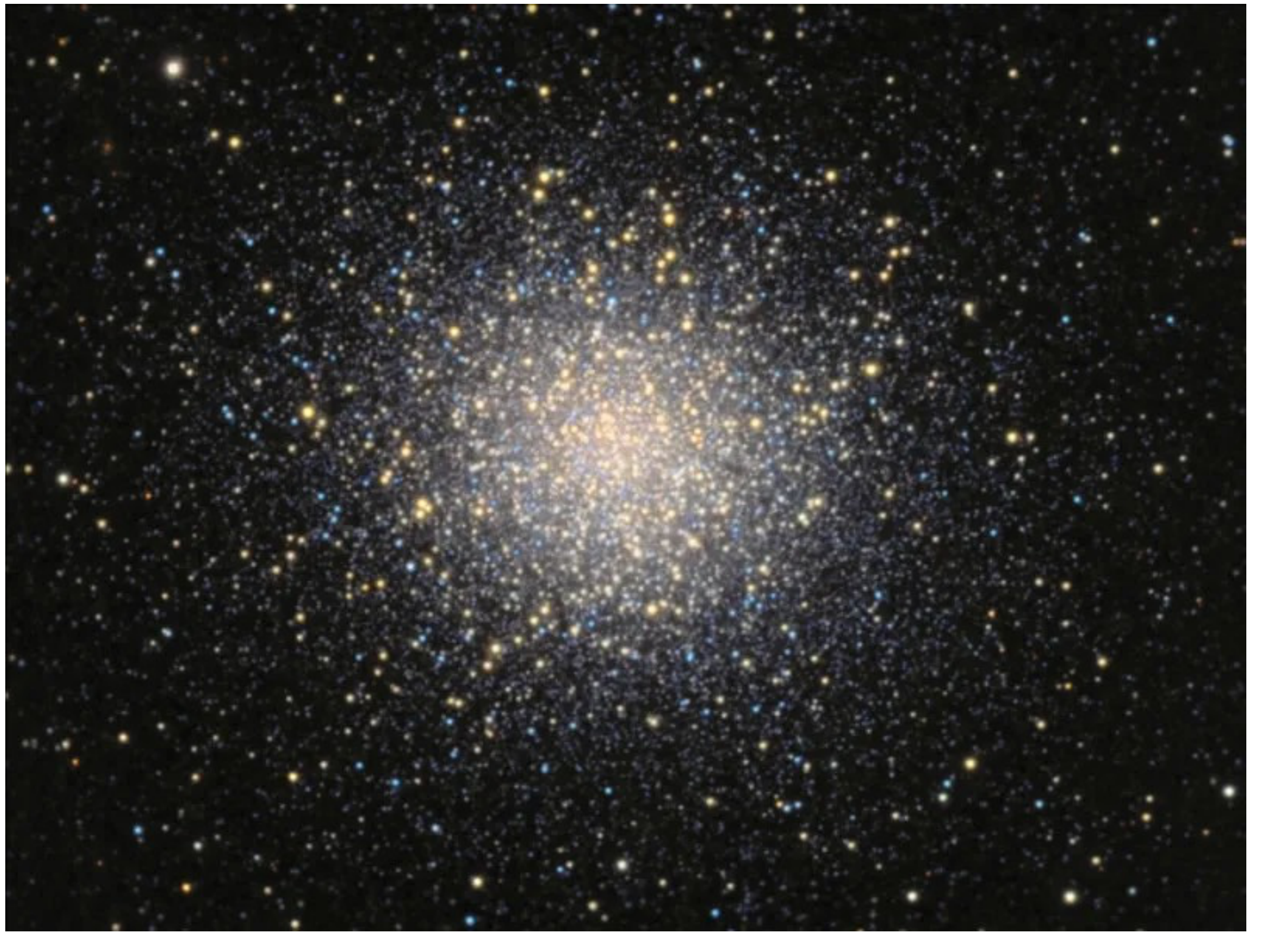

J. Barnes & BT

Circular Velocity Profiles of Different double-power-law density models

$$\rho(r) = \frac{\rho_0}{(r/a)^\alpha (1 + r/a)^{\beta-\alpha}} \qquad v_c(r) = \sqrt{\frac{GM(r)}{r}}$$

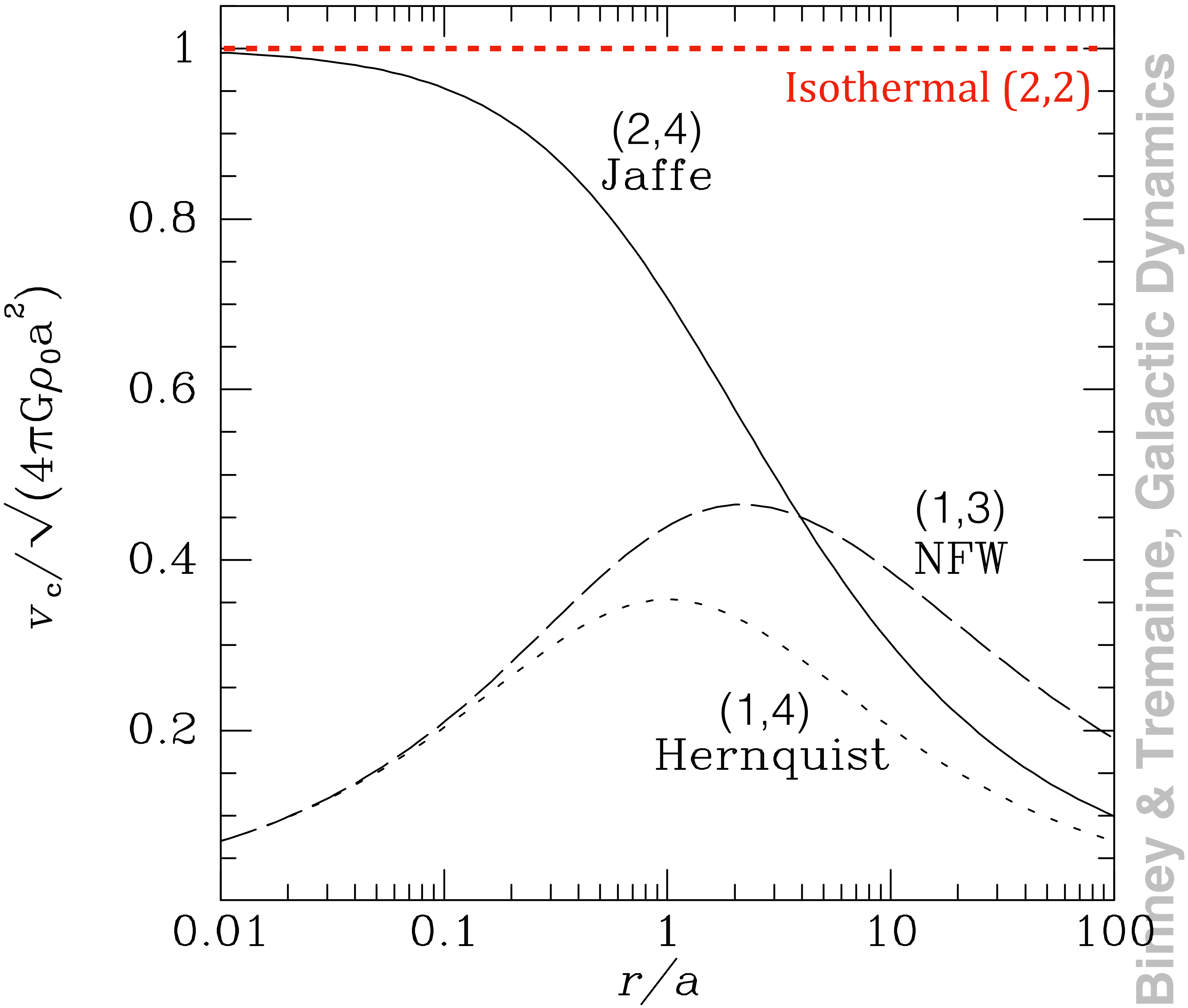

What about non-circular orbits in a logarithmic potential field?

General form: $\phi(x, y, z) = 0.5 \ln(R_c^2 + x^2 + (y/b)^2 + (z/c)^2)$

When b=c=1: $\phi(r) = 0.5 \ln(R_c^2 + r^2)$

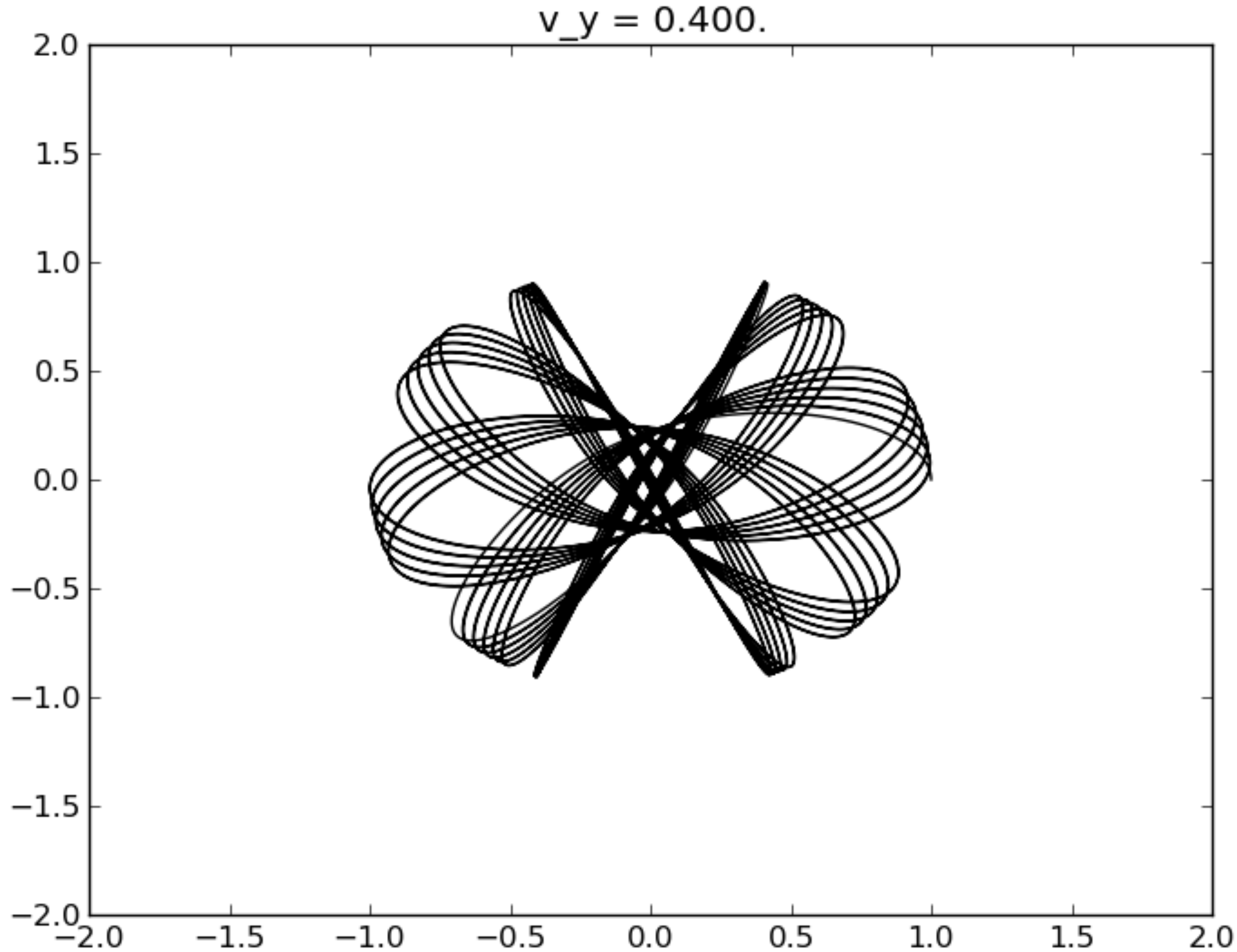

Galaxy-Scale (E/S0): Density Profile ~ SIS

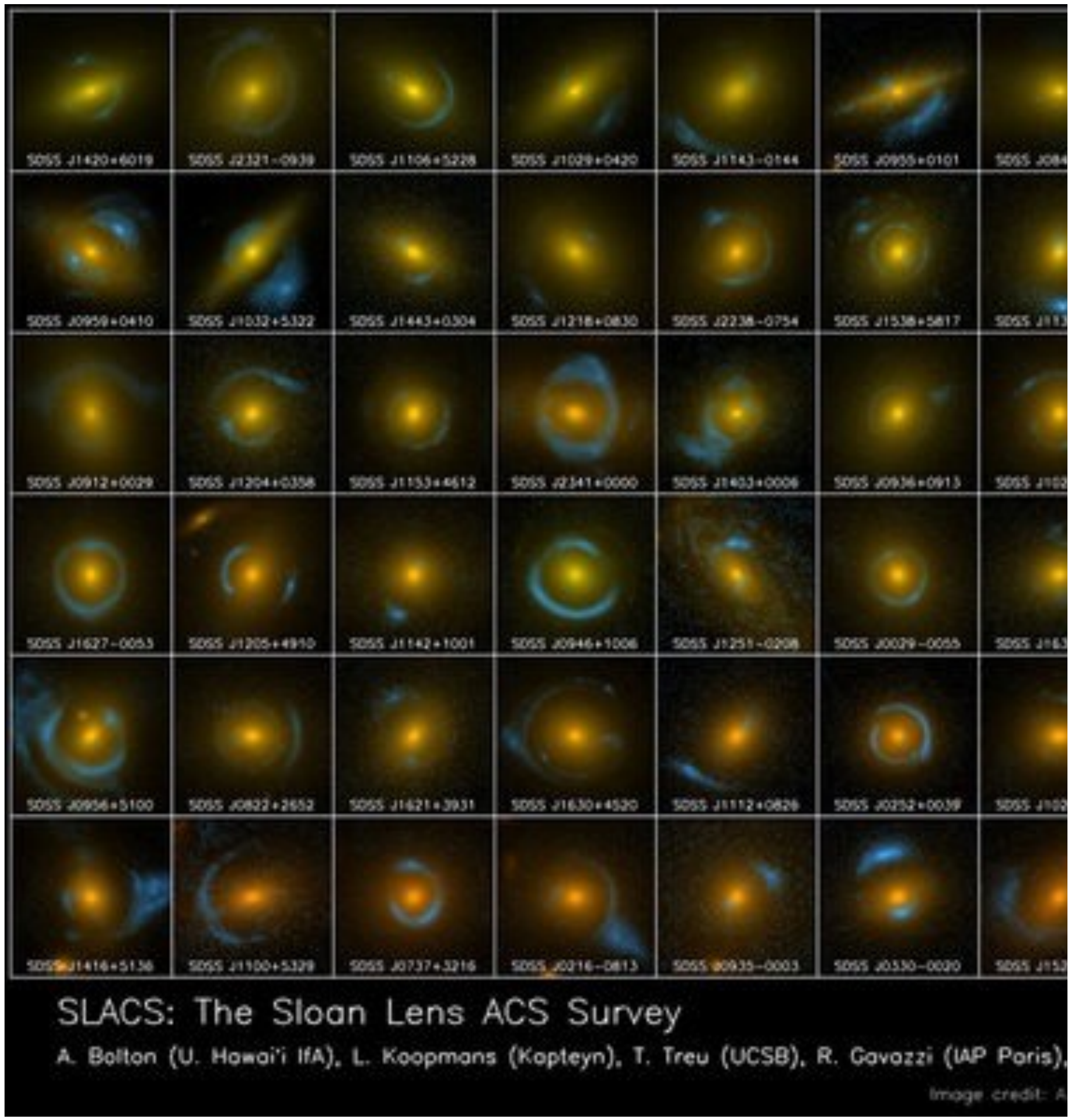

Koopmans+2009

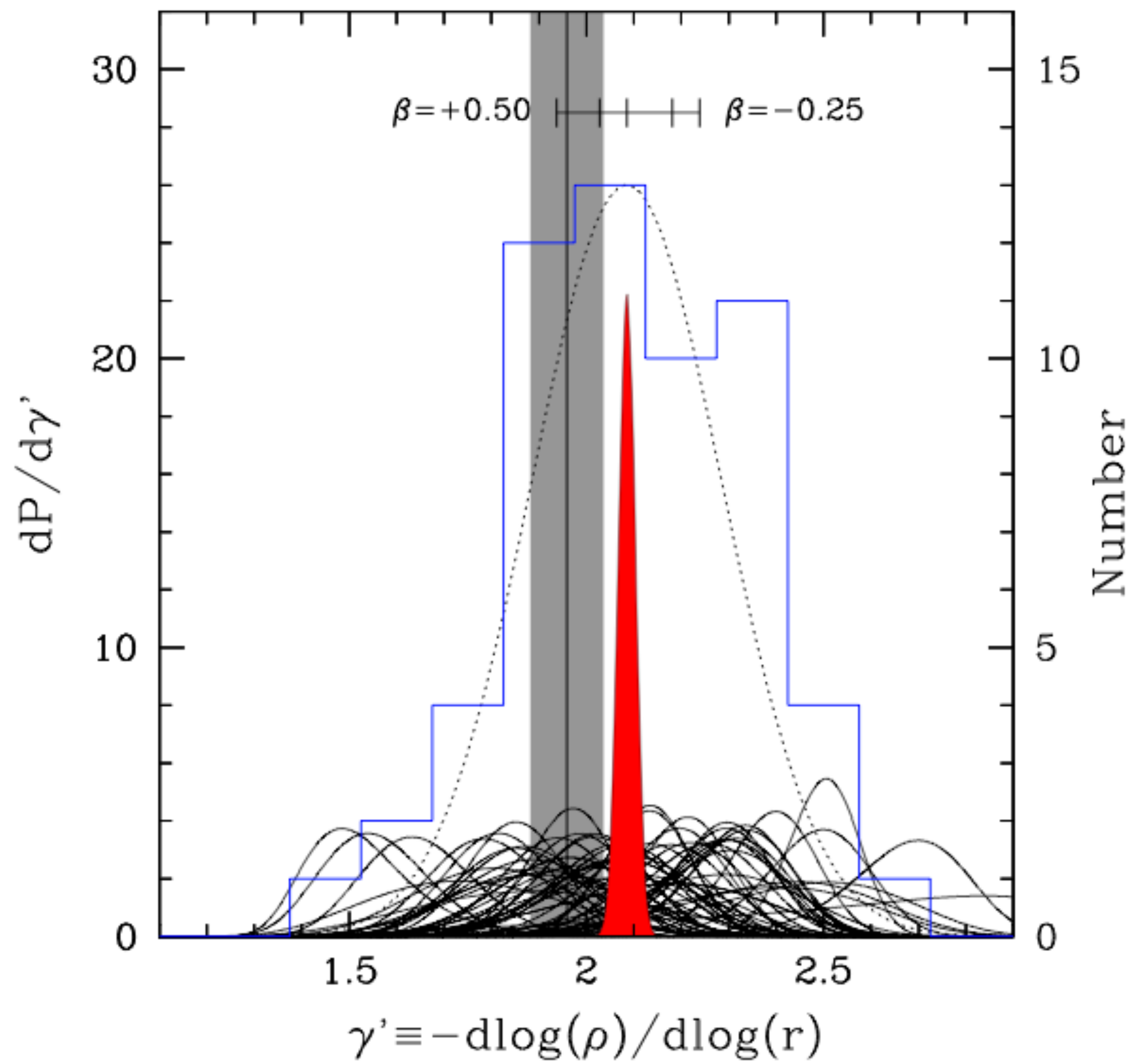

Figure 1. Logarithmic density slopes of 58 SLACS ETGs (thin solid curves). The filled red curve is the joint likelihood of the *ensemble-average* density slope. The histogram indicates the distribution of median values and the dotted Gaussian curve indicates the intrinsic scatter in $\gamma'_{\rm LD}$ (see text for details). We assume a Hernquist luminosity-density profile. The small dashes indicate the shift in the ensemble-average density slope for $\beta_r = +0.50, +0.25, -0.50, -0.25$ (left to right), respectively. Note the reversal of the $\beta_r = -0.50$ and -0.25 dashes. The vertical solid line and gray region indicate the best-fit value and 68% CL interval, respectively, of the average density derived from scaling relations.

Modeling Strong Gravitational Lensing

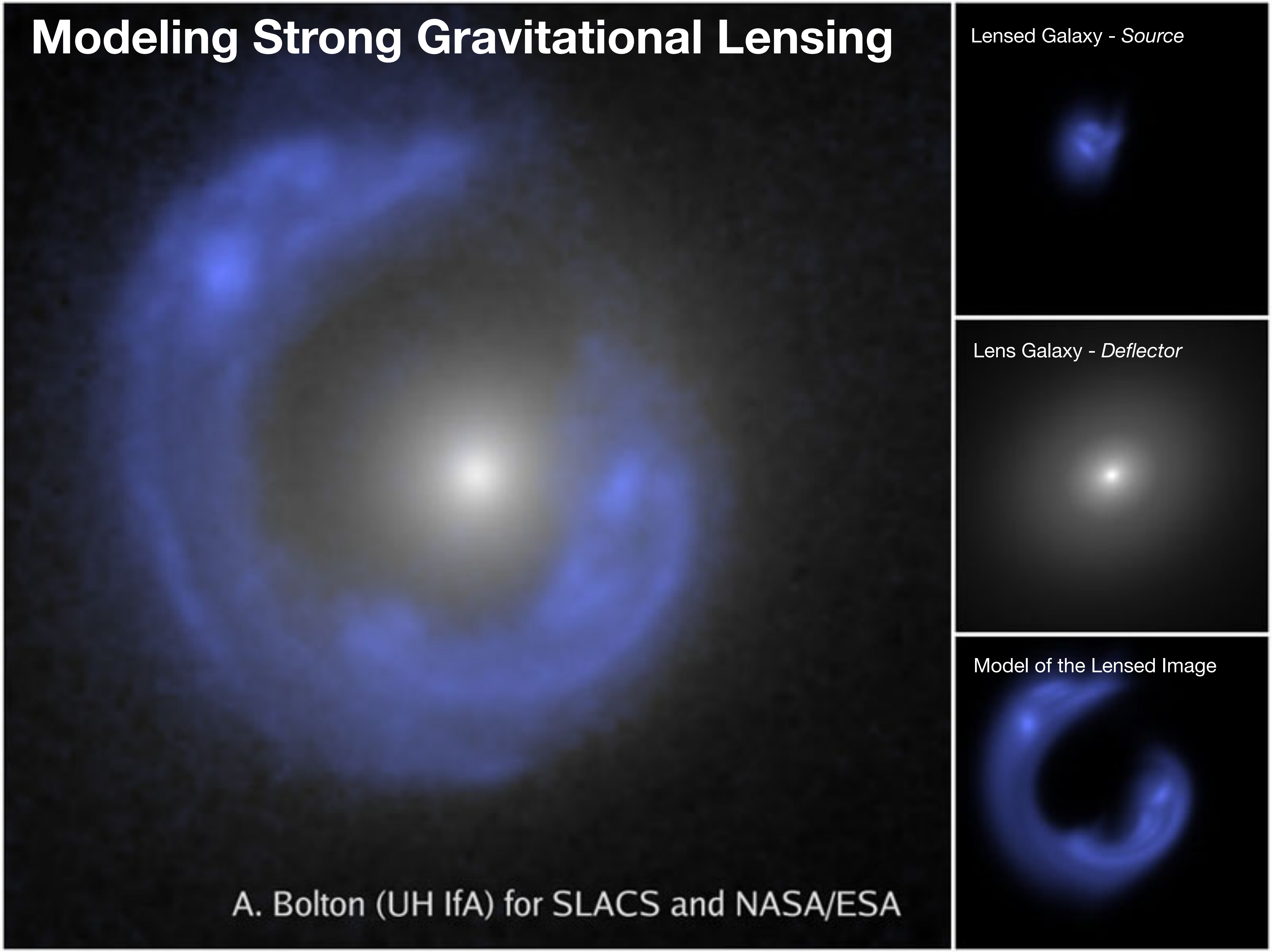

Cluster-Scale Strong Lensing: Density Profile ~ NFW Profile

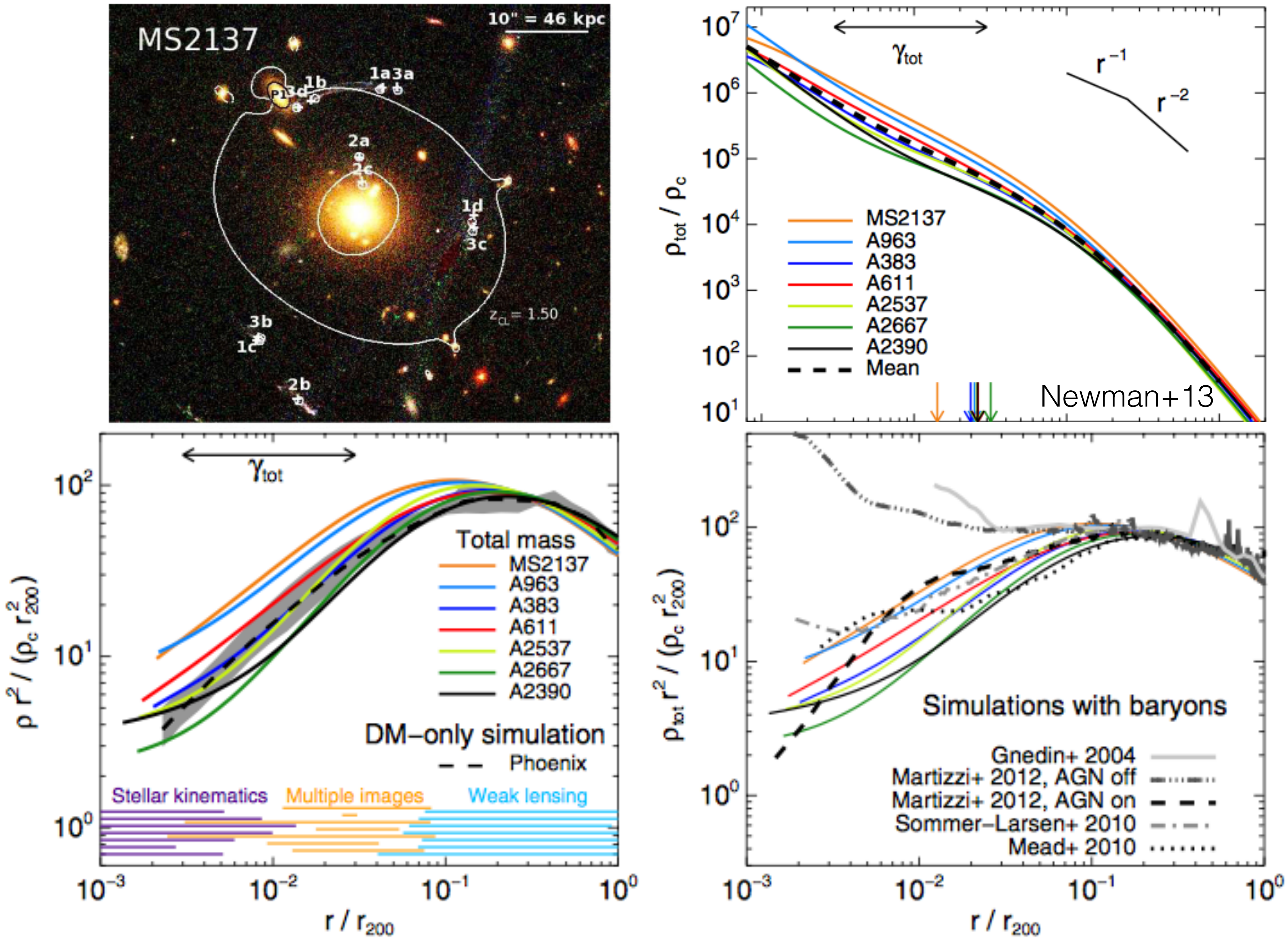

Figure 18. Left: total scaled density profiles for the full sample (colored lines) are compared to simulated clusters—containing only DM—from the Phoenix project (Gao et al. 2012). The dashed line shows the mean of the seven simulated Phoenix clusters, while the gray band outlines the envelope they define. Observed profiles are plotted down to 3 kpc. The radial range spanned by each data set is indicated at the bottom, and the interval over which γ_{tot} is defined is shown at the top of the panel. Note that the density has been multiplied by r^2 to reduce the dynamic range; thus, an isothermal slope $\rho \propto r^{-2}$ is horizontal. Right: the observed total density profiles (thin lines, as in left panel) are compared to several hydrodynamical simulations that include baryons, cooling, and feedback. The Gnedin et al. (2004) results are taken from their Figure 2, the Sommer-Larsen & Limousin (2010) curves refer to their Coma "Rz2" simulation, and the Mead et al. (2010) results are for their C4 simulation with cooling, star formation, and AGN feedback.

Axial Symmetry Systems (thin disks)

General Axial Symmetry Systems

clay sculpture turntable

Only for spherical symmetry systems $v(r) = \sqrt{GM(r)/r}$

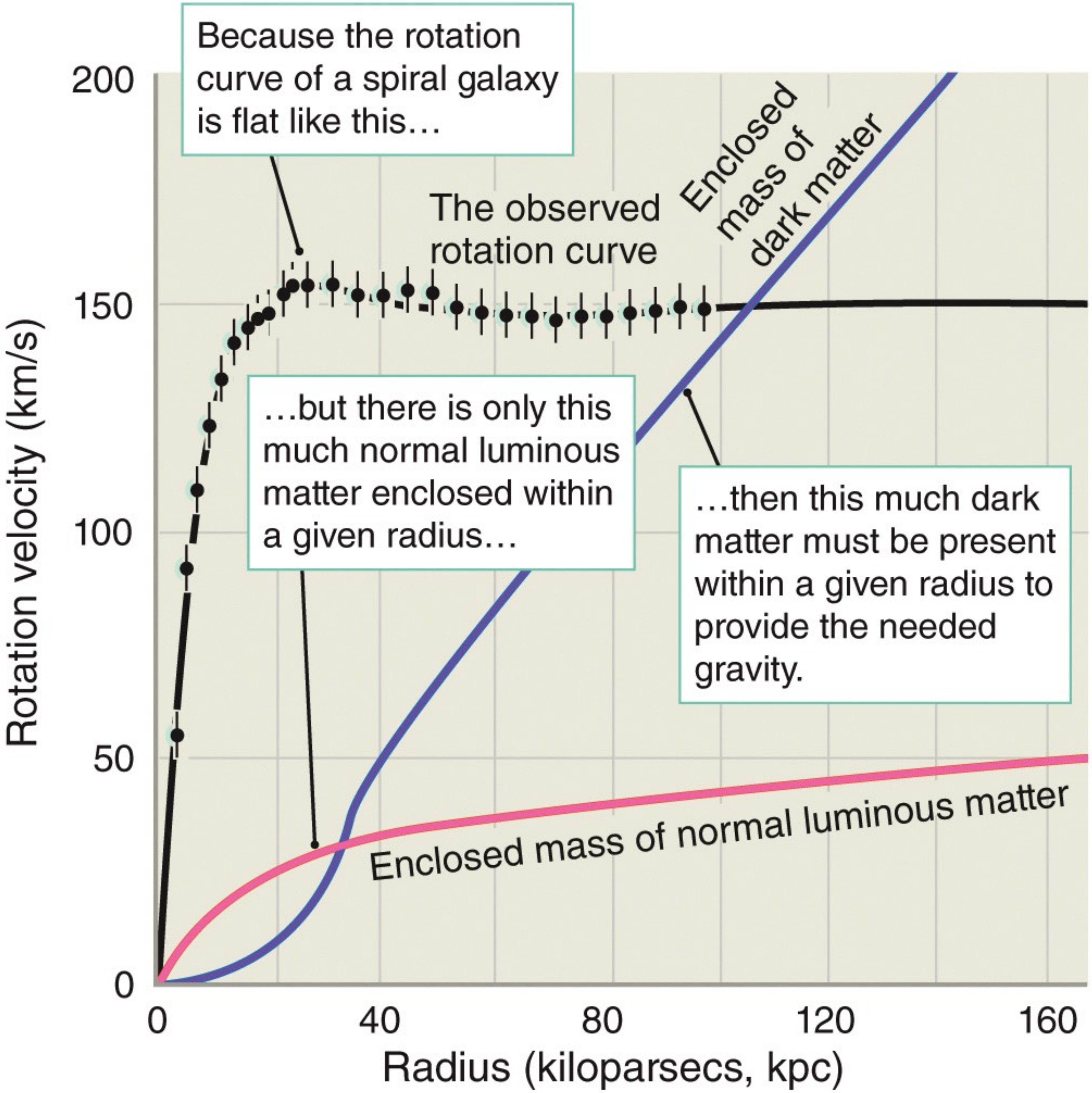

So this illustration widely used in textbooks is over-simplified because the normal luminous matter is mostly distributed on a disk instead of a sphere

Circular Velocity Profiles: Axial Symmetry vs. Spherical Symmetry

The spherical system has the same enclosed mass profile as the disk

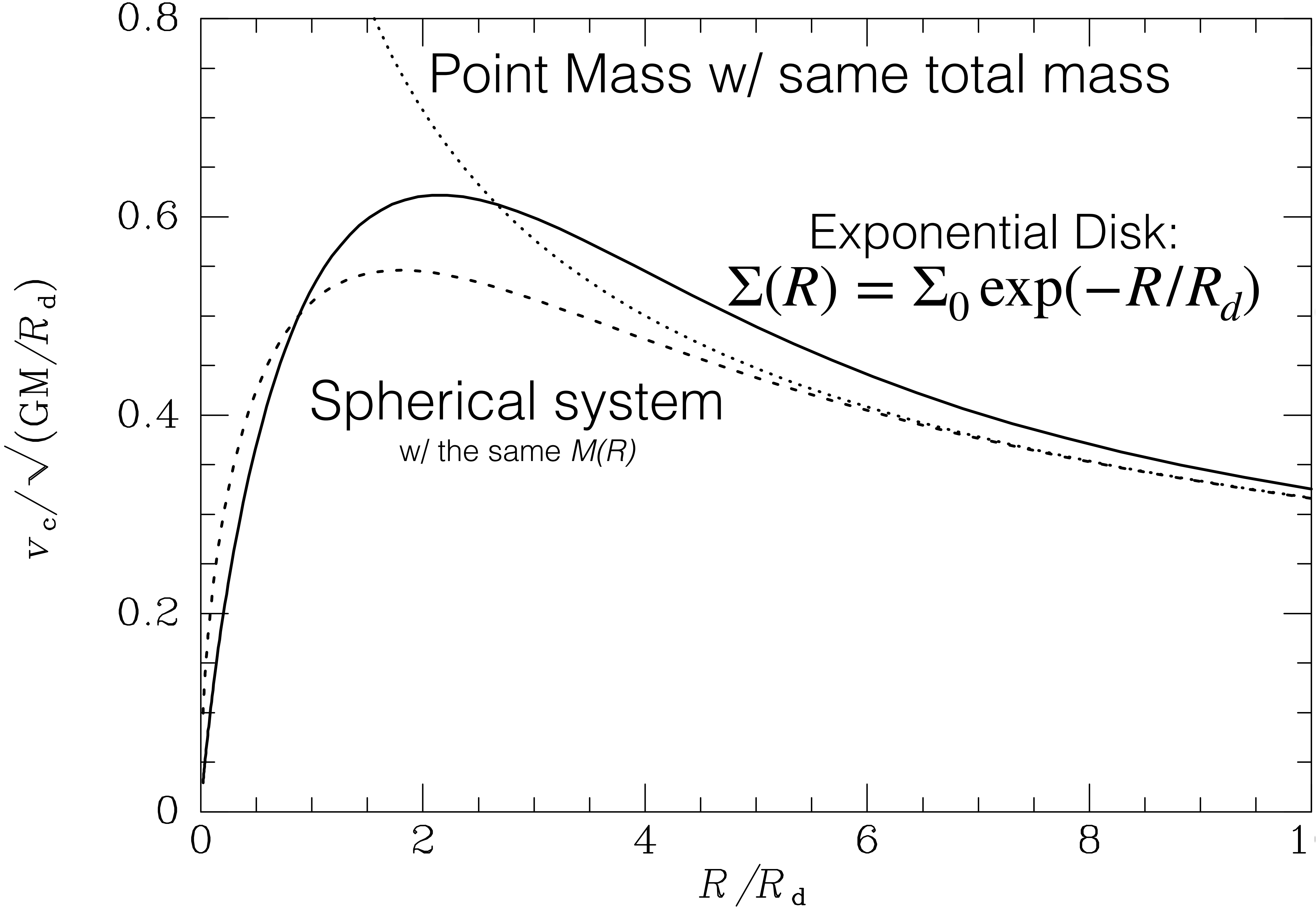

Potential of a Kuzmin Disk

Name	$\Sigma(R)$	$\Phi(R,z)$
Kuzmin	$\dfrac{aM}{2\pi(R^2+a^2)^{3/2}}$	$\dfrac{-GM}{\sqrt{R^2+(a+\lvert z\rvert)^2}}$

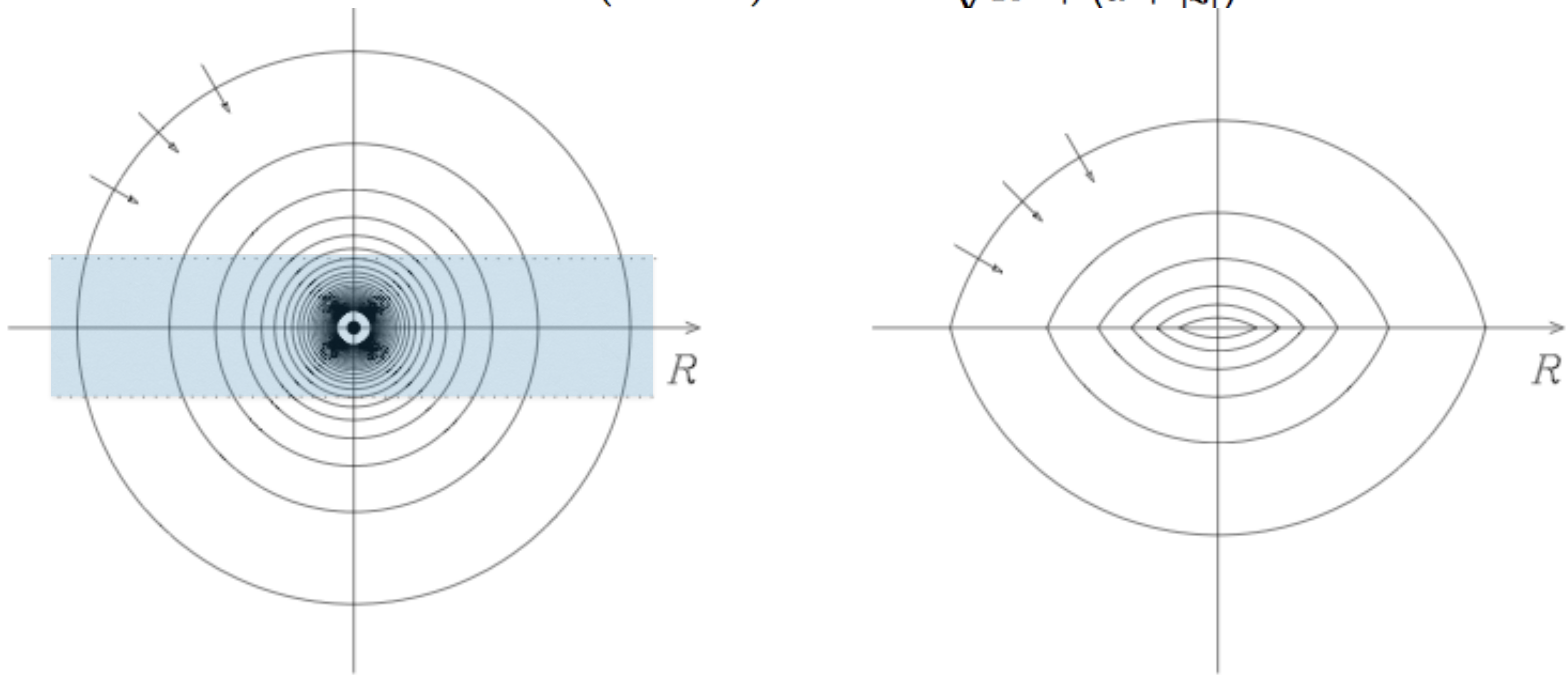

Figure 7.1: Surgery on the potential of a point mass produces the potential of a Kuzmin disk. Left: potential of a point mass. Contours show equal steps of $\Phi \propto 1/r$, while the arrows in the upper left quadrant show the radial force field. Dotted lines show $z = \pm a$. Right: potential of a Kuzmin disk, produced by excising the region $|z| \leq a$ from the field shown on the left. Arrows again indicate the force field; note that these no longer converge on the origin.

Iso-density Contours of Axisymmetric Systems

Generalized Kuzmin Disks

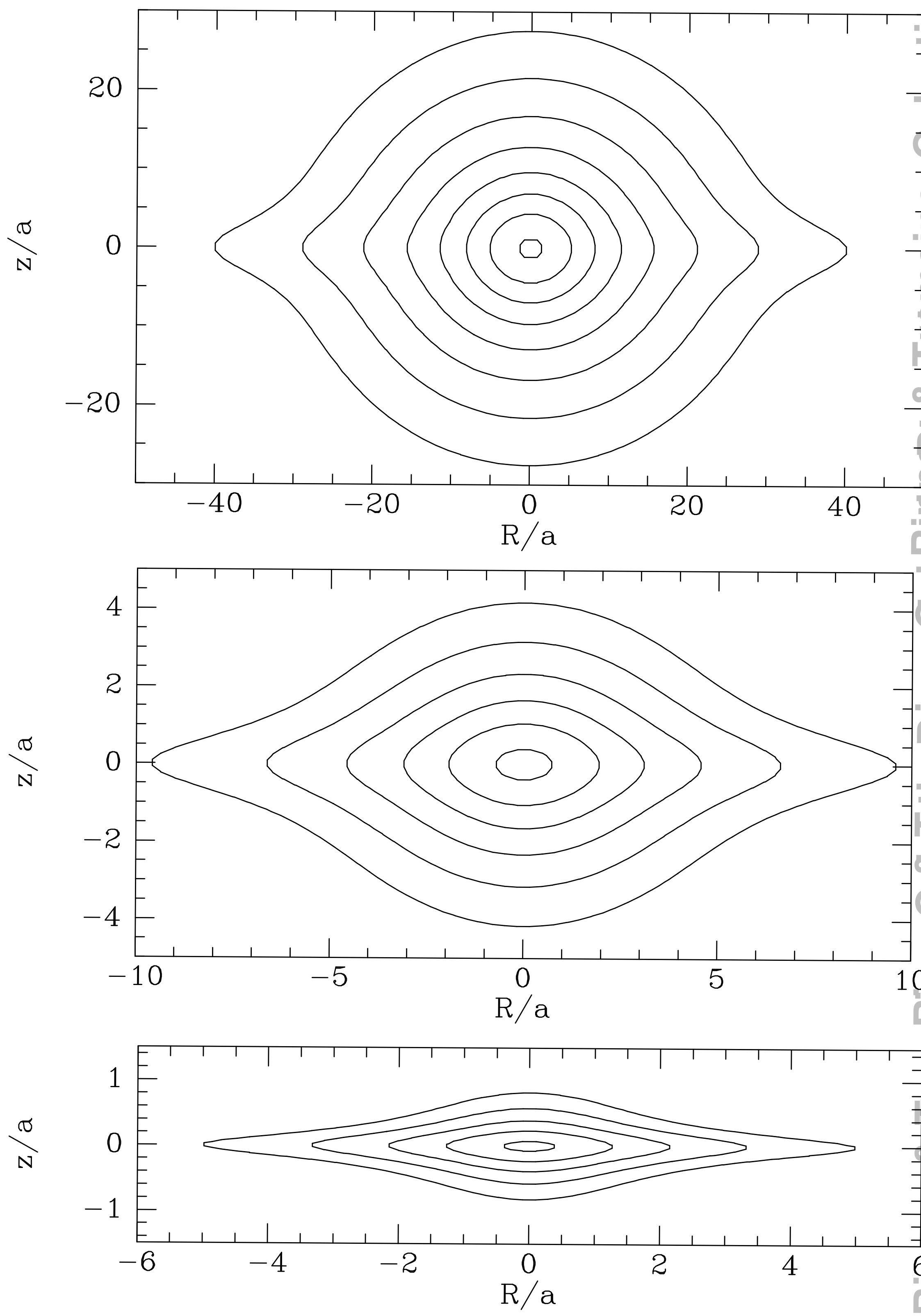

Logarithmic Potential Disks

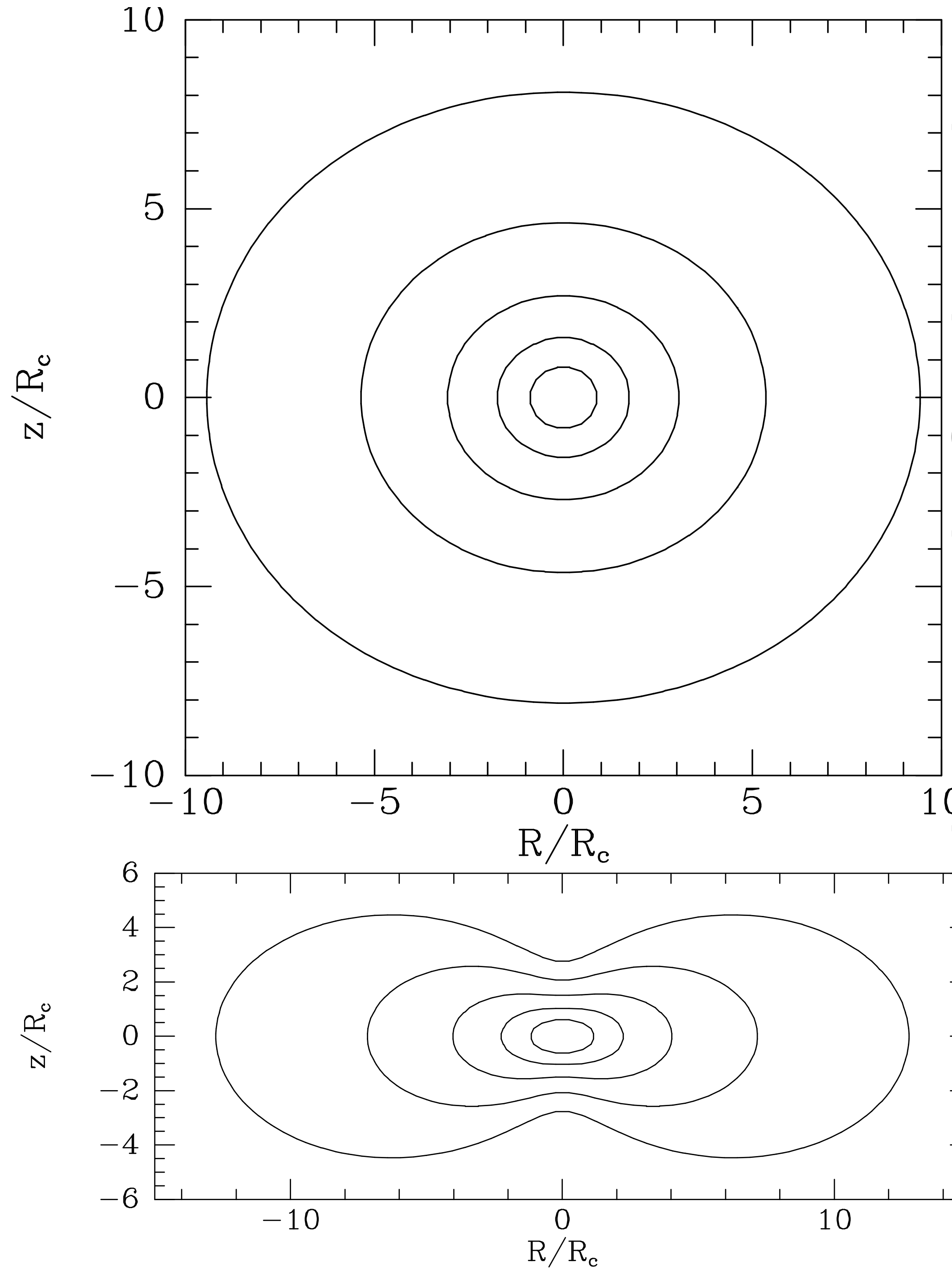

Rotation Curve Modeling of Disk Galaxies with Potential-Density Pairs

A LONGSLIT PLACED ALONG A GALAXY'S MAJOR AXIS

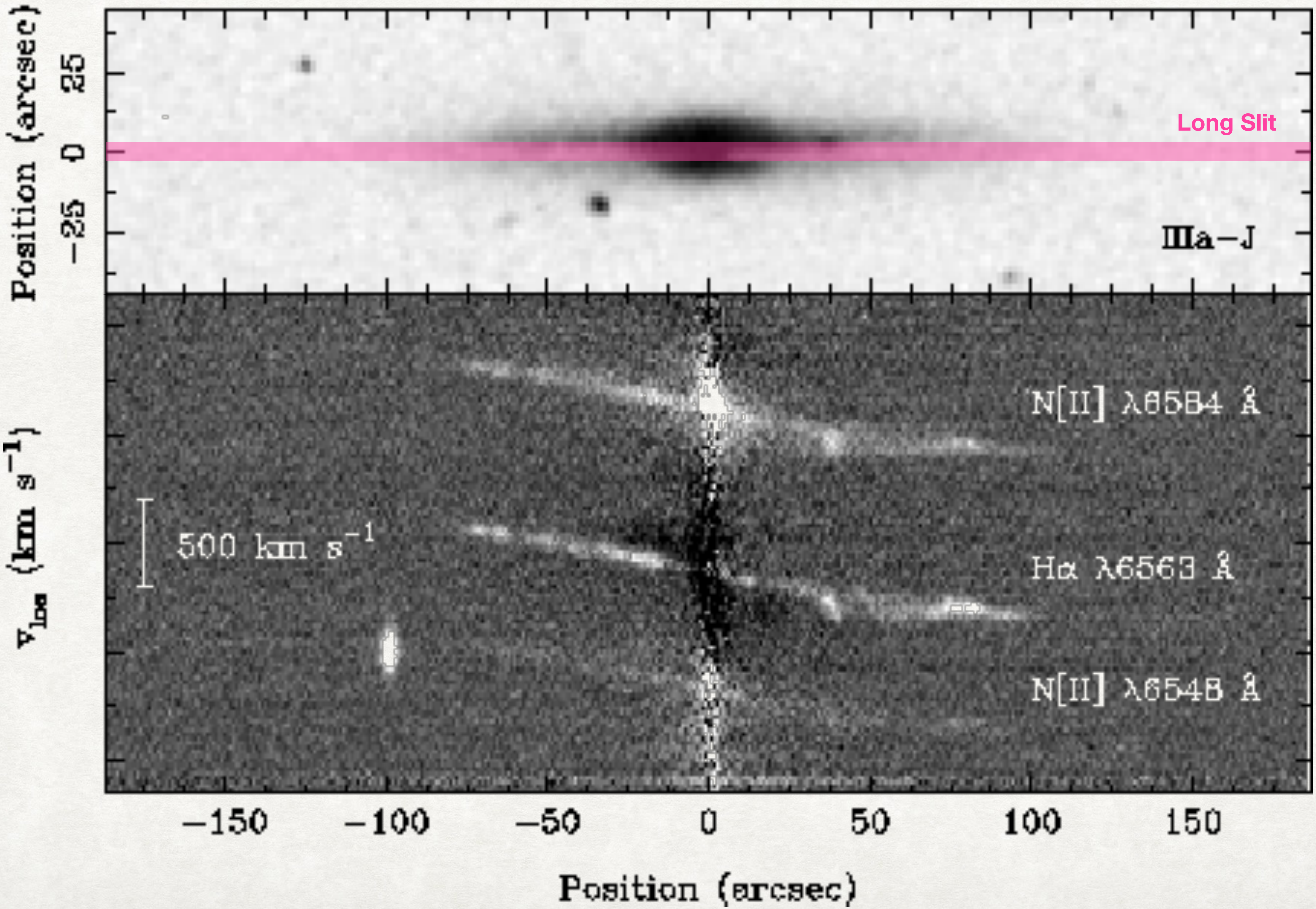

Observed Rotation Velocities Need to be Corrected for Inclination Angle

$$v_{\text{obs}} = v_{\text{int}} \sin i$$

Estimate inclination angle from b/a ratio

Oblate Ellipsoid Model of Disk Galaxies (Hubble 1926)

$$\cos^2 i = \frac{(b/a)^2 - q^2}{1 - q^2} .$$

- where **b** and **a** are the semi-minor and semi-major axis of the ellipse, and i is the inclination angle and **q** is the edge-on thickness

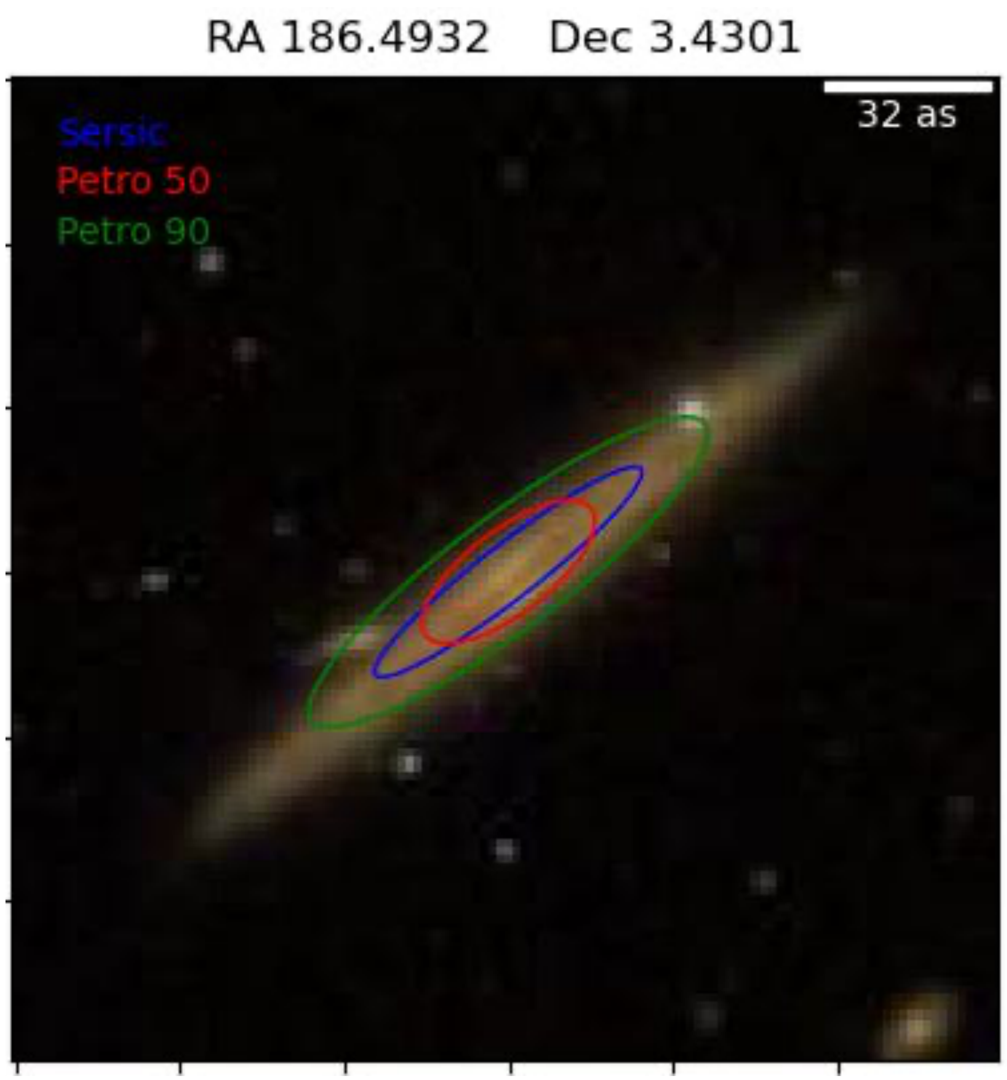

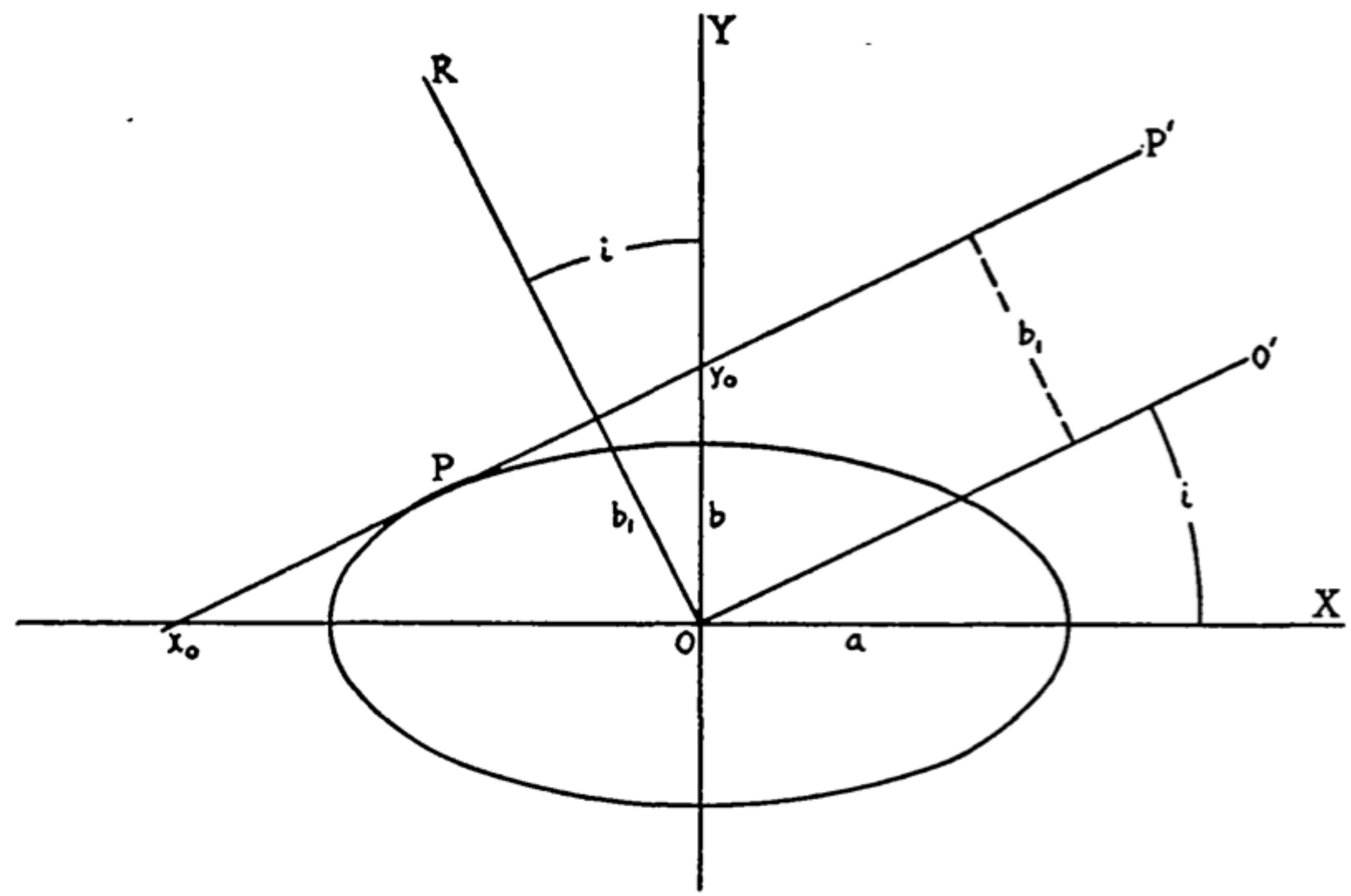

Model Mass Components of a Disk Galaxy

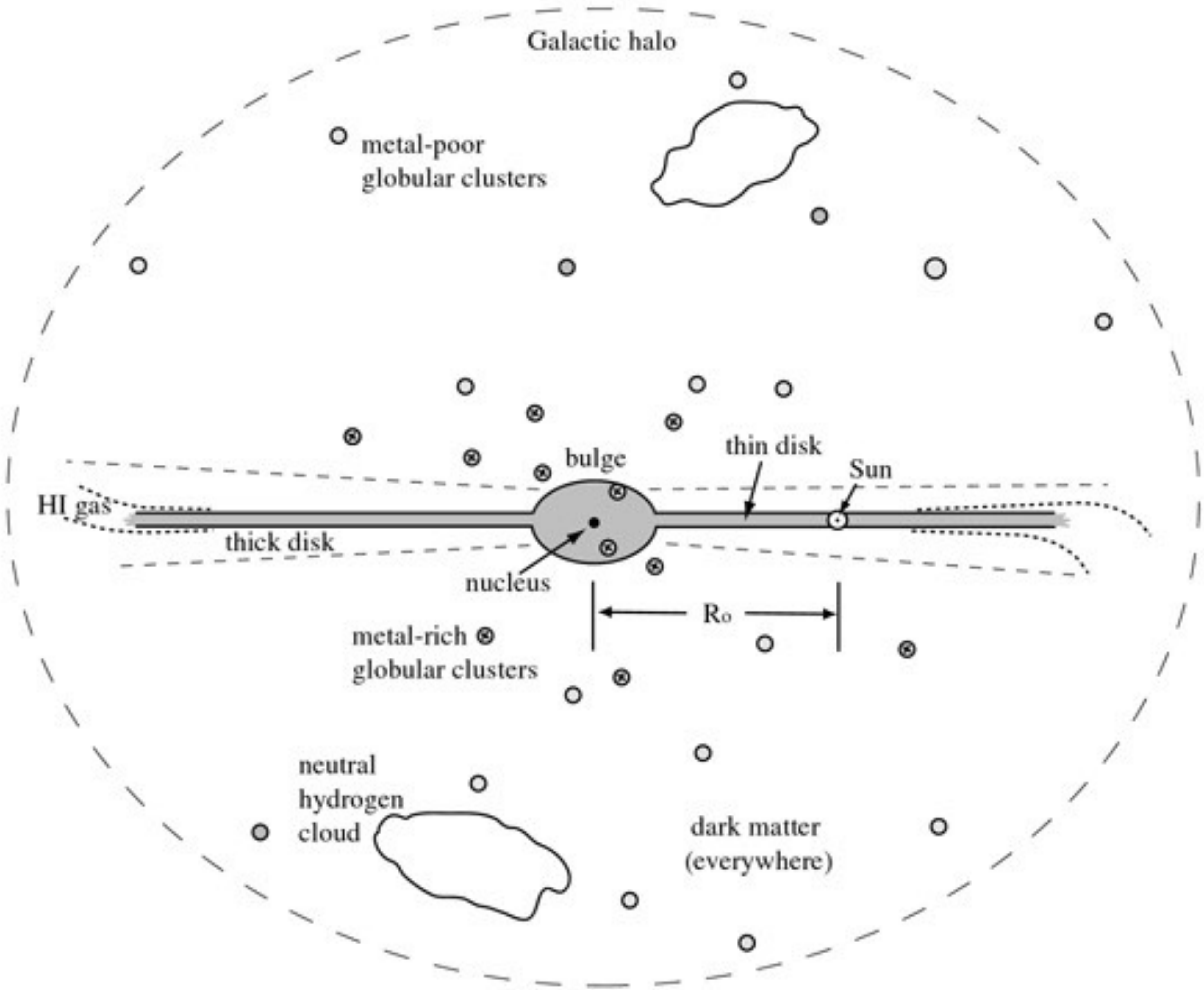

Fig 1.8 'Galaxies in the Universe' Sparke/Gallagher CUP 2007

Equipotential Contours of the Mass Components

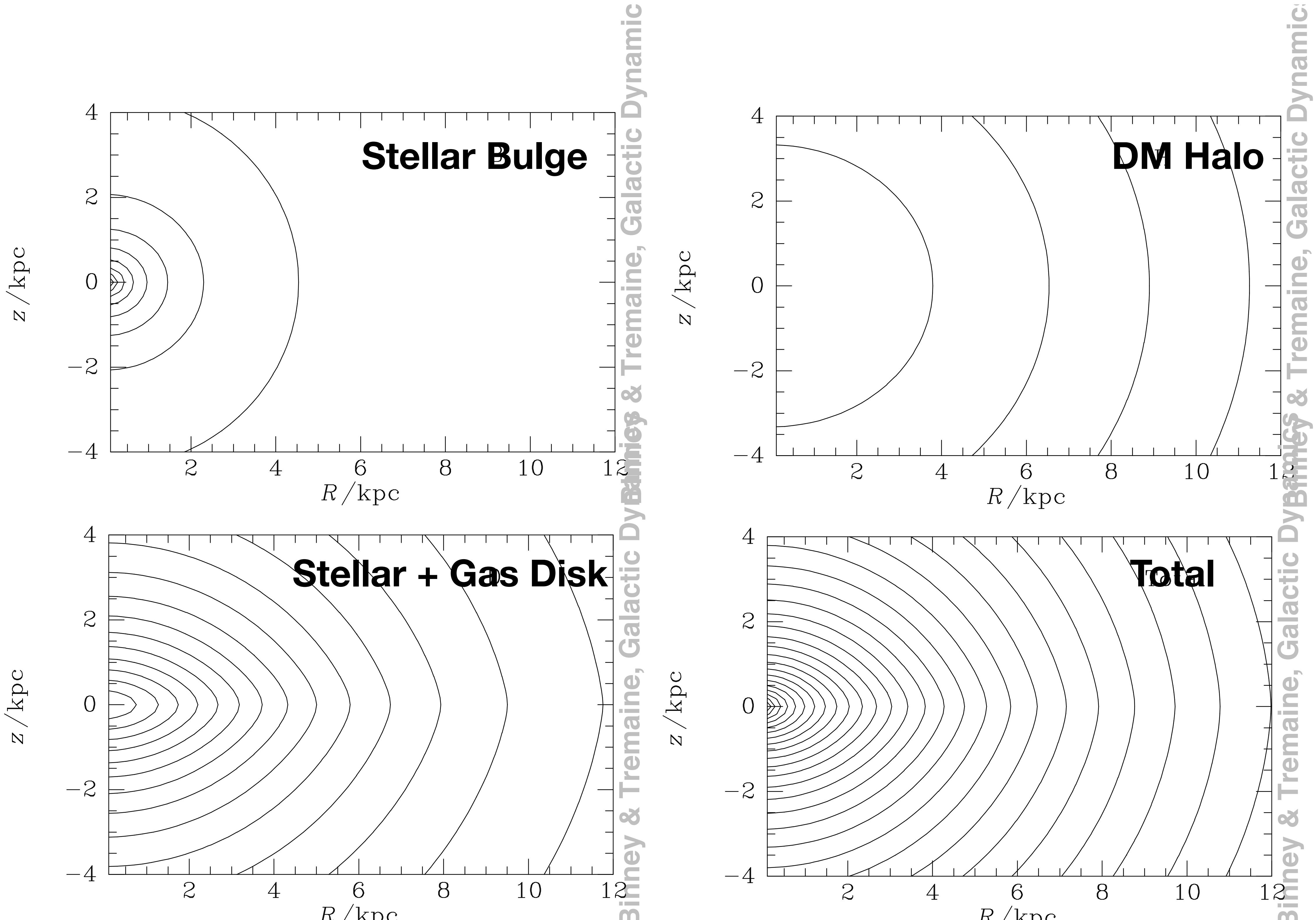

Circular velocity can be calculated with $\vec{g} = -\nabla\phi = v^2/r$

Fitting the Observed Rotation Curve of NGC 3198 w/ an NFW halo

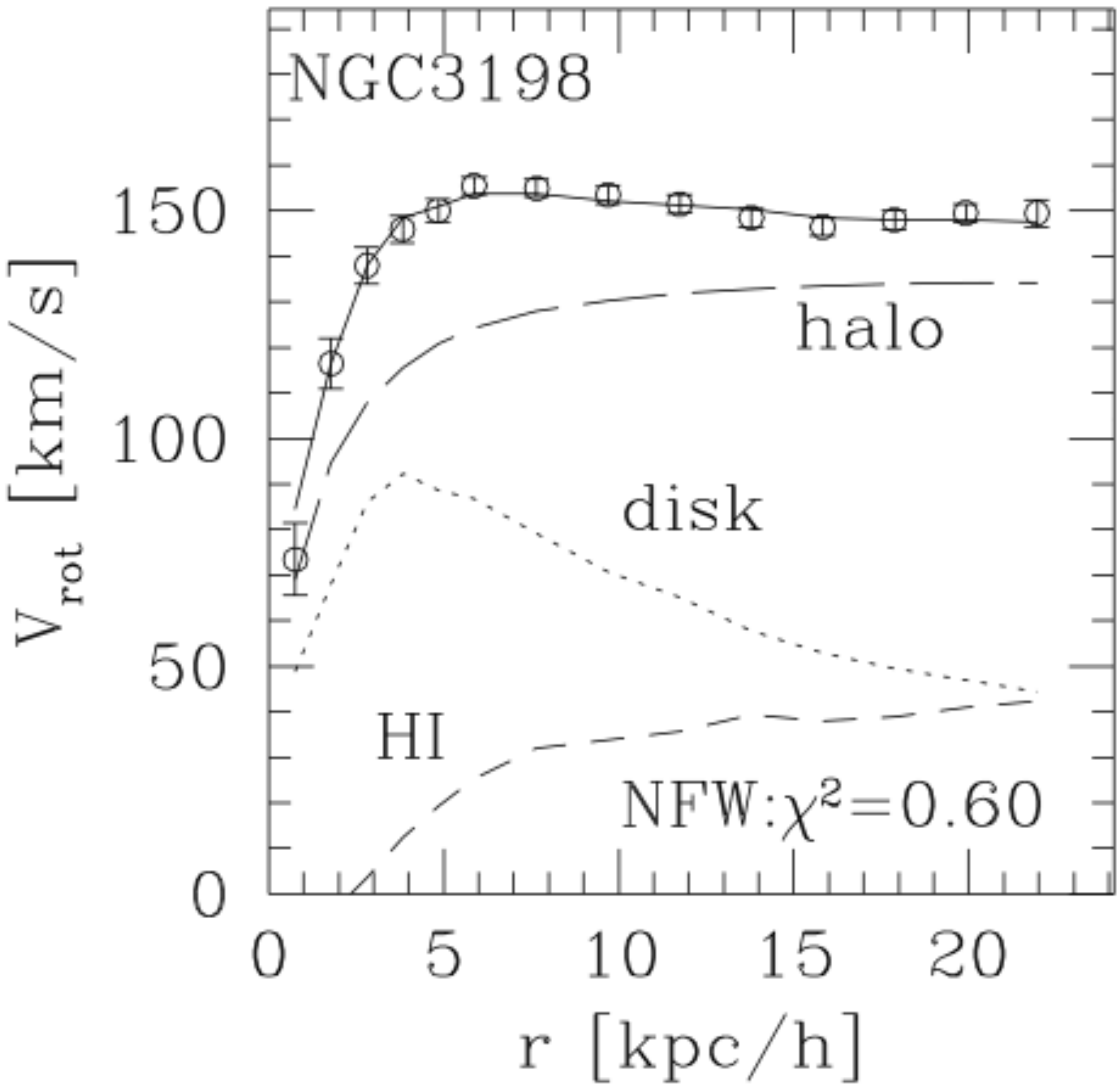

Navarro 1998

Usually, multiple models can fit the rotation curve equally well

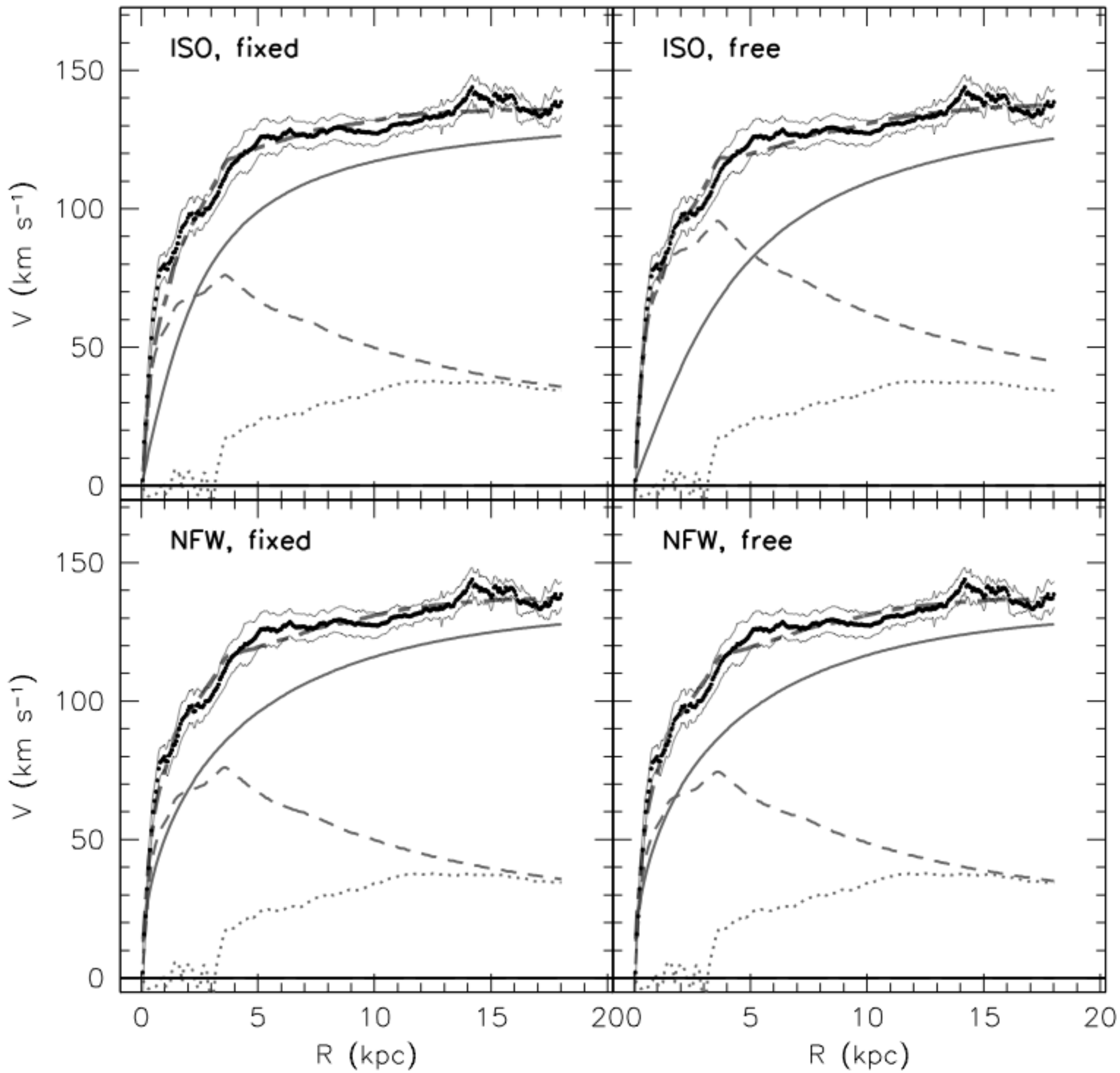

De Blok+2008

Detailed Modeling of Stellar Kinematics in Elliptical Galaxies w/ Orbit Superposition

Galaxies are self-gravitating systems in dynamical equilibrium

- The mass distribution $\rho(r, \theta, \phi)$ determines gravitational potential: $\nabla^2 \phi = 4\pi G \rho$
- The gravitational potential determines the orbits: $\mathbf{g} = -\nabla \phi$
- The orbits determine how much **time** objects spend at each location $\tau(r, \theta, \phi)$, thus determines the **mass distribution.** The loop is closed.

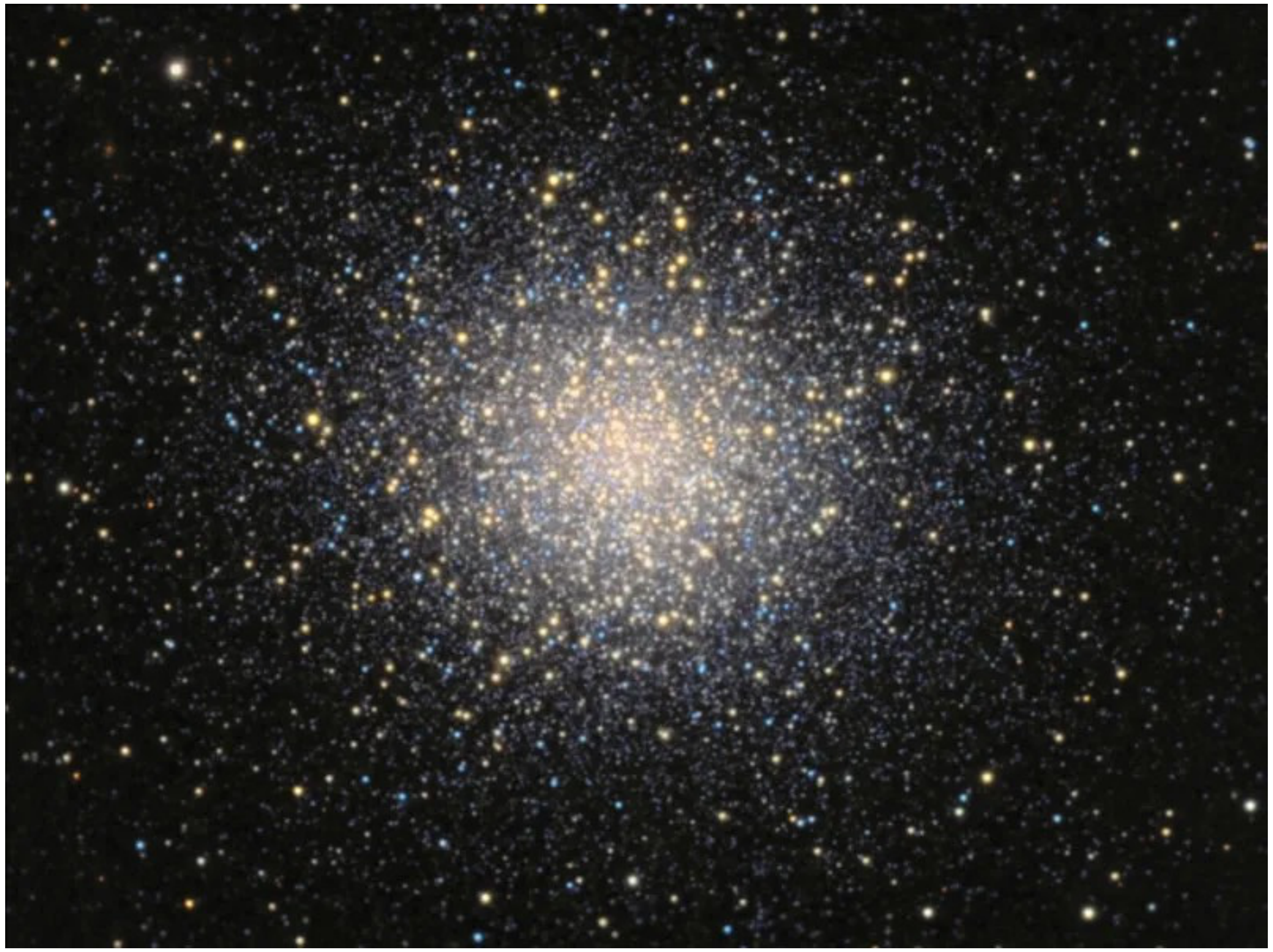

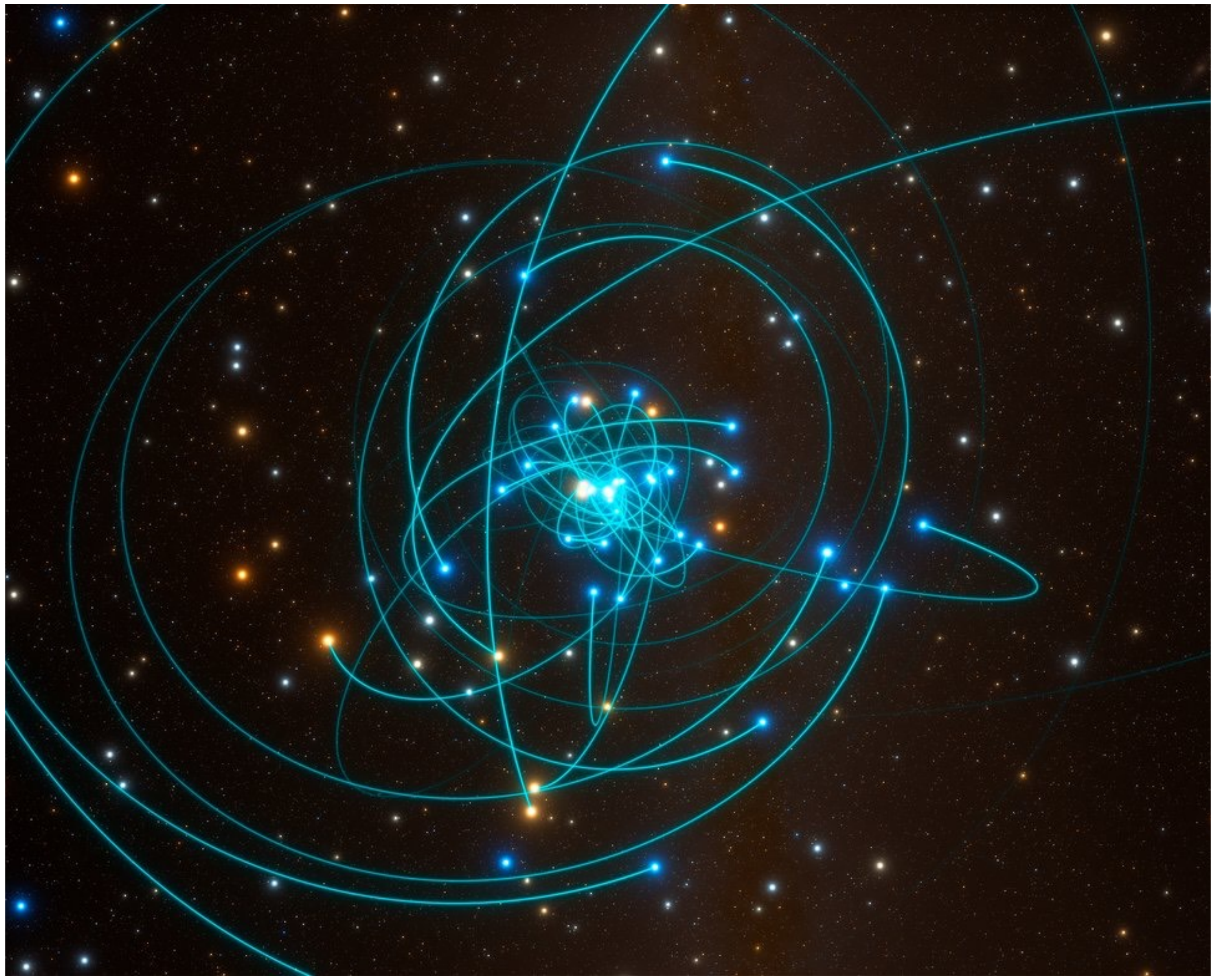

Imaging and spectroscopy provide useful 2D measurement, but to infer the full 3D information requires dynamical modeling

- Imaging observations provide maps of the light distribution of stars and gas in the galaxy, which can be used to infer the 2D projected mass distribution
- Integral-field spectroscopic observations provide a map of Doppler shift, which then gives us the line-of-sight velocities.
- But even perfect observations provide **incomplete information** of the galaxy:
  - only the surface density *projected* along the line-of-sight is measured
  - only the velocity component along the line-of-sight is measured

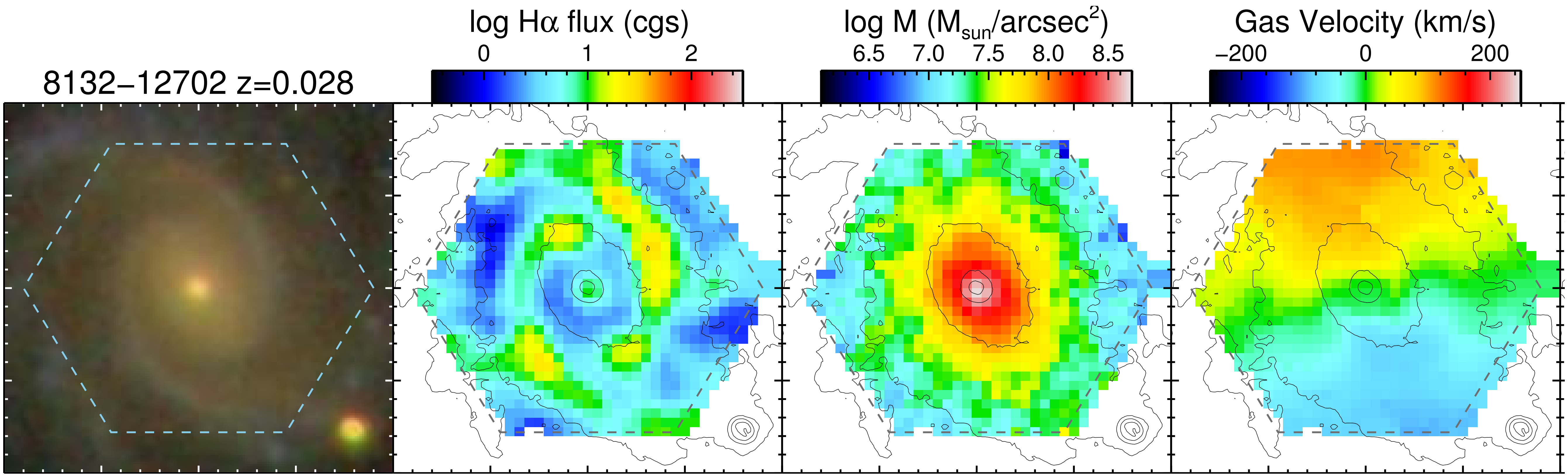

Data from SDSS IV/MaNGA Survey, Figure made by Hai Fu

Elliptical Galaxies: Irregular Orbits of Stars

In ellipticals and in bulges of spiral galaxies, stars orbit in many different directions and move on irregular orbits. The velocity dispersion (r*andom motion*) dominates over the rotation velocity (*ordered motion*)

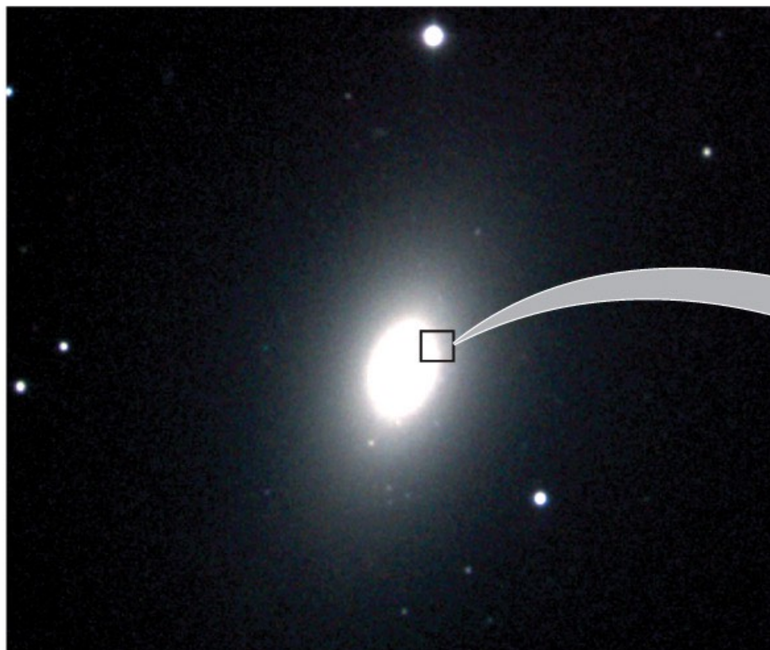

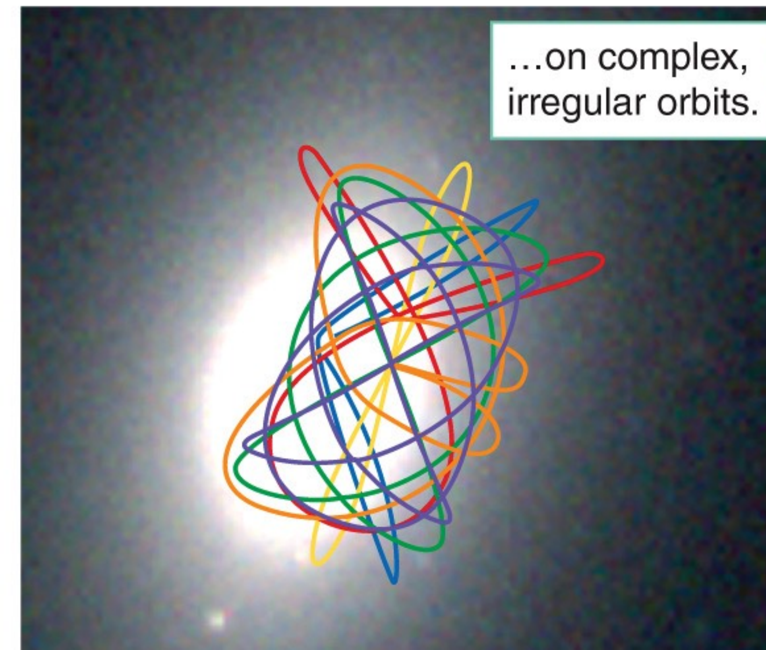

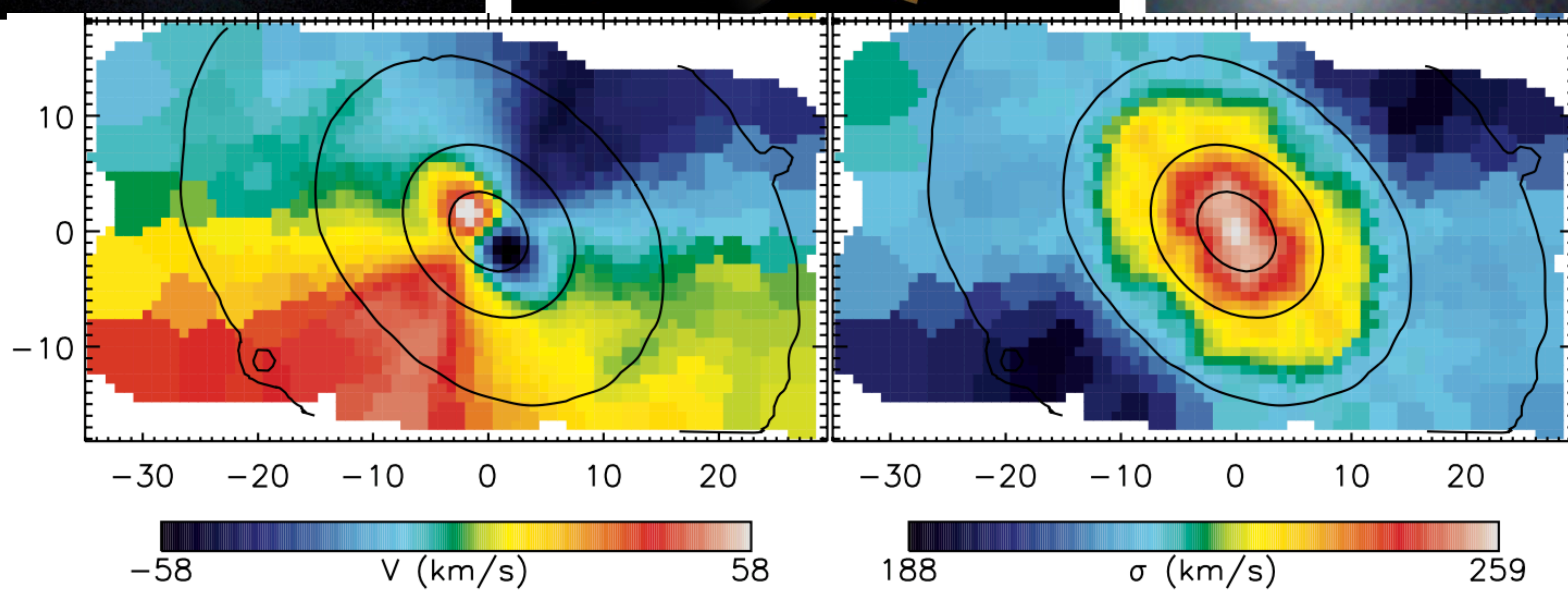

NGC4365

van den Bosch+ 2008

How to find a dynamical model that is consistent with observations?

- The **orbit-superposition approach** by **Martin Schwarzschild (1979)**.
- Specify a ***M/L*** and a geometric model to *deproject* the observed surface light distribution $\Sigma(\alpha, \delta)$ to obtain the 3D density distribution $\rho(\vec{x})$
- Find the corresponding gravitational potential by solving the Poisson Equation: $\nabla^2 \Phi(\vec{x}) = 4\pi G \rho(\vec{x})$
- Construct a grid of ***K* cells** in position space
- Choose initial positions and velocities for a set of ***N* orbits,** for each one
  - integrate the equation of motion for many orbital periods $\vec{g}(\vec{x}) = -\nabla \Phi(\vec{x})$
  - keep track of the time the orbit spends in each of the **K cells;** this is proportional to how much mass the orbit contributes to each cell.
- Determine **non-negative weights** for each orbit such that the summed mass in each cell is equal to the mass implied by the original $\rho(\vec{x})$.
- Use the model to predict the line-of-sight velocity distribution and compare it with the **observed stellar kinematics**, modify $\rho(\vec{x})$ if necessary and repeat until the process converges.

Elliptical Galaxies and Bulges: Irregular Orbit Families

- In elliptical galaxies and bulges of spiral galaxies, stars orbit in many different directions and move on irregular orbits.
- There are four main orbit families in the triaxial gravitational potential of elliptical galaxies.

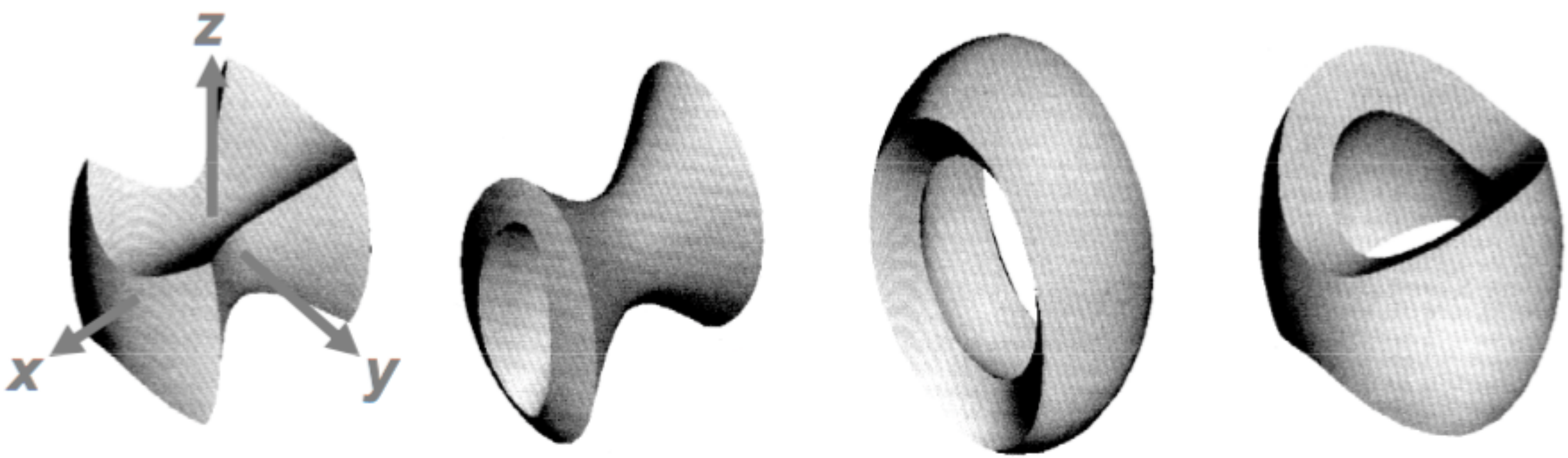

Box | *Inner long-axis tube* | *Outer long-axis tube* | *Short-axis tube*

Projected Views of a Box and a Minor-Axis Tube Orbit

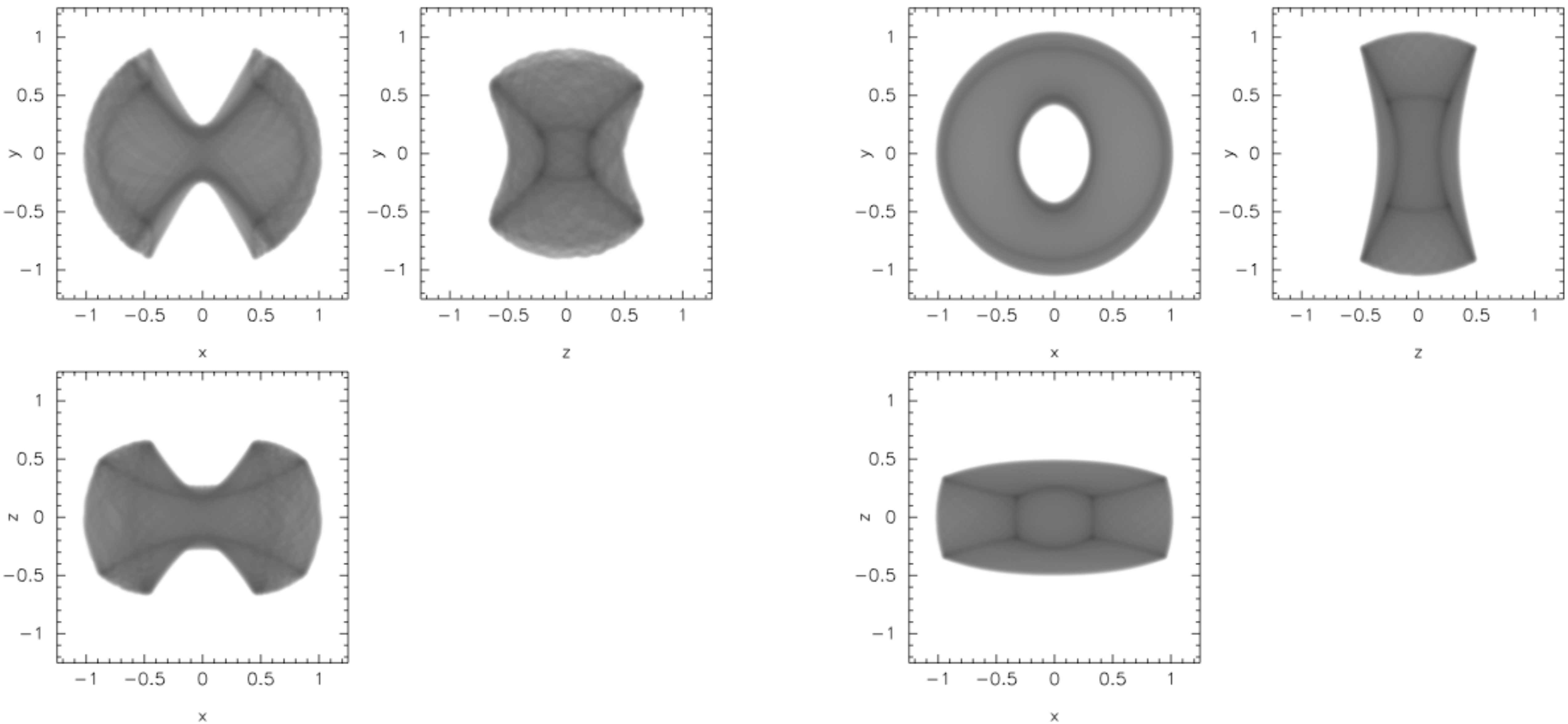

Figure 10.1: Time-averaged orbits in a triaxial logarithmic potential (7.20) with $b = 0.9$, $c = 0.8$, and $R_c = 0.2$. Left: a box orbit generated by starting at position $(x, y, z) = (1, 0, 0)$ with velocity $(v_x, v_y, v_z) = (0, 0.3, 0, 4)$. Right: a minor-axis tube orbit generated by starting at position $(x, y, z) = (1, 0, 0)$ with velocity $(v_x, v_y, v_z) = (0, 0.6, 0.4)$.

Separating the contribution from stars in the four orbit families

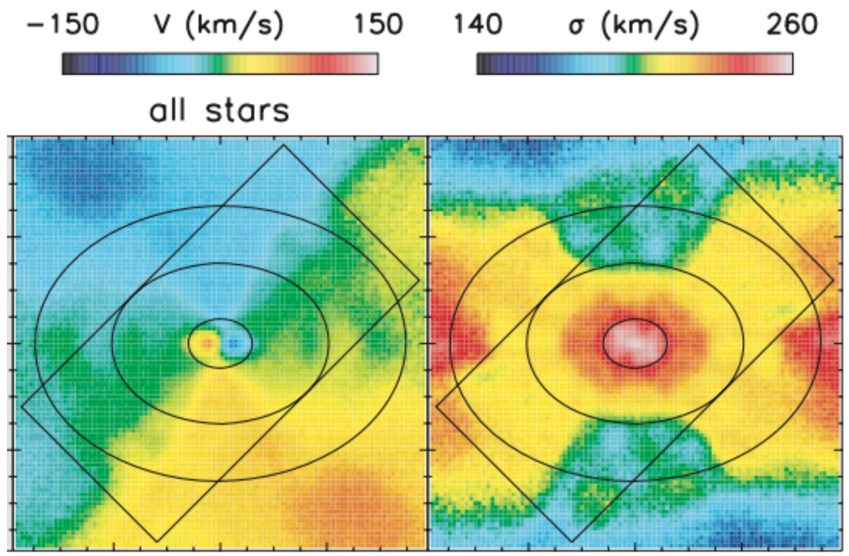

NGC4365

van den Bosch+ 2008